Evaluation of 100-nm-size mechano-responsive liposomes for targeted delivery at constricted arteries

Inauguraldissertation
zur
Erlangung der Würde eines Doktors der Philosophie
vorgelegt der
Philosophisch-Naturwissenschaftlichen Fakultät
der Universität Basel

von

Marzia Maria Gaia Buscema
aus Italien

Basel, 2018

Genehmigt von der Philosophisch-Naturwissenschaftlichen Fakultät

auf Antrag von:

Prof. Dr. Bert Müller, Fakultätsverantwortlicher
Prof. Dr. Alex Dommann, Korreferent

Basel, den 26. Juni 2018

Prof. Dr. Martin Spiess, Dekan

Contents

Summary

Today, cardiovascular disease remains the foremost cause of death worldwide. More than 70% of all cardiovascular diseases are due to dysfunction of the coronary arteries, which fail to supply sufficient oxygen to the heart. As first aid, the intravenous injection of a vasodilatory drug improves the survival rate. The dose, however, is limited because of side effects including a drop in blood pressure. Hence, a targeted instead of a systemic delivery is highly desirable. Recently, mechano-responsive liposomes about 100 nm in diameter have been proposed to transport the drug to the constrictions and preferentially release the vasodilator locally. In order to pave the way for mechano-responsive nano-containers towards patient treatment, the present thesis contains studies on (i) the morphology of a plaque-containing human coronary artery throughout the preparation steps towards histology, (ii) the structural alterations of the liposomes under selected flow conditions, and (iii) the immunological response of the drug-loaded liposomes *in vitro* and *in vivo*. High-resolution hard X-ray tomography in absorption and phase contrast modes have shown that paraffin embedding gives rise to an anisotropic shrinkage by 15 to 65% with respect to formalin fixed tissues. The decalcification procedure compromises the determination of the lumen, leaving remaining components of the plaque abound in the artery's lumen. Consequently, the lumen should be extracted before decalcification and paraffin embedding. For this purpose, phase tomography is much better suited than the conventional attenuation-based approach because of the minor dependence on the atomic number and the related reduction of streak artefacts. The combination of spatially resolved small-angle X-ray scattering with microfluidics allows for the measurement of mechanically induced morphological changes of liposomes. Here, local changes in the average bilayer thickness and the mean size of the mechano-responsive liposomes have been detected. Overall shape and bilayer thickness do change already near the inlet to the constriction, but are dominant near the outlet. At a flow rate of 0.2 µL/sec, the liposome's bilayer thickness increased by 30% compared to the thickness well before the constriction and under static condition. The increase is in line with a mechanically induced loss of interdigitation between the phospholipid acyl chains. The immune response to dedicated nitroglycerin-loaded, mechano-responsive liposomes has been quantified by means of enzyme-linked immunosorbent assays *in vitro* and by monitoring the arterial pressures in pigs *in vivo*. The research findings show comparable or less complement activation than the Food-and-Drug-Administration-approved liposomal drugs Abelcet and Doxil. Even an up to three times human therapeutic dose does not increase the pulmonary artery pressure and the systemic arterial pressure. The results of the three subprojects demonstrate that physical approaches using smart containers of nanometer size can establish a groundbreaking background for the translation of basic science towards future patient treatments.

Zusammenfassung

Herz-Kreislauf-Erkrankungen sind die weltweit am häufigsten auftretende Todesursache. Mehr als 70% dieser Erkrankungen sind die Folge einer Fehlfunktion der Herzkranzarterien, die das Herz nicht mehr mit genügend Sauerstoff versorgen können. Um die Überlebenschancen im Notfall zu erhöhen, verabreicht man intravenös gefässerweiternde Medikamente. Der Dosierung ist dabei aufgrund der auftretenden Nebenwirkungen, einschliesslich Abfall des Blutdrucks, limitiert. Aus diesem Grund ist eine gezielte statt der systemischen Wirkstofffreisetzung erforderlich. Mechanosensitive Liposomen mit einem Durchmesser von ungefähr 100 nm wurden unlängst als Wirkstofffähren eingeführt, die den gefässerweiternden Wirkstoff bevorzugt an der Verengung freisetzen. Um den Weg dieser mechano-sensitiven Wirkstofffähren für die Behandlung von Patienten zu ebnen, umfasst die vorliegende Doktorarbeit Studien über (i) die Morphologie von einem verkalkten menschlichen Herzkranzgefäss in der Abfolge der Präparationsprozesse für die Histologie, (ii) Formveränderungen von Liposomen in ausgewählten Strömungsbedingungen und (iii) die Immunantwort auf wirkstoffbeladene Liposomen *in vitro* und *in vivo*. Hochauflösende Tomographie mit harten Röntgenstrahlen in Absorptions- und Phasenmodi hat aufgezeigt, dass das Einbetten von einem verkalkten Herzkranzgefäss in Paraffin eine anisotrope Schrumpfung von 15 bis 65% gegenüber der Konservierung mittels Formalin verursacht. Zudem beeinträchtigt eine Entkalkung die Vermessung des Lumen, weil verbleibende Plaque-Komponenten die Arterie füllen. Deshalb sollte das Lumen vor der Entkalkung bestimmt werden. Dazu eignet sich der Phasenkontrastmodus besser als der konventionelle Absorptionskontrast, weil aufgrund der geringeren Ordnungszahlabhängigkeit deutlich weniger Artefakte auftreten. Ortsaufgelöste Kleinwinkelröntgenstreuung in einem mikrofluidischen Kanalsystem, das ein Modell für ein verengtes Herzkranzgefäss darstellt, erlaubt festzustellen, inwieweit die Strömungsverhältnisse in einer solchen Verengung die Morphologie der Liposomen beeinflusst. Man kann hierbei die mittleren Dickenänderungen der Lipid-Doppelschicht und die durchschnittlichen Grössenänderungen der Liposomen bestimmen. Die Form und die Lipid-Doppelschicht der Liposomen ändert sich bereits vor der Verengung und ist am Ende der Verengung besonders deutlich. Bei einem Durchfluss von 0.2 µL/sec wird die Lipid-Doppelschicht um bis zu 30% gegenüber dem statischen Zustand grösser. Diese Zunahme der Dicke ist im Einklang mit dem Verlust der Verzahnung zwischen den Alkylketten der Lipide in der Doppelschicht. Die Immunantwort gegenüber gezielt mit Nitroglyzerin beladenen, mechano-sensitiven Liposomen wurde mittels Enzym-gebundener Immunosorbent-Assays *in vitro* und durch Messung der Gefässinnendrücke in Schweinen in vivo quantifiziert. Die Ergebnisse zeigen gegenüber etablierten Liposom-basierten Medikamenten (Abelcet, Doxil) eine vergleichbare oder geringere Komplementaktivierung. Sogar eine gegenüber der heute verwendeten dreimal höhere Dosis erhöht den Gefässinnendruck der Pulmonalarterie nicht. Die Ergebnisse der drei Teilprojekte veranschaulichen, dass physikalische Ansätze für die Nutzung von intelligenten Nano-Wirkstofffähren wegweisende Hinweise für

weitere Entwicklungen vor dem Hintergrund einer zukünftigen Patientenbehandlung schaffen können.

List of Publications

Journal Publications

M. Buscema, H. Deyhle, T. Pfohl, A. Zumbuehl, B. Müller, "Spatially resolved small-angle X-ray scattering for characterising mechano-responsive liposomes using microfluidics", *Materials Today Bio* (submitted)

M. Buscema, H. Deyhle, S.E. Hieber, G. Schulz, A. Hipp, F. Beckmann, J.A. Lobrinus, T. Saxer, B. Müller, "Ex vivo evaluation of a plaque-containing human coronary artery via histology and high-resolution hard X-ray tomography", *Scientific Reports* (submitted)

M. Buscema, S. Matviykiv, T. Mészáros, G. Gerganova, A. Weinberger, U. Mettal, D. Mueller, F. Neuhaus, E. Stalder, T. Ishikawa, R. Urbanics, T. Saxer, T. Pfohl, J. Szebeni, A. Zumbuehl, B. Müller, "Immunological response to nitroglycerin-loaded shear-responsive liposomes *in vitro* and *in vivo*", *Journal of Controlled Release* **264**, 14–23, (2017) (doi:10.1016/j.jconrel.2017.08.010)

S. Matviykiv, **M. Buscema**, G. Gerganova, T. Mészáros, G.T. Kozma, U. Mettal, F. Neuhaus, T. Ishikawa, J. Szebeni, A. Zumbuehl, B. Müller, "Immunocompatibility of Rad-PC-Rad liposomes *in vitro*, based on human complement activation and cytokine release", *Precision Nanomedicine* **1**, 45–67, (2018) (doi:10.29016/180410.1)

S. Bugna, **M. Buscema**, S. Matviykiv, R. Urbanics, A. Weinberger, T. Meszaros, J. Szebeni, A. Zumbuehl, T. Saxer, B. Müller, "Surprising lack of liposome-induced complement activation by artificial 1,3-diamidophospholipids *in vitro*", *Nanomedicine: Nanotechnology, Biology, and Medicine* **12**, 845–849, (2016) (doi:10.1016/j.nano.2015.12.364)

Peer-Reviewed Conference Proceedings

M. Buscema, G. Schulz, H. Deyhle, A. Khimchenko, S. Matviykiv, M. N. Holme, A. Hipp, F. Beckmann, T. Saxer, K. Michaud, B. Müller, "Histology-validated X-ray tomography for imaging human coronary arteries ", *Proceedings of SPIE* **9967**, 99670O (2016) (doi:10.1117/12.2238702)

M. Buscema, H. Deyhle, T. Pfohl, S.E. Hieber, A. Zumbuehl, B. Müller, "Characterization of mechano-sensitive nano-containers for targeted vasodilation", *Proceedings of SPIE* **9797**, 97970S (2016) (doi:10.1117/12.2238702)

M. Buscema, M. N. Holme, H. Deyhle, G. Schulz, R. Schmitz, P. Thalmann, S.E. Hieber, N. Chicherova, P.C. Cattin, F. Beckmann, J. Herzen, T. Weitkamp, T. Saxer, B. Müller, "Grating interferometry-based phase microtomography of atherosclerotic human arteries", *Proceedings of SPIE* **9212**, 921203 (2014) (doi:10.1117/12.2060443)

H. Deyhle, G. Schulz, A. Khimchenko, C. Bikis, S. E. Hieber, C. Jaquiery, C. Kunz, M. Müller-Gerbl, S. Höchel, T. Saxer, A. K. Stalder, B. Ilgenstein, F. Beckmann, P. Thalmann, **M. Buscema**, N. Rohr, M. N. Holme, B. Müller, "Imaging tissues for biomedical research using the high-resolution micro-tomography system nanotom m ", *Proceedings of SPIE* **9967**, 99670Q (2016) (doi:10.1117/12.2237809)

S. Matviykiv, **M. Buscema**, H. Deyhle, T. Pfohl, A. Zumbuehl, T. Saxer, B. Müller, "X-ray micro computed tomography for the visualization of an atherosclerotic human coronary artery", *Journal of Physics: Conference Series* **849**, 012002 (2017) (doi:10.1088/1742-6596/849/1/012002)

S. Matviykiv, **M. Buscema**, T. Mészáros, G. Gerganova, T. Pfohl, A. Zumbuehl, J. Szebeni, B. Müller, "Liposomes - bio-inspired nano-containers for physically triggered targeted drug delivery ", *Proceedings of SPIE* **10162**, 101620A (2017) (doi:10.1117/12.2258378)

Peer-Reviewed Conference Abstracts

M. Buscema, H. Deyhle, T. Pfohl, S. E. Hieber, S. Matviykiv, A. Zumbuehl, B. Müller, "Studying shear-stress sensitive liposomes using microfluidics", *European Cells and Materials* **32**, 2, 31 (2016)

S. Matviykiv, **M. Buscema**, S. Bugna, T. Mészáros, J. Szebeni, A. Zumbuehl, B. Müller, "Complement activation of artificial liposomes about 100 nm in diameter", *European Cells and Materials* **32**, 2, 48 (2016)

M. Buscema, T. Pfohl, A. Zumbuehl, B. Müller, "Comparing microfluidic devices and established glass capillaries in laboratory-based X-ray scattering of liposomes as nano-containers for drug delivery", *European Cells and Materials* **28**, 6, 26 (2014)

List of selected Posters and Presentations

M. Buscema, M. N. Holme, G. Schulz, H. Deyhle, A. Khimchenko, P. Thalmann, S. E. Hieber, R. Schmitz, T. Weitkamp, A. Hipp, J. Herzen, F. Beckmann, J. A. Lobrinus, V. Kurtcuoglu, F. Rikhtegar, I. Zanette, T. Saxer, and B. Müller "Lumen determination in plaque containing vessels"; Annual Meeting of Swiss Society for Biomedical Engineering, 30 August 2017, Winterthur, Switzerland - POSTER PRESENTATION + "SMALL TALK"

M. Buscema, H. Deyhle, T. Pfohl, S. E. Hieber, G. Schulz, A. Zumbuehl, and B. Müller "Shear response of nano-containers for targeted vasodilation"; European & Global Summit for Cutting-Edge Medicine: Clinical Nanomedicine and Targeted Medicine (CLINAM2017), Basel, Switzerland, 7 - 10 May 2017 - POSTER PRESENTATION

M. Buscema, H. Deyhle, T. Pfohl, S. Matviykiv, G. Gerganova, T. Meszaros, S. Bugna, S. E. Hieber, G. Schulz, A. Zumbuehl, J. Szebeni and B. Müller "Tailoring mechano-sensitive liposomes for targeted vasodilation"; European Materials Research Society, 22–26 May 2017, Strasbourg, France - POSTER PRESENTATION

M. Buscema, S. Matviykiv, H. Deyhle, T. Pfohl, S. E. Hieber, A. Zumbuehl, and B. Müller "Studying shear-stress sensitive liposomes using microfluidics"; 22th Swiss Conference on Biomaterials and Regenerative Medicine, Schulthess Klinik, Zürich, Switzerland, 9 - 10 June 2016 - POSTER PRESENTATION

M. Buscema, Marzia Buscema, S. Matviykiv, Hans Deyhle, Thomas Pfohl, Andreas Zumbuehl, B. Müller "Spatially resolved small-angle X-ray scattering of mechano-sensitive nanometer-sized liposomes"; International Conference X-Ray Microscopy XRM2016, August 15 - 19, 2016, Oxford, UK - POSTER PRESENTATION

M. Buscema, G. Schulz, H. Deyhle, A. Khimchenko, A. Hipp, F. Beckmann, M. N. Holme, V. Kurtcouglu, S. Grabherr, T. Pfohl, A. Zumbuehl, T. Saxer, and B. Müller "Histology-validated X-ray tomography for imaging human coronary arteries"; SPIE Conference: Developments in X-Ray Tomography X, San Diego, USA, 28 - 31 August 2016 - ORAL PRESENTATION

M. Buscema, M. N. Holme, G. Schulz, H. Deyhle, A. Khimchenko, P. Thalmann, S. E. Hieber, R. Schmitz, T. Weitkamp, F. Beckmann, J. A. L., V. Kurtcuoglu, F. Rikhtegar, I. Zanette, T. Saxer, and B. Müller "X-ray tomography techniques for histology-validated 3D imaging of soft and hard tissues using plaques- containing blood vessels as example"; DESY Users' Meeting, 28 - 30 January 2015, Hamburg, Germany - POSTER PRESENTATION

M. Buscema, M. N. Holme, G. Schulz, H. Deyhle, A. Khimchenko, P. Thalmann, S. E. Hieber, R. Schmitz, T. Weitkamp, A. Hipp, J. Herzen, F. Beckmann, J. A. Lobrinus, V. Kurtcuoglu, F. Rikhtegar, I. Zanette, T. Saxer, and B. Müller "Understanding shear-stress sensitive nano-containers for drug delivery"; DBE Research Day, August 23, 2015, Basel, Switzerland - POSTER PRESENTATION

M. Buscema, M. N. Holme, F. Rikhtegar, V. Kurtcuoglu, A. Weinberger, S. Bugna, S. E. Hieber, J. Herzen, F. Beckmann, I. Zanette, T. Weitkamp, R. Urbani, T. Pfohl, A. Zumbuehl, T. Saxer and B. Müller "Determining the shear-stress threshold of mechano-sensitive nanocontainers for targeted vasodilatation"; Workshop on Biomechanics, 1 - 4 September 2014 Shima, Japan-POSTER PRESENTATION + "SMALL TALK"

M. Buscema, T. Pfohl, A. Zumbuehl, and B. Müller "Comparing microfluidic devices and established glass capillaries in laboratory based X-ray scattering of liposomes as nano-containers for drug delivery"; NRP 62 "Smart Materials" Tech Apéro, 16 May 2014 - POSTER PRESENTATION

1 Introduction

Myocardial infarction, also known as heart attack, is often caused by cardiovascular diseases and is responsible for about 7.4 million deaths every year [1]. Myocardial infarction is caused by coronary artery dysfunctions leading to the accumulation of white blood cells and the formation of fibro-fatty tissues, namely plaque, within the artery. Plaque is responsible for narrowing the artery. When the plaque ruptures, the blood clot forms which prevents blood supply to the heart muscle, causing heart attack. In emergency situations, one of the conventional protocol utilized to aid the patient includes the intravenous injection of a vasodilator, such as nitroglycerin, to widen the occluded arteries. Nitroglycerin injection allows blood perfusion to the heart, but its systemic administration leads to the decrease of peripheral vascular resistance with a consequent fall in blood pressure. The obstruction of the artery is responsible of a significant increase of the arterial flow velocity in diseased regions of the blood vessel compared to healthy ones [2]. Indeed, one can take advantage of the differences in the blood velocity to release the drug locally, using a purely physical trigger. In this scenario, a smart drug delivery at the obstruction site would be beneficial. Drug delivery systems concern all methods developed for administration of a pharmaceutical compound with therapeutic effect. Nanometer-sized materials, are suitable for developing drug delivery systems, as they cross organs and tissues. A drug delivery system can be fabricated using inorganic materials such as gold, iron oxide, or silica; organic polymers such as polystyrene (PS), polylactic acid (PLA), or poly(lactic-co-glycolic acid) (PLGA); or biopolymers such as proteins, carbohydrates, or phospholipids utilized to prepare liposomes. The use of liposomes as drug delivery vehicles is widespread. About twelve FDA-approved liposomal drugs are nowadays in clinical use [3]. Recently discovered artifical phospholipid-based shear-responsive nano-containers, namely Pad-PC-Pad, [4] are valuable candidates for releasing the drug at obstructed regions of arteries.

To improve the mechano-sensitivity of these liposomes a deep knowledge of the artery morphology including plaque structure and lumen area is essential. It would allow better understanding of the local shear stress changes at the site of the occlusion. The effect of the local shear stress on the nano-containers should then be investigated using suitable system, which can emulate a diseased blood vessel. Despite the clinical benefit of nano-carriers in targeted drug delivery, liposomal drugs are often recognized as foreign objects and hence are attacked by the immune system. Therefore, *in vitro* and *in vivo* assessments as a preclinical immune toxicity test is mandatory in the development of drug delivery systems.

1.1 Micro computed tomography for the determination of constricted arteries morphology

The understanding of human coronary artery diseases initiation and progression is often focused on the comprehension of the vessel dimensions, the plaque composition [5], as well as the detection of vulnerable plaque, the evaluation of thrombus, and the identification of neointima formation [6]. Another branch of interest in the investigation of cardiovascular disorders includes the assessment of coronary arteries morphology. The narrowing of the arteries leads to an increase of the vessel wall shear stress values at least one order of magnitude with respect to healthy blood vessels [7]. Proof-of-concept studies based on vasodilatory and thrombolytic drug release towards shear-activated nanoparticles based on phosphatidylcholine (PC)-based nano capsules [8], artificial phospholipids-based liposomes [4], and copolymers [9] have been reported. In order to tune the release of the drug by nano-containers, the shear stress parameters of both diseases and healthy regions of the coronary arteries are required.

Imaging techniques such as coronary computed tomography angiography and magnetic resonance are widely used as *in vivo* methods for the visualization and characterization of coronary artery occlusions. Although these techniques guarantee information on the physiological conditions of the coronary artery, they present limitation in terms of three dimensional evaluation of blood vessel anatomy [10], and do not reach the micrometer resolution, which is necessary for quantitative blood flow simulations.

Histology is considered the standard of reference for the *ex vivo* visualization and characterization of biological tissues down to sub-micrometer scale. However, it has been stated that histological imaging does not show the native morphology of the specimen [11]. On the contrary, X-ray micro computed tomography (µCT) is a well established imaging method allowing for non-destructive and three-dimensional (3D) rendering of biological specimens, including brain [12,13], nerves [14], cartilages [15] and coronary arteries [16, 17]. The visualization of diseased coronary arteries by means of µCT can elucidate the effect of the preparation steps for histology with respect to the artery morphology.

In section 2.1 we evaluate how the morphology of a segment cut from a plaque-containing human coronary artery is affected by formalin fixation, paraffin embedding, and decalcification which preludes the histological sectioning.

A diseased artery contains both high and low X-ray absorbing tissues, e.g. plaque and lumen, respectively. Therefore, conventional absorption µCT, which probes the imaginary part β of the refractive index $n = 1 - \delta + i\beta$, is not suited for the visualization of these specimens. Phase contrast µCT techniques, which are sensitive to phase shift of the X-rays passing through the specimen, and thus to the real part δ of the index of refraction, is better suited for these specimens. This is because δ varies less than β between the high- and low-absorbing tissues and thus the dynamic range of the phase contrast measurement is sufficient for simultaneous visualization. Herein, 3D tomography data of the calcified artery are acquired in phase contrast-mode, whereas scans of the decalcified artery are carried out in absorption contrast-mode.

The lumen cross section along the centerline is determined. For extracting the centerline a dedicated pipeline is implemented.

The results indicate that the lumen cross section obtained from the tomography data of the artery after formalin fixation allows for the determination of the plaque position along the artery. In contrast, paraffin embedding has a strong impact on the morphology of the artery lumen. The decalcification step damages internal and external regions of the artery, hampering the lumen segmentation. Furthermore, a comparison between tomography data acquired with advanced laboratory- and synchrotron radiation sources indicate that the use of a table-top tomography system is reasonable for the assessment of the artery lumen morphology.

The evaluation of the morphology of diseased arteries is the basis for blood flow simulations. Blood flow simulations provide the vessel wall shear stress values at both healthy and diseased regions of the artery [18]. The knowledge of the wall shear stress range is essential for the optimization of the mechanical properties of mechano-responsive liposomes. Consequently, it is advisable to investigate how the shear-responsive Pad-PC-Pad liposomes behave when subjected to an external perturbation, such as a shear stress gradient.

1.2 Shear-responsive liposomes investigated by means of microfluidics and small-angle X-ray scattering

Liposomes are made out of amphipathic molecules, which comprise a hydrophilic head and a hydrophobic tail. In aqueous solution, they assemble forming a closed phospholipid bilayer. Liposomes were described for the first time by Bangham and co-workers in 1965 [19] and soon suggested as drug delivery systems [20].

The artificial 1,3-diaminophospholipid, namely Pad-PC-Pad (nomenclature in Fedotenko *et al.* [21]) forms faceted liposomes [4, 22–24]. Pad-PC-Pad with a mean diameter of about 100 nm are produced here using the well established extrusion method [25].

The unusual shape of these liposomes can be regarded as an intermediate state of minimized energy between a spherical and a planar surface [26]. Under mechanical stimulation, the attenuation of the defects present in the membrane of Pad-PC-Pad liposomes might be responsible for their mechanosensitive properties. At constricted blood vessels, the blood velocity, and therefore the shear stress, is significantly increased. This enhanced shear stress can trigger the release of the drug carried by Pad-PC-Pad liposomes.

Hence, an *in vitro* model to test the behavior of Pad-PC-Pad under a shear stress gradient would be beneficial. Herein, microfluidics with a suitable design has been utilized allowing for the investigation of the liposomes under dynamic conditions. To probe the structural modifications of the liposomes while spatial and temporal conditions change, small-angle X-ray scattering (SAXS) has been combined with microfluidics. SAXS is based on the elastic scattering of the X-rays traveling through the sample. The scattered intensity I is collected as a function of the scattering vector q, which depends on the scattering angle θ as $q = 4\pi \sin(\theta)/\lambda$, being λ the X-rays wavelength.

In section 2.2, a microfluidic system which aims mimicking the geometry of a constricted blood vessels is reported. The microfluidic system consists of a micrometersized rectangular channel with an abrupt constriction in the middle. The channel, connected to a syringe pump system, allows tuning the flow rate, and thus the shear rate within the microfluidic device. Computational fluid dynamic simulations help to predict the profile of the velocity and the shear rate along the microfluidic device. Preliminary SAXS measurements to test the accessibility of the SAXS signal of the liposomes are performed in boron silicate glass capillary and in microfluidic devices. The results indicate that, despite liposome suspensions provide low contrast (lipid concentration of about 20 mg/mL), microfluidics and SAXS is a challenging but promising approach for probing these mechano-sensitive liposomes *in vitro*.

In section 2.3, the behavior of shear-sensitive liposomes Pad-PC-Pad by tuning the flow conditions within a microfluidic device is investigated. Two dimensional spatially resolved maps reveal the local variations of the scattering signal and guide the selection of regions within the device. In these regions, the scattering signal is radially integrated providing the scattering intensity I as a function of the scattering vector q at different flow velocities. The results show that under dynamic conditions, Pad-PC-Pad liposomes' structure is sensitive at different length scales.
Pad-PC-Pad liposomes' behavior under flow conditions is compared to liposomes prepared using dipalmitoylphosphatidylcholine (DPPC), which do not show any significant response.
These findings make Pad-PC-Pad liposomes promising as drug delivery system for targeting constricted blood vessels. However, the intravenous administration of liposomal drugs might cause adverse reactions of the immune system. Therefore, *in vitro* and *in vivo* immunological tests with the liposomes are required.

1.3 Immune toxicity tests with shear-responsive liposomes

Over almost five decades, researchers have improved liposome properties in terms of drug loading, rapid clearance, triggered release and transport of substances.
This progress has supported the idea of using liposomes as vehicles of anti-cancer [27], anti-fungal [28], anti-biotic [29] and anti-inflammatory drugs.
Despite the advantages mentioned above, liposomes are often recognized as foreign by the body due to their morphology and size [30] and, thus, can trigger the immune system which responds activating a biochemical cascade, named complement activation. The complement system [31] is responsible for attacking and destroying the suspected substance. Nevertheless, it might give rise to adverse immune reactions named complement activation-related pseudo-allergy (CARPA). CARPA has been widely used to describe mild to severe hypersensitivity reactions [32] in up to 45% of the patients [33]. These immune system reactions leads to abrupt variations of hemodynamic parameters including the pulmonary artery pressure and in the systemic arterial pressure which can be fatal for patients affected by cardiovascular pathologies. Liposomal drugs that cause adverse reaction of the immune system have been previously reported [32].
Hence, *in vitro* and *in vivo* assessments of CARPA, as a preclinical immune toxicity test in the development of liposomal drugs, are recommended.
Szebeni and co-workers have shown that among the main factors causing *in vitro* complement activation by liposomes are the inhomogeneity in size and lipid formulation, the presence of poly-ethylene glycol (PEG), the polyamino coating, and the

cholesterol in the bilayer membrane [30].

In section 2.4, an *in vitro* and *in vivo* study on the immunological response towards Pad-PC-Pad liposomes is reported.
Pad-PC-Pad liposomes concentrated and ten-fold diluted, with and without PEG, bare and loaded with nitroglycerin were incubated with human and porcine sera (*in vitro* assessments). Furthermore, the sera were incubated with saline (liposome buffer) and nitroglycerin (liposome cargo) used as negative controls as well as with Doxil, Abelcet (Food and Drug Adiministration-approved liposomal drugs) and zymosan as positive controls.
During the *in vitro* test, the three complement pathways through which the complement cascade might activate and the final branch of the cascade, are detected by measuring the increased level of dedicated proteins of the complement system.
The *in vitro* results allow us to state that i) the alternative pathway might activate the complement activation in presence of concentrate Pad-PC-Pad suspension containing both PEG and nitroglycerin, in agreement with the literature [34]; ii) diluted Pad-PC-Pad liposomes show comparable level of complement activation as reported for Doxil [35]. The *in vitro* findings are supported by the *in vivo* experiment indicating that Pad-PC-Pad liposomes loaded with a drug dosage up to three times the human therapeutic dose yield no significant changes in the continuously monitored hemodynamic parameters.

2 Results

2.1 Ex vivo evaluation of a plaque-containing human coronary artery via histology and high-resolution hard X-ray tomography

Scientific Reports, submitted

Ex vivo evaluation of a plaque-containing human coronary artery via histology and high-resolution hard X-ray tomography

Marzia Buscema[1], **Simone E. Hieber**[1,*], **Georg Schulz**[1], **Hans Deyhle**[1], **Alexander Hipp**[2], **Felix Beckmann** [2], **Johannes A. Lobrinus** [3], **Till Saxer** [4], **and Bert Müller**[1,**]

[1]Biomaterials Science Center, Department of Biomedical Engineering, University of Basel, Allschwil, Switzerland

[2]Institute of Materials Research, Helmholtz-Zentrum Geesthacht, Geesthacht, Germany

[3]Neuropathology Unit, University Hospital of Geneva, Geneva, Switzerland

[4]Faculty of Medicine, University of Geneva, Geneva, Switzerland

[*]simone.hieber@unibas.ch

[**]bert.mueller@unibas.ch

ABSTRACT

Atherosclerotic arteries exhibit characteristic constrictions and substantial deviations from cylindrical shape. Therefore, determining the artery's cross-section along the centerline is challenging, although high-resolution isotropic three-dimensional data are available. Herein, we apply high-resolution computed tomography in absorption and phase to a plaque-containing human artery *post-mortem*, through the course of the preparation stages for histology. We identify the impact of paraffin embedding and decalcification on the artery lumen. For automatic extraction of lumen's cross-section along centerline we present a dedicated pipeline. Comparing fixated tissue before and after paraffin embedding gives rise to shape changes with lumen reduction to 50-80%. The histological slicing induces further deformations with respect to tomography. Data acquired after decalcification show debris unintentionally distributed within the vessel preventing the reliable automatic lumen segmentation. Comparing tomography of laboratory- and synchrotron-radiation-based X rays by means of joint histogram analysis leads us to conclude that advanced desktop tomography is capable of quantifying the artery's lumen as an essential input for blood flow simulations. The results indicate that the most reliable lumen quantification is achieved by imaging the non-decalcified specimen fixed in formalin, using phase contrast modality and a dedicated processing pipeline. The results presented will initiate further studies on pathological cases.

Introduction

Blood vessels are commonly represented as a network of hollow tubes that transport blood through the human body. In a healthy situation, hemodynamics is characterized by a laminar flow and a wall shear stress in the order of 1 Pa[1]. Constrictions, for example as the result of atherosclerosis, give rise to a wall shear stress increased by at least one order of magnitude[2]. Recent communications have proposed exploiting increased wall shear stress for the targeted delivery of vasodilatory drugs[3,4]. For the clinical use, however, the threshold for drug release has to be determined. Consequently, the morphology of the vessel lumen in both healthy and diseased conditions has to be evaluated. *In vivo* imaging techniques such as coronary computed tomography angiography and magnetic resonance imaging are used widely for the visualization and quantification of coronary artery occlusions. Although these techniques yield information under physiological conditions, they are limited in terms of the three-dimensional evaluation of blood vessel anatomy[5], and they do not reach the micrometer precision required for meaningful flow simulations[6]. Therefore, researchers have applied expensive and time-consuming serial sectioning and the combination of two-dimensional micrographs[7]. This histological approach, however, relies on extended tissue preparation procedures, namely fixation, decalcification, embedding, and staining, which substantially modify the geometry of the vessel with respect to the *in vivo* situation. In order to reduce or correct the impact of the numerous preparation steps, and to achieve isotropic spatial resolution, several research teams have recently applied micro computed tomography (μCT)[8–12]. Using the conventional attenuation contrast, the plaque present in atherosclerotic vessels dominates X-ray absorption[6]. Typically, only the plaque becomes visible, whereas the vessel wall is almost transparent. Using reduced photon energies, the highly absorbing plaque causes severe streak artefacts, and the visualization of the vessel wall is compromised. Therefore, it is beneficial to use phase contrast, including X-ray grating-based interferometry (XGI)[13].

In the present communication, we report on μCT measurements of a diseased human artery segment subsequent to individual tissue preparation steps, i.e. formalin fixation, paraffin embedding, and decalcification. The tomography data were registered in order to determine local geometrical modifications. The lumen was segmented and the cross-section along the centerline derived. It should be noted that determining the centerline is a demanding undertaking because of the specific morphology in the constriction, and thus the convergence of widely used approaches is not guaranteed. In fact, most of the present approaches[14–16] follow points with the greatest distance to the surface, and they can abruptly change sites, leading to undesired jumps in the centerline. Thus, a robust iterative procedure for lumen quantification is proposed herein, dedicated to large deviations from the classic cylindrical shape, allowing the comparison of the lumen cross sections of the artery segment obtained at each of the tissue preparation steps to histology. The application of advanced methologies in the present study allow for a precise evaluation of a segment of a stenosed vessel lumen in three dimensions revealing the impact of the preparation procedure.

Results

Artery imaging and lumen segmentation

Table 1 details specimen preparation and the imaging parameters used. The images in Fig. 1a show a CT slice from Dataset #1 on the left, with its counterpart from Dataset #2 on the right. The counterpart slice was identified by the three-dimensional affine registration of Datasets #1 and #2[17]. The similarity of the anatomical structures is elucidated best by the plaque, represented by a black to yellow color. Formalin fixation led to a dominant artefact, namely the dark area within the vessel wall, caused by the presence of gas bubbles within the artery lumen, as displayed in the left image of Fig. 1a. On the other hand, paraffin embedding resulted in cracks within the plaque and air inclusions within the soft tissue, associated with streak artefacts (see Fig. 1a, right). A direct comparison of the diseased artery before and after paraffin embedding clearly indicates that only the plaque is preserved in size and shape, and the soft tissues substantially deform in a non-isotropic manner.

The image in Fig. 1b on the right displays a slice selected from the CT Dataset #3*A* obtained from the decalcified artery. The decalcification process substantially reduces the plaque, in which case streak artefacts are prevented. However, additional morphology modifications are present, including damage to the inner and outer (data not shown) parts of the vessel wall. Lumen segmentation failed where damage of the vessel wall was present. For comparison, the related slice from absorption-contrast data, i.e. Dataset #3*B*—see left part of Fig. 1b—with around two times worse spatial resolution is displayed. Likewise, this image indicates that the lumen cannot be segmented by means of the presently available automatic procedures.

The gradients in intensity and the large deviation from the cylindrical shape prevent the successful lumen segmentation by means of Frangi filtering[18], which is widely employed as vessel detector in 3D imaging. In order to determine cross-section along the artery, the lumen has been identified in undamaged parts, involving user interactions (*cf.* Methods, Lumen segmentation). We proposed a dedicated iterative procedure (*cf.* Fig. 10) to extract the centerline perpendicular to the cross-sections of successfully segmented lumen.

The centerline found after the first four ($i = 1, 2, 3, 4$) and the eighth ($i = 8$) iterations for the segmented lumen of Dataset #1 are shown in 2a.

Fig. 2b displays the centerline plotted within the corresponding artery lumen, oriented as in Fig. 2a (Fig. 2b, left), and rotated by 90° (Fig. 2b, right). The appendage shown in Fig. 2b left, represents a bifurcation present along the artery. Due to the artery bifurcation, the centerline $i = 1$, a dark blue-colored curve, exhibits a bulge that disappears at iteration $i = 8$, a light green-colored curve, where the condition $\rho < \mu$ is reached ($\mu = 0.3$ voxel). Convergence of the residual ρ for Dataset #1 is represented in Fig. 2c.

Fig. 3 shows the cross-sectional areas of Datasets #1 (black dots) and #2 (red dots) obtained as described in Methods section. The procedure was successfully applied to Dataset #1 for a length of approximately 15 mm out of 20 mm. The remaining artery of 5 mm length suffered from strong intensity gradients. Furthermore, the intensity gradient (see Fig. 1a, left) strongly affected lumen segmentation in the region between 8 and 10 mm. In Dataset #2, the artery could be segmented with success at a length of 9 mm that remained undamaged after paraffin embedding. The lower diagram in Fig. 3 shows the shrinkage of the artery as a function of the position along the centerline, whereby paraffin embedding caused a reduction in the cross-sectional area by values between about 15% and 65%. The diagram in Fig. 4 shows the results of the cross-sectional areas of Datasets #3*A* (orange dots) and #3*B* (blue dots). The two Dataset #3*A* and #3*B* are acquired from the same specimen measured using synchrotron radiation and conventional source in absorption contrast, respectively.

The comparison demonstrates that the data provide reliable values in a restricted part of the sample, namely from 1.2 to 2.6 mm. From position 2.6 to 4.5 mm (black dashed line), the cross-section of Dataset #3*B* was affected by 20-voxel-wide erosion/dilation, as a consequence of the results provided by lumen segmentation. From position 4.5 to 5.6 mm (red-colored dashed line), the cross-section obtained from Dataset #3*A* was affected by artefacts, which give rise to an overestimation of the cross-sectional area.

Laboratory-based µCT vs. synchrotron-radiation-based µCT imaging

Fig. 5 is a bivariate representation of the histograms from the registered Datasets #3*A* (bottom, left) and #3*B* (top, right). This joint histogram contains four clusters, each corresponding to the embedding material (paraffin), the fibrous tissue, the vessel wall, and the residual plaque, respectively. In both histograms, the paraffin (red-colored Gaussian peak) is clearly present and segmentable. It is, however, broader in the histogram of the Dataset #3*A* than in the histogram of Dataset #3*B*. The histogram of Dataset #3*B* distinguishes, in addition to the paraffin, between fibrous tissue (green-colored Gaussian peak), tissues forming the vessel wall (dark blue-colored Gaussian peak), and the remaining calcification (light blue-colored Gaussian peak), whereas the histogram of Dataset #3*A* displays a broad peak (gray-colored Gaussian peak). After filtering Dataset #3*A* using a Gaussian with $\sigma = 2$, the peaks in the histogram also exhibit the four Gaussian peaks, as exemplified in Fig. 6 bottom left.

Complementarity of tomographic imaging to histology

Fig. 7 contains optical micrographs of three histological slices (left), which were stained using H&E, Miller, and Masson's Trichrome. The corresponding CT-slices (right) from the Dataset #3*A* were selected on the basis of slice-to-volume registration[19]. On the images of the histological sections (Fig. 7, left), one finds the adventitial tissue on the outer part of the vessel wall. Muscular media is stained red-brown on H&E, gray on Miller and red-blue on Masson's Trichrome. Asymmetric decalcified plaque is visible on the left side of the artery. The artefacts caused by histological slicing are clearly visible, if one compares them with the tomography data. The artery walls, and especially the region where the decalcified plaque is present, are deformed.

Discussion

In order to visualize simultaneously lower and higher X-ray absorbing tissues in the diseased artery (Fig. 1a), phase contrast is better suited than absorption, due to the dependence of phase and absorption on the atomic number[20]. Thus, the plaque-containing artery segment was visualized with a phase contrast modality. Nevertheless, the high phaseshift of the plaque still gives rise to sporadic streak artefacts as clearly present in Datasets #1 and #2, *cf.* Fig. 1a.

It has been reported that formalin fixation causes tissue shrinkage of about $3-6\%$[21]. In the brain, formalin fixation gives rise to local strains as large as 15%[22]. Therefore, one can reasonably assume that the derived lumen of the artery segment will be smaller than in the *in vivo* situation. Highly intense hard X-rays often induce the formation and growth of air bubbles, especially at internal interfaces[23], which are found within the vessel walls (*cf.* Dataset #1), causing severe changes in the $\Delta\delta$ values.

Air bubble formation is circumvented by paraffin embedding, albeit this does lead to streak artefacts caused by cracks in the plaque and entrapped air in the soft tissue during the embedding process. H. J. Gundersen et al. have reported that dehydration, owing to paraffin embedding, can result in shrinkage of up to 30%[24]. In fact, the data represented in Fig. 1a confirms that paraffin embedding causes drastic deformation and shrinkage of the soft tissues while the morphology of the plaque remains unaffected.

The streak artefacts herein vanished as the result of the decalcification (*cf.* Fig. 1b), although lumen segmentation was hampered, as remains of the decalcified plaque infiltrated the lumen (data not shown). The morphology of the diseased part of the artery could therefore not be reliably quantified.

In order to investigate the impact of the individual tissue preparation steps, namely formalin-fixation, paraffin embedding and decalcification, the cross-sectional area along the artery lumen has to be determined. Since the artery cannot be reasonably described as a cylinder, its lumen was not parallel to the z-axis. Determining the center of each CT-slice is insufficient for extracting the centerline. Approaches reported in the literature, including piece-wise linear curves[14] and B-splines[15,16], are successful only to a limited extent due to the challenging geometry. Hence, it was necessary to search for alternative ways to extract the centerline along the bent and bifurcated diseased artery. The proposed algorithm revealed strong convergence. Application of the algorithm to the individual datasets indicates that the number of iterations depends not only on deviation from the cylindrical shape but also on the specimen preparation. For the Datasets #2 and #3A, the number of iterations was four and five, to reach a residual of less than 0.3 voxel, respectively, whereas for the Dataset #1 the artery bifurcation increased the number of iterations to eight (see Fig. 2). Dataset #3B contained some tissue debris in the segmented lumen, resulting after the decalcification process. This dataset was subjected to 20 voxel-wide erosion/dilation. The number of iterations to reach convergence increased to 29.

If one assumes that tissue shrinkage owing to formalin fixation is below 10%, as reported by Zehbe et al.[21], the plot of the cross-section along the centerline for Dataset #1 (Fig. 3, black dots) should yield the information on the artery lumen which reduces due to the formation of the plaque within the vessel wall. Contrary to formalin fixation, embedding the specimen in paraffin required substantial handling by the user, leading to deformation which influenced the morphology of the specimen, and thus the lumen cross section (*cf.* Fig. 3, red dots). In particular, the artery segment was embedded, de-embedded and re-embedded several times before obtaining a paraffin block without air bubbles entrapped.

The histogram data for the synchrotron radiation source does not allow distinguishing the information on the fibrous tissue, the vessel walls and the remaining plaque, which is instead possible observing the histogram data from the conventional X-ray source. As the filtering of the data acquired at the synchrotron radiation source highlights the peaks, the authors suspect that the proprietary Bruker reconstruction software contains a similar filtering feature. Therefore, one may hypothesize that filtering more effectively improves contrast than binning[25]. The main deduction from the joint histogram analysis is the almost linear correspondence of attenuation values obtained from Bruker and synchrotron, which implies that the conventional approach and the synchrotron radiation μCT shows comparable density resolution. Each modality gives rise to four components, namely the vessel wall, the fibrous tissue, the remaining plaque, and the embedding material (paraffin).

To validate the tomography data, histology is required. In the current literature, it has been claimed that with respect to H&E and Miller, Masson's Trichrome staining is the better choice for comparing histology with tomography data[6]. In the present study, no significant differences in terms of tissues identification could be found, so the arbitrary selection of one staining protocol was enough to validate the morphological findings from hard X-ray tomography. Although the features are co-resident in tomography and histology, one recognizes some additional deformations owing to cutting. These additional deformations can be seen better by the clipped slices displayed in Fig. 8.

Precise determination of the lumen from a plaque-containing human artery remains a subject for further research, since (i) *in vivo* methods do not reach the necessary micrometer resolution, (ii) the *post-mortem* evaluation using hard X-rays is not only suboptimal because formalin fixation results in moderate shrinkage, but also because it often induces bubble formation and growth during the data acquisition, (iii) when embedding the diseased artery into paraffin, bubble formation and growth can be prevented at the expense of massive local deformations, (iv) decalcification prevents the occurrence of streak artefacts, but often also induces tissue damage, which seriously compromises lumen extraction, and (v) the histological sections of decalcified arteries hardly represent the artery's morphology *in vivo*.

In conclusion, the present study proposes that the lumen from a plaque-containing artery should be based on formalin fixation and hard X-ray imaging. The formation and growth of gas bubbles in the formalin-fixed specimen can be reduced by using less intense X-ray beams with a photon energy as high as possible and adapted protocols for preparing the formalin solution and the tissue. Future research activities may include besides a reduction of imaging and preparations artefacts, a generalization of the proposed processing pipeline for further biomedical applications.

Methods

Specimen preparation

A 2.2-cm-long segment of a plaque-containing human coronary artery from the distal part of the anterior interventricular artery was explanted *post-mortem* from a female patient. *Ante-mortem* she consented to give her body for research purposes to the medical faculty of Lausanne University, Switzerland, the forensic department of which is a joint venture with the neighboring University of Geneva. Ethical approval for this study (Ethical Committee N° NAC 09-105) was provided by the Ethical Committee N.A.C. (Neuclid, Apsic, Chirurgie, Pathologie, Radiologie) of Geneva University Hospitals, Geneva. All methods were performed in accordance with relevant guidelines and regulations.

The artery segment was placed in a 2.0 mL Eppendorf tube and fixed with 4% paraformaldehyde (PFA). After imaging at the synchrotron radiation facility, the segment was embedded in paraffin. Prior to paraffin embedding, the surrounding tissues, mainly fatty tissue, were removed from the artery. To minimize the specimen diameter, the paraffin block was trimmed with a scalpel.

Later, the segment was de-embedded and then subjected to decalcification. The segment, fixed in 4% paraformaldehyde (PFA) for two days, was immersed in a decalcifying solution (87 vol% distilled water, 8 vol% formic acid, 5 vol% PFA) at a temperature of 37 °C. Decalcification was stopped when the decalcifying solution did not become white after mixing with 1 mL ammoniumoxalate (5%, vol/vol) and 1 mL ammonia (5%, vol/vol). Subsequently, the specimen was immersed in alcohol 70% for a period of five hours, dehydrated, embedded in paraffin at a temperature of 60 °C, and cooled down to room temperature.

Multimodal imaging of a plaque-containing human coronary artery

For simultaneous visualization of the highly X-ray absorbing plaque and the surrounding soft tissues, the human coronary artery segment was imaged using XGI-based µCT at the beamline P07 (PETRA III, DESY, Hamburg, Germany) once without and once with paraffin embedding. After decalcification and re-embedding into paraffin, the segment was visualized using the absorption-contrast-based tomography setup at the beamline P05 (PETRA III, DESY, Hamburg, Germany) and using the laboratory-based tomography system Skyscan 1275 (Bruker, Kontich, Belgium). Table 1 summarizes the preparation of the human artery segment and the parameters employed for data acquisition.

Laboratory-based tomography

Radiographs were recorded using a 3 Megapixel (1944 × 1536) CMOS camera featuring a pixel size of 75 µm. In total, 1200 projections (rotation angle increment of 0.3°) of the specimen were collected using an acceleration voltage of 15 kV and a beam current of 156 µA. Exposure time was set to 2.3 s. Effective pixel length corresponded to 5.2 µm. The tomograms were reconstructed using the manufacturer's software NRrecon, in which the Feldkamp algorithm[26] is implemented.

Synchrotron radiation-based double-grating interferometry

The P07 beamline is operated by Helmholtz-Zentrum Geesthacht, Germany. For phase imaging, the specimen was placed in a water bath to reduce artefacts owing to large X-ray wave front curvature at the specimen background interface, commonly referred to as "phase-wrapping" artefacts. As the size of the artery exceeded the field of view, it was moved vertically to the X-ray beam in 10 and 13 height steps for the formalin-fixated and paraffin-embedded states, respectively. Radiographic data were acquired at a photon energy of 45 keV. The double-crystal Si(111) monochromator (horizontal Laue geometry) was bent to match Rowland circle geometry. The beam-splitter grating (4.8 µm periodicity, Ni) was placed 31.4 cm away from the analyzer grating (2.4 µm periodicity, Au), corresponding to the third fractional Talbot order. The detection unit contained a 100 µm-thick $CdWO_4$ scintillator. The obtained optical image was magnified 5× and recorded by a CMOS camera, which was developed and produced at the Institute for Data Processing and Electronics (Institute of Technology, Karlsruhe, Germany) and uses a chip (CMOSIS, Antwerp, Belgium) with 20 megapixels (5120 × 3840) each 6.4 µm in size. The effective pixel length corresponded to 1.3 µm. For the formalin-fixed specimen, 900 projections were recorded over 360°, using an asymmetric rotation axis configuration, whereas 1200 projections were acquired for the paraffin-embedded specimen. At each angle, four phase-step images were taken over one period of the interference pattern. The exposure time was set to 0.2 s per phase step image. Prior to reconstruction, the phase tomograms were binned by factors of 2, 4, and 8 to simplify their handling and to improve the contrast[25]. After binning, phase-retrieval was performed by means of pixel-wise Fourier analysis. In order to reconstruct the phase tomograms, the differential data were integrated and then treated like attenuation-based data.

Synchrotron radiation-based tomography in absorption-contrast mode

The undulator source combined with the double-crystal monochromator, consisting of two Si(111) Bragg crystals, provided photons with an energy of 10 keV at the HZG beamline P05. The X-ray photons were converted into an optical image by a 100 µm-thick $CdWO_4$ scintillator and recorded by a camera (SciCam series) with a Kodak CCD chip KAF-09000 (3056 × 3056) comprising of 12 µm-wide pixels. The specimen-detector distance was set to 10 mm. In all, 1200 equiangular radiographs with an effective pixel length of 2.4 µm were recorded along 180°, with an exposure time of 1.5 s per projection. Prior to reconstruction, the projections were binned by a factor of two. The tomograms were obtained by the standard filtered back-projection algorithm.

Lumen segmentation

The lumen of the artery was determined from the tomography data, by means of the region-growing tool available in VG Studio MAX 2.1 (Volume Graphics GmbH, Heidelberg, Germany). Prior to this segmentation procedure, the data were smoothed using a median filter with a kernel size of 15. In order to visualize the impact of the filter, the segmented lumen cross section of all the CT-slices of Dataset #2 were compared before and after filtering (*cf.* Fig. 9, where lumen area of hundred CT-slices are shown). As the median filter caused slight and constant lumen enlargement over all the CT-slides, the lumen was eroded by one voxel. In case of Dataset #3*B* the segmented lumen was eroded/dilated by 20 voxels.

Cross section along the centerline determined from the segmented lumen

For the datasets listed in Table 1, the centerline of the artery segment was calculated. The individual steps in the iterative procedure used herein are represented in Fig. 10. The main steps are as follows:

1. **Initialization**. In the initialization step, the binarized data for the segmented artery lumen were loaded as a stack of 2D slices in the $x-y$-plane and stored as a 3D volume with isotropic resolution in the x-, y-, and z directions. The z-axis was oriented parallel to the artery.

2. **Compute centerline $c_{0,k}$ along the z-axis**. The centerline is discretized on points $c_{0,k}$ with $k = 1,...,N_k$, where N_k is the number of $x-y$-slices. The points $c_{0,k}$ correspond to the geometrical centers of the lumen for each slice orthogonal to the z-axis, and the resulting centerline $c_{0,k}$ is smoothed using a Gaussian filter ($\sigma = 20$). If the artery lumen is parallel to the z-axis, the centerline will be identified and no further steps will be necessary.

3. **Compute tangent vectors $\tau_{i,k}$ to $c_{i,k}$.** Tangent vectors $\tau_{i,k}$ to the centerline $c_{i,k}$ are computed using a finite difference second-order method.

4. **Compute planes $\pi_{i,k}$ orthogonal to the tangent vectors $\tau_{i,k}$.** In this step, the planes $\pi_{i,k}$ orthogonal to the tangent vectors $\tau_{i,k}$ are determined.

5. **Compute slice extraction on $\pi_{i,k}$ with the artery lumen to evaluate the $c_{i+1,k}$.** The slices are extracted using a linear interpolation. Here, a relaxation method is introduced to stabilize convergence for centerline identification. The extracted slices allow for calculating the centerline points $c_{j,k}$. In the next iteration, the centerline $c_{i+1,k}$ is determined by $c_{i+1,k} = (1-\beta)c_{j,k} + \beta c_{i,k}$, setting the relaxation parameter beta to $\beta = 0.5$ for the Datasets #1, #2, and #3A and $\beta = 0.9$ for the Dataset #3B and finally smoothed using the Gaussian filter. Thus, the residual ρ of the centerline $c_{i-1,k}$ and $c_{i,k}$ is computed, being $\rho = \sum_{k=1}^{N_k} d(c_{i-1,k}, c_{i,k})/N_k$ and i the number of iterations. If $\rho > \mu$, the algorithm returns to step 3, with the threshold μ = 0.3 voxel length being well below one voxel length; otherwise, the iteration loop is terminated and the centerline $c_{final,k}$, the tangent vectors $\tau_{final,k}$, and the planes $\pi_{final,k}$ are found.

6. **Cross-sectional areas along the artery lumen position**. In this step, slices orthogonal to the tangent vectors $\tau_{final,k}$ are extracted from the volumetric data of the artery lumen and their cross-sectional areas computed.

Histology

Histological sections were prepared from the decalcified artery according to a standard protocol[6]. Briefly, three slices, each about 2 µm thin, were cut along the artery. The slices were colored with three selected stains, namely hematoxylin and eosin (H&E), Miller or Masson's Trichrome, and mounted on glass slides. Images of the histological slides were taken using the Panoramic MIDI scanner (3DHistech, Sysmex Suisse) with a pixel resolution of 0.24 µm.

Data registration

One height step selected from Dataset #1 was successfully registered to the corresponding height step of Dataset #2, using an affine registration algorithm[27]. Three-dimensional registration was carried out using the classical maximization of mutual information[28,29] (see CT-slices in Fig. 1a). The same procedure was applied to the Datasets #3A and #3B (see CT-slices in Fig. 1b). To match the histology and tomography data (#3A), slice-to-volume registration[19] was performed. To facilitate the comparison with the tomography data, and prior to registration, the histology images were binned by a factor of 20 and converted to grayscale.

References

1. Doriot, P.-A. *et al.* In-vivo measurements of wall shear stress in human coronary arteries. *Coron. Artery Dis.* **11**, 495–502 (2000).

2. Cheng, C. *et al.* Large variations in absolute wall shear stress levels within one species and between species. *Atherosclerosis* **195**, 225–235 (2007).

3. Saxer, T., Zumbuehl, A. & Müller, B. The use of shear stress for targeted drug delivery. *Cardiovasc. Res.* **99**, 328–333 (2013).

4. Holme, M. N. *et al.* Shear-stress sensitive lenticular vesicles for targeted drug delivery. *Nat. Nanotechnol.* **7**, 536–543 (2012).

5. Hibi, K., Kimura, K. & Umemura, S. Clinical utility and significance of intravascular ultrasound and optical coherence tomography in guiding percutaneous coronary interventions. *Circ. J.* **79**, 24–33 (2014).

6. Holme, M. N. *et al.* Complementary x-ray tomography techniques for histology-validated 3d imaging of soft and hard tissues using plaque-containing blood vessels as examples. *Nat. Protoc.* **9**, 1401–1415 (2014).

7. Wintermark, M. *et al.* High-resolution ct imaging of carotid artery atherosclerotic plaques. *Am. J. Neuroradiol.* **29**, 875–882 (2008).

8. Hetterich, H. *et al.* X-ray phase-contrast computed tomography of human coronary arteries. *Investig. Radiol.* **50**, 686–694 (2015).

9. Hetterich, H. *et al.* Phase-contrast ct: qualitative and quantitative evaluation of atherosclerotic carotid artery plaque. *Radiology* **271**, 870–878 (2014).

10. Willner, M. *et al.* Phase-contrast hounsfield units of fixated and non-fixated soft-tissue samples. *PloS One* **10**, e0137016 (2015).

11. Walton, L. A. *et al.* Morphological characterisation of unstained and intact tissue micro-architecture by x-ray computed micro-and nano-tomography. *Sci. Rep.* **5**, 10074 (2015).

12. Pohle, K. *et al.* Characterization of non-calcified coronary atherosclerotic plaque by multi-detector row ct: comparison to ivus. *Atherosclerosis* **190**, 174–180 (2007).

13. Birnbacher, L. *et al.* Experimental realisation of high-sensitivity laboratory x-ray grating-based phase-contrast computed tomography. *Sci. Rep.* **6**, 24022 (2016).

14. Lacoste, C., Finet, G. & Magnin, I. E. Coronary tree extraction from x-ray angiograms using marked point processes. *Third IEEE Int. Symp. on Biomed. Imaging: Nano to Macro* 157–160 (2006).

15. Bouix, S., Siddiqi, K. & Tannenbaum, A. Flux driven automatic centerline extraction. *Med. Image Anal.* **9**, 209–221 (2005).

16. Frangi, A. F., Niessen, W. J., Nederkoorn, P. J., Elgersma, O. E. H. & Viergever, M. A. Three-dimensional model-based stenosis quantification of the carotid arteries from contrast-enhanced mr angiography. *Proc. IEEE Work. on Math. Meth. Biomed. Image Anal.* 110–118 (2000).

17. Müller, B. *et al.* Three-dimensional registration of tomography data for quantification in biomaterials science. *Int. J. Mater. Res.* **103**, 242–249 (2012).

18. Frangi, A. F., Niessen, W. J., Vincken, K. L. & Viergever, M. A. Multiscale vessel enhancement filtering. *Med. Image Comput. And Comput. Interv. - MICCAI98* 130–137 (1998).

19. Chicherova, N. *et al.* Automatic deformable registration of histological slides to μct volume data. *J. Microsc.* 49–61 (2018).

20. Momose, A., Takeda, T., Yoneyama, A., Koyama, I. & Itai, Y. Phase-contrast x-ray imaging using an x-ray interferometer for biological imaging. *Anal. Sci.* **17**, i527–i530 (2002).

21. Zehbe, R. *et al.* Going beyond histology. synchrotron micro-computed tomography as a methodology for biological tissue characterization: from tissue morphology to individual cells. *J. Royal Soc. Interface* **7**, 49–59 (2010).

22. Schulz, G. *et al.* Three-dimensional strain fields in human brain resulting from formalin fixation. *J. Neurosci. Methods* **202**, 17–27 (2011).

23. Lang, S. *et al.* Experimental comparison of grating- and propagation-based hard x-ray phase tomography of soft tissue. *J. Appl. Phys.* **116**, 154903 (2014).

24. Gundersen, H. J. G., Mirabile, R., Brown, D. & Boyce, R. W. *Chapter 8-Stereological Princ. Sampl. Proced. for Toxicol. Pathol.* 215–286 (2013).

25. Thurner, P., Beckmann, F. & Müller, B. An optimization procedure for spatial and density resolution in hard x-ray micro-computed tomography. *Nucl. Instrum. Methods Phys. Res. B* **225**, 599–603 (2004).

26. Feldkamp, L. A., Davis, L. C. & Kress, J. W. Practical cone-beam algorithm. *J. Opt. Soc. Am. A* **1**, 612–619 (1984).

27. Fierz, F. C. *et al.* The morphology of anisotropic 3d-printed hydroxyapatite scaffolds. *Biomaterials* **29**, 3799–3806 (2008).

28. Maes, F., Collignon, A., Vandermeulen, D., Marchal, G. & Suetens, P. Multimodality image registration by maximization of mutual information. *IEEE Transactions on Med. Imaging* **16**, 187–198 (1997).

29. Viola, P. & Wells, W. M. Alignment by maximization of mutual information. *Int. J. Comput. Vis.* **24**, 137–154 (1997).

Acknowledgements

This work was funded partially by the Swiss National Science Foundation (SNSF) project 126090 via the National Research Program (NRP) 62 'Smart Materials'. The experiments at DESY were performed at beamline P07 within the beamtime proposal I-20150360 EC and at beamline P05 within the beamtime proposal I-20170435 EC. The authors thank University Center of Legal Medicine, University of Lausanne, Switzerland for providing the human artery. The authors thank Christos Bikis for support during preparation of the specimen, and Anna Khimchenko is thanked for a number of valuable discussions.

Author contributions

M.B. and B.M. designed the study. T.S. prepared the specimen. J.A.L. provided the histological sections. M.B., G.S. and B.M. performed the measurements. A.H. and F.B. reconstructed the data. S.E.H. and M.B. developed the iterative centerline extraction. G.S. registered the tomography data. H.D. registered the histological sections to the CT-data. M.B. analysed the data and prepared the figures. M.B. and B.M. wrote the main part of the manuscript. All the authors discussed the results and contributed to the final manuscript.

Additional information

Competing interests: The authors declare no competing interests.

		Imaging parameters								
Label	**Specimen preparation**	**Modality**	**X-ray source**	E **[keV]**	**Detector type (pixel used)**	l [μ**m**]	N	t **[s]**	T **[h]**	$h(n)$ **[mm]**
#1	Formalin fixation	XGI phase	P07, DESY	45	CMOS (5120×3840)	1.3	1800	0.2^*	21.3	21.9 (10)
#2	Paraffin embedding	XGI phase	P07, DESY	45	CMOS (5120×3840)	1.3	1200	0.2^*	15.6	13.9 (6)
#3A	Decalcified	absorption	P05, DESY	10	CCD (3056×3056)	2.4	1200	$1.5^\#$	9.3	10.3 (4)
#3B	Decalcified	absorption	conventional	≤ 15	CMOS (1944×1536)	5.2	1200	$2.3^\#$	6.9	16.6 (4)

Table 1. Specimen used and imaging parameters E: photon energy; l: effective pixel length; N: number of projections; t^*: exposure time per phase step image; $t^\#$: exposure time per projection image; T: total artery scan time; h: total artery scan height; n: number of height steps.

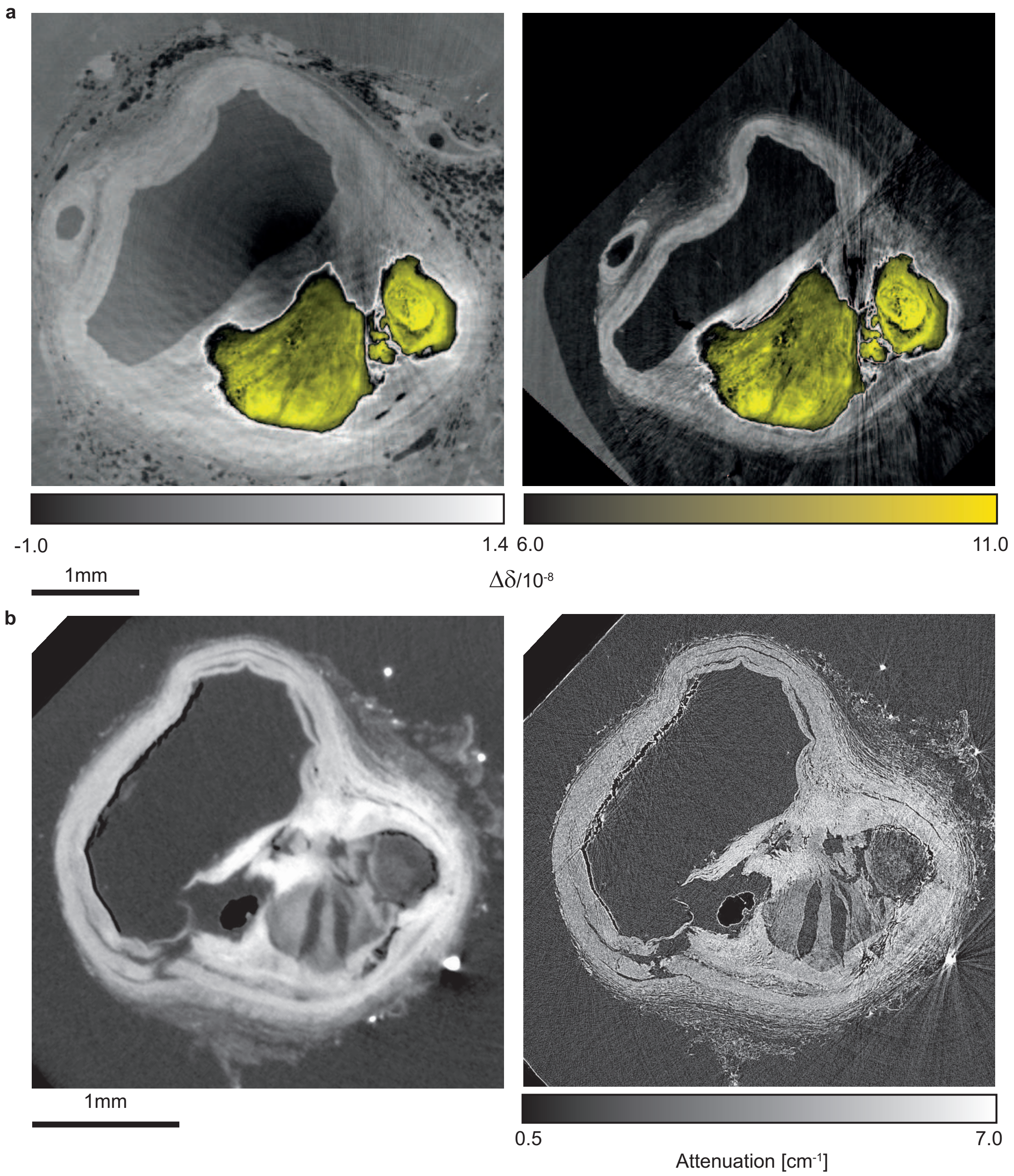

Figure 1. Selected slices from 3D-3D-registered CT-data before (a) and after decalcification (b) showing clearly the impact of water replacement. (a) The phase contrast CT-slice from Dataset #1 (left) and the corresponding one from Dataset #2 (right) were acquired using a double grating interferometer. In the images, the black to yellow color represents the plaque, which allows for registration, as its size and shape hardly change, whereas the vessel walls given in light gray exhibit massive shrinkage. (b) The absorption CT-slice from Dataset #3*A* (right) and the corresponding one from Dataset #3*B* (left) elucidate that lumen segmentation is a challenge and automatic procedures will probably fail due to vessel wall damage.

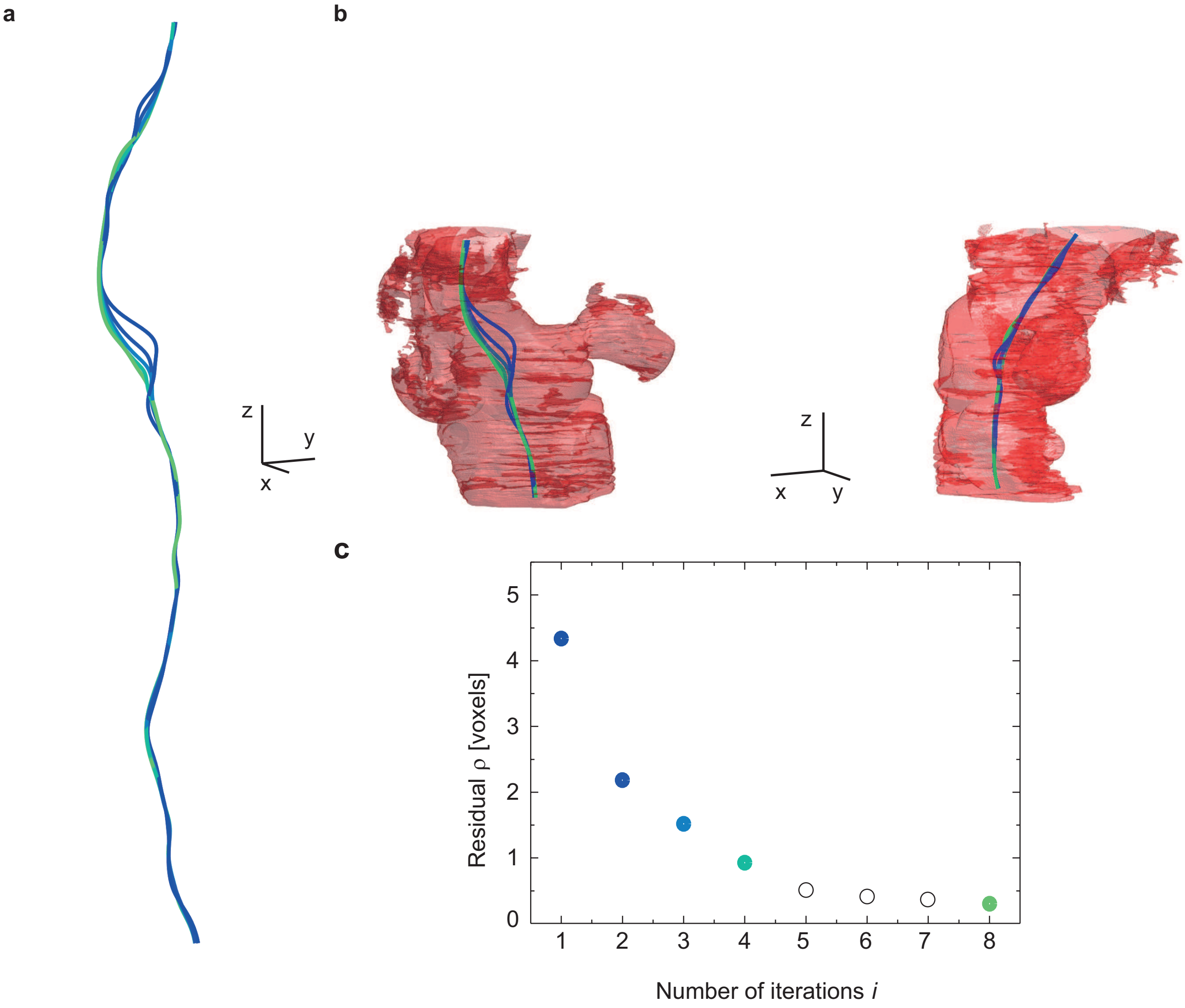

Figure 2. Rendering of the computed centerlines and the related residual ρ. (a) Results for the centerlines obtained from the first to the fourth as well as the eighth iterations, derived from Dataset #1, are shown in colors ranging from dark blue to light green. (b) Part of the centerlines from (a) and the corresponding lumen are viewed from two perspectives. (c) The color-coded residuals are plotted vs. the iteration steps. Iterations 5 to 7 are not represented in (a), and the orthogonal axes of the scale bar correspond to a length of 1 mm each.

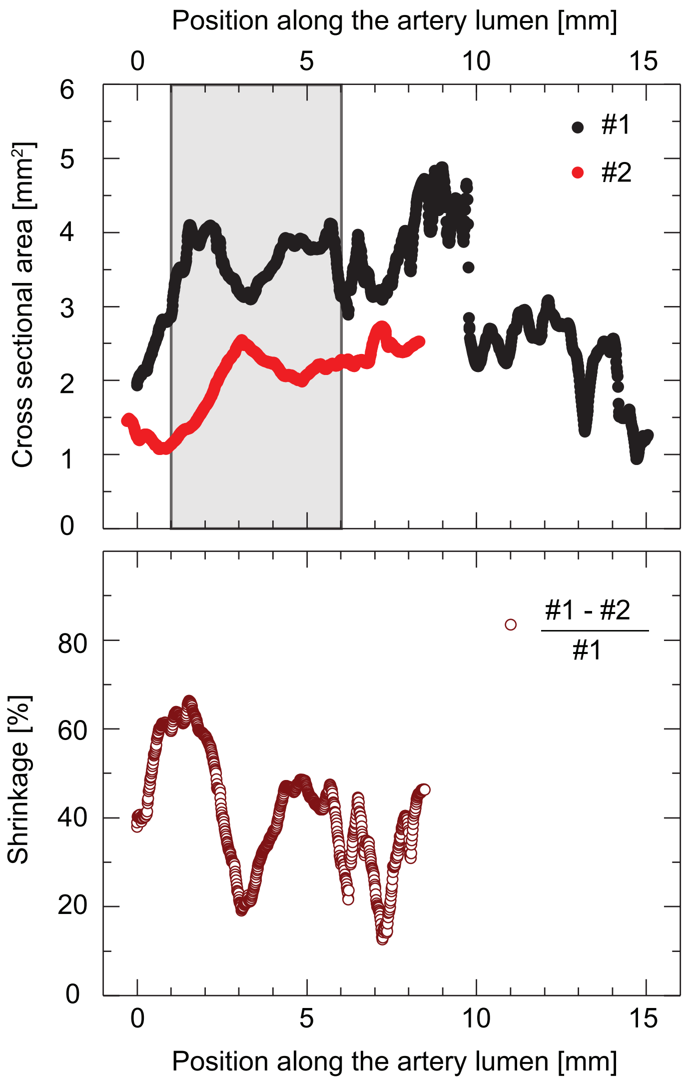

Figure 3. **Cross-sectional area obtained from Datasets #1 (black dots) and #2 (red dots) along the segmented artery lumen, and related shrinkage (brown hollow dots)**. The reduction of the cross-sectional area in Dataset #1 allowed for localizing the plaque-related constriction (top panel). Non-uniform shrinkage (bottom panel) as a result of paraffin embedding prevented any meaningful determination of stenosis. Using the plaque, the two datasets were perfectly aligned. The gray-shaded box (top panel) indicates the location of the data represented in Fig. 4.

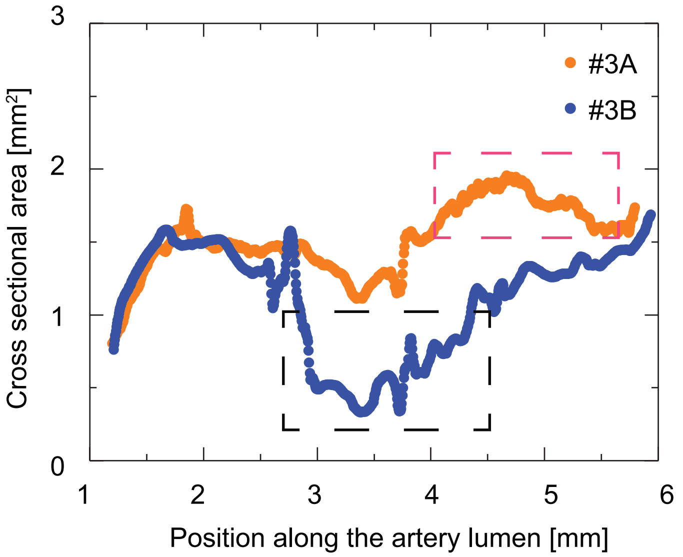

Figure 4. Cross-sectional area along the artery as derived from Dataset #3*A* (blue dots) and Dataset #3*B* (orange dots). The cross-sectional areas overlap from position 1.2 to 2.6 mm. Damage introduced during the re-embedding procedure hampered the lumen segmentation of both datasets. Red- and black-dashed boxes indicate regions where the lumen cross-section was either overestimated (Dataset #3*A*) or affected by 20-voxel-wide erosion/dilation (Dataset #3*B*).

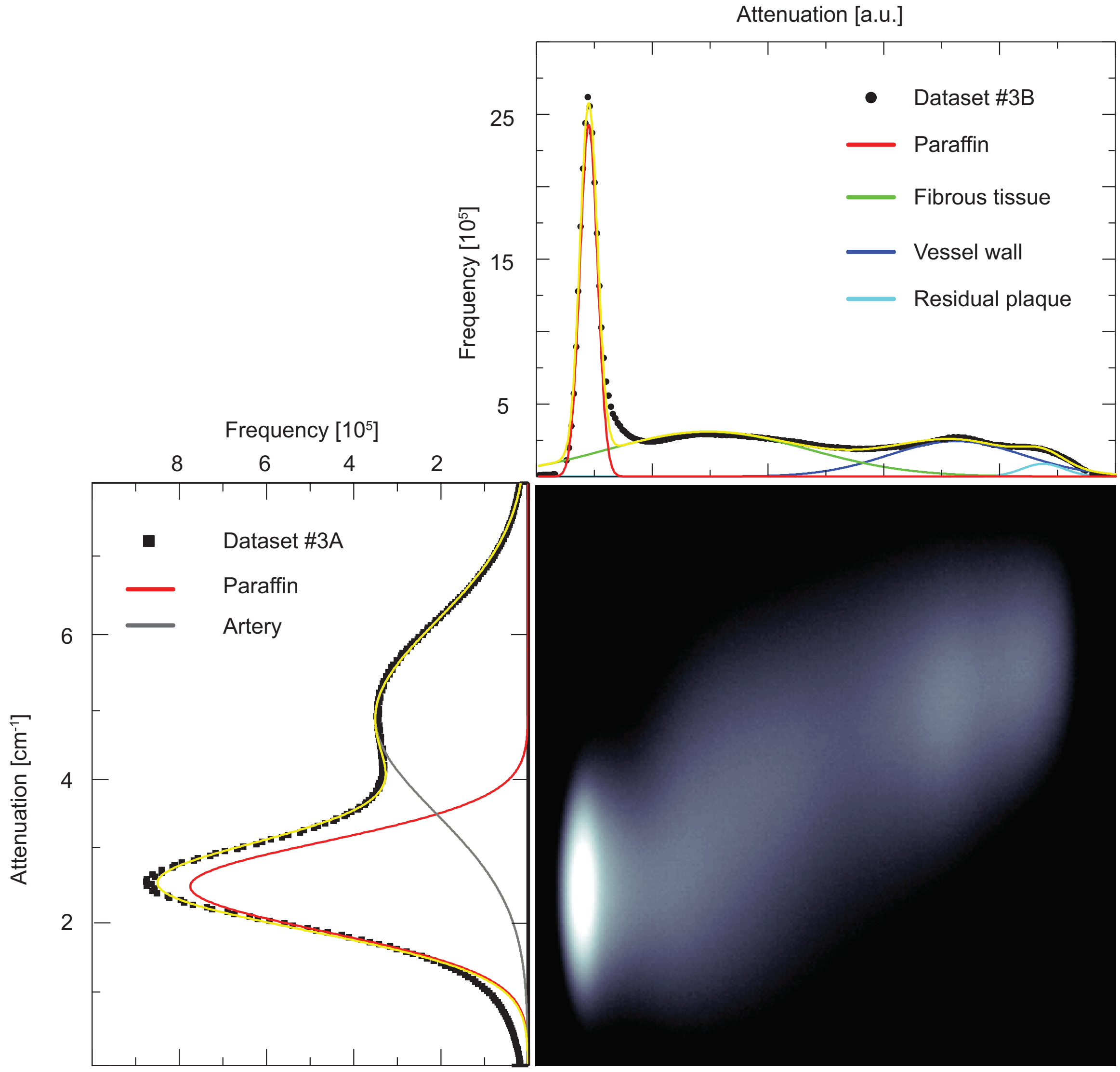

Figure 5. Joint histogram and individual histograms of the registered volumes from Datasets #3*A* **(bottom, left) and** #3*B* **(top, right)**. The peaks of the histograms were fitted with multi-Gaussian distributions (yellow curve). Whereas the individual histograms are given by a linear scale, the joint histogram is plotted on a logarithmic scale.

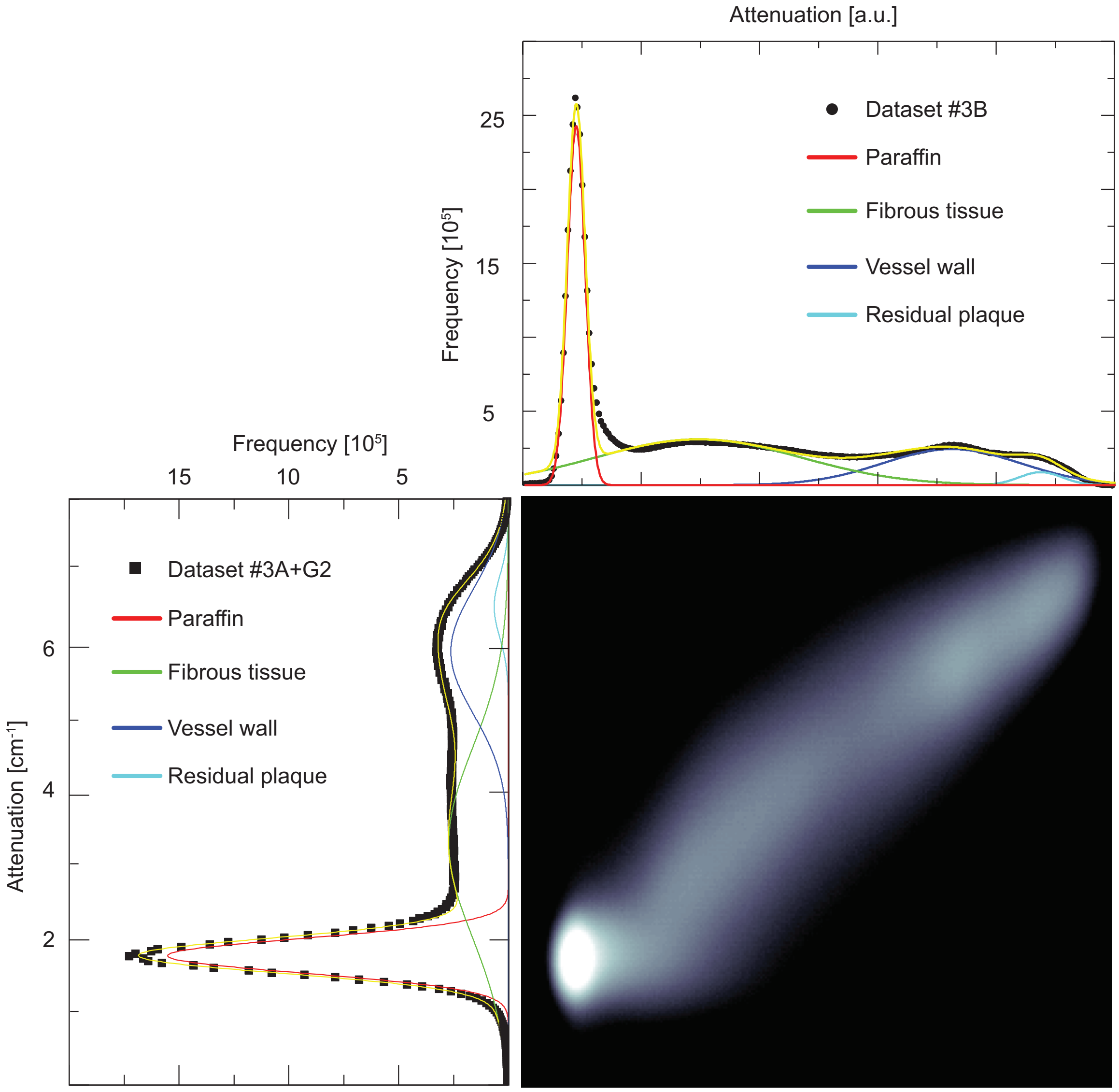

Figure 6. Joint histogram and individual histograms of the registered volumes from Datasets #3*A* after applying a Gaussian filter (bottom, left) and #3*B* (top, right). Filtering Dataset #3*A* gave rise to sharper peaks, which overlapped without filtering (see Fig. 5, bottom left).

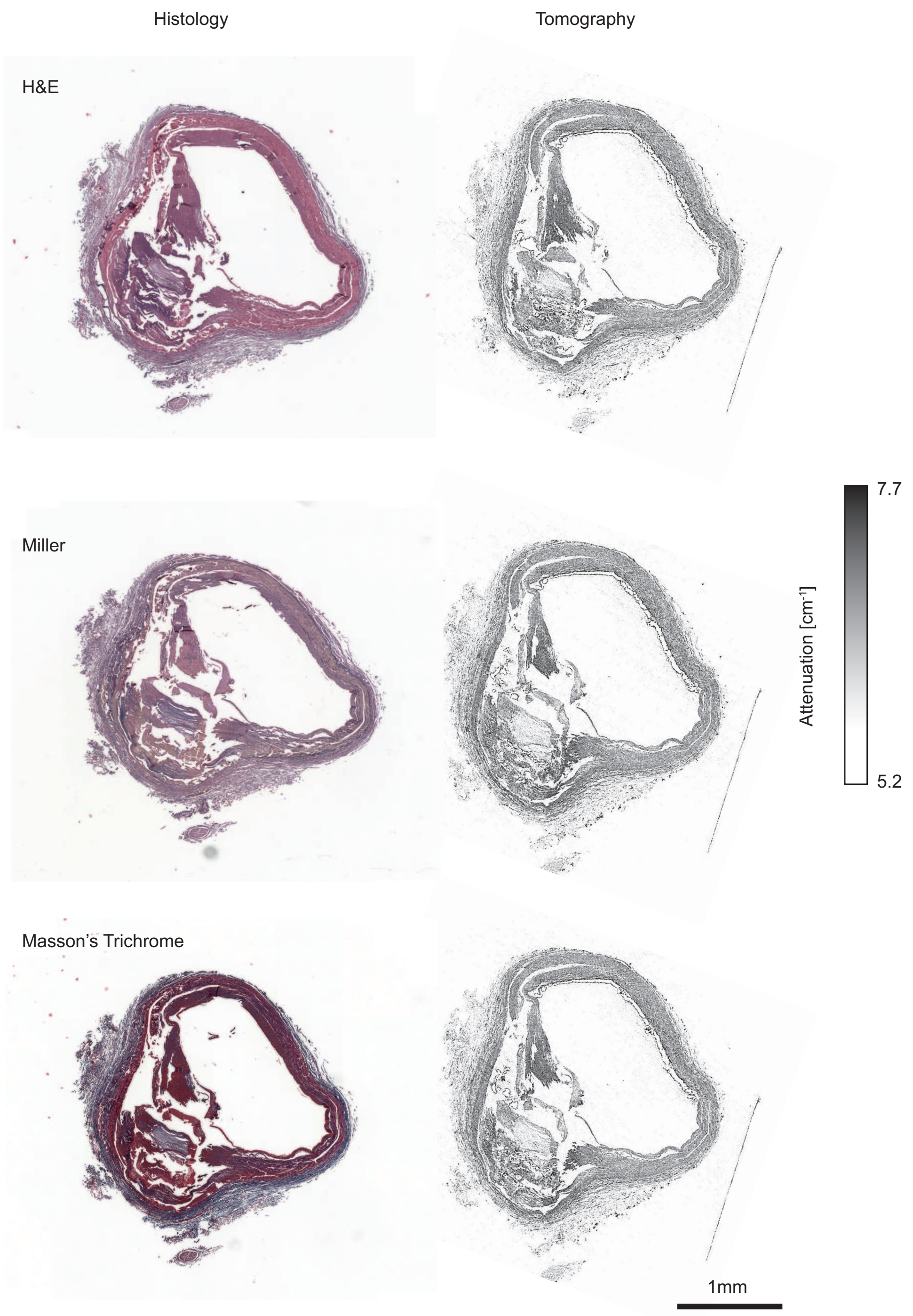

Figure 7. **Comparison of histology slices and their CT counterparts from Dataset #3*A*.** The selected micrographs of the histological sections (left) of the decalcified human coronary artery were stained using H&E, Miller, and Masson’s Trichrome. Tomography slices (right) matching the histological sections were identified by automatic registration.

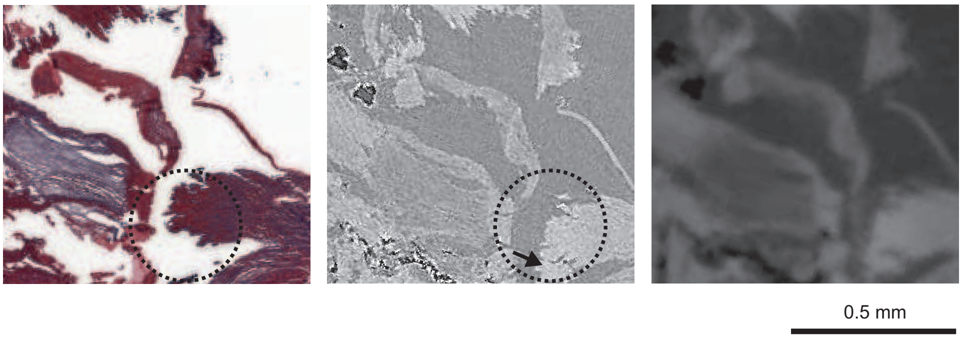

Figure 8. Magnified parts of the slices shown in Fig. 7. The histological slice, stained by Masson's Trichrome (left), exhibits anisotropic deformation resulting from the cutting process, as recognizable by comparison with the counterparts from the Datasets #3*A* (middle) and #3*B* (right). After histological sectioning, part of the tissue drastically deforms (dashed black circle) or is lost (black arrow).

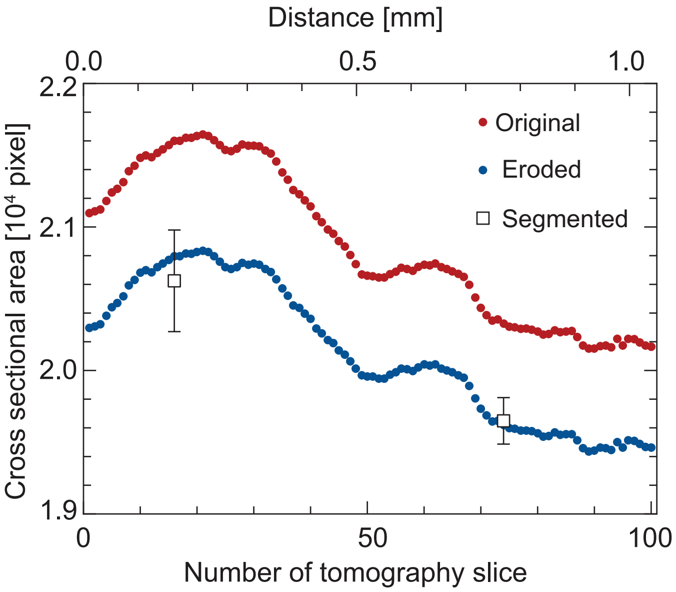

Figure 9. Effect of the median filter on the lumen area. Hundred tomography slides from Dataset #2 segmented after applying a median filter with a kernel size of 15 (red dots); two arbitrarily selected CT-slides, with no filter applied, segmented by three individuals (hollow squares, data presented as mean values, including error bars derived from the standard deviation, $n = 3$). Data filtering caused constant lumen enlargement over all the CT-slides, and therefore the lumen cross-section was eroded by one voxel (blue dots).

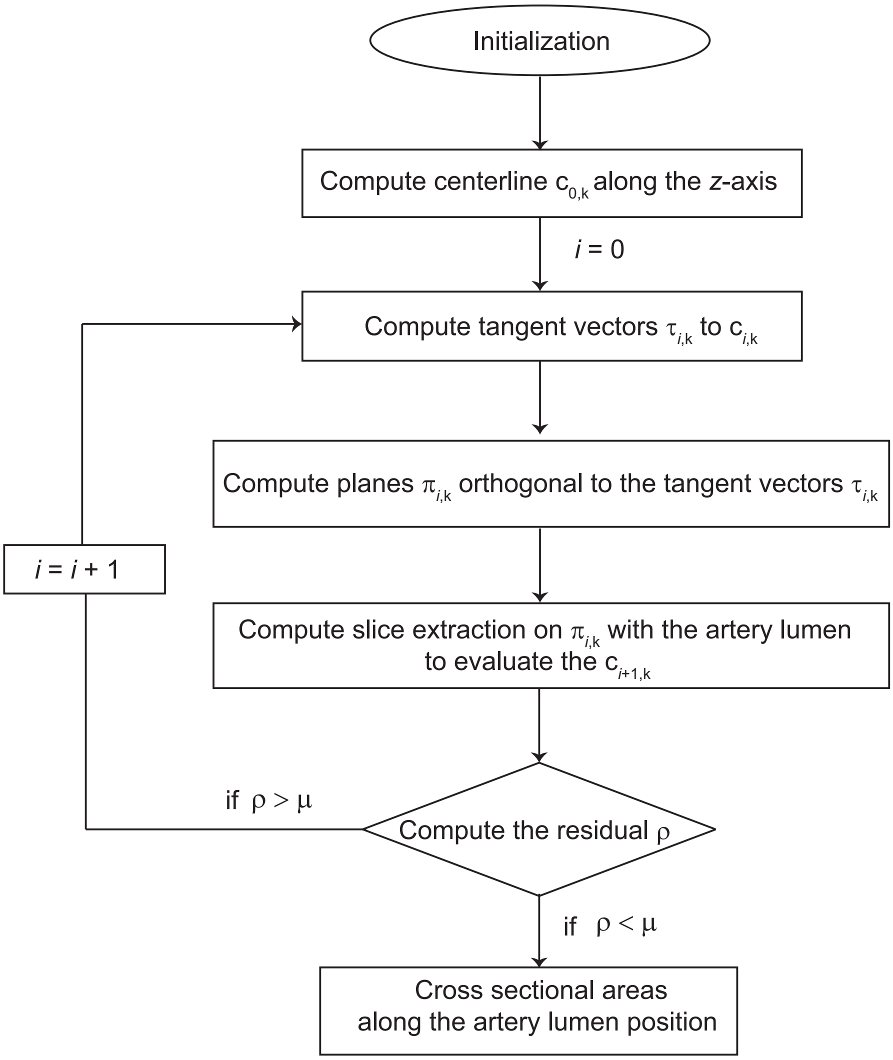

Figure 10. **Flow chart describing the implemented iterative procedure.** The flow chart shows the main steps employed to determine the centerline and the cross-sectional area along the artery lumen.

2.2 Characterization of mechano-sensitive nano-containers for targeted vasodilation

Published in Proceedings of SPIE

Characterization of mechano-sensitive nano-containers for targeted vasodilation

Marzia Buscema[a], Hans Deyhle[a], Thomas Pfohl[a], Simone E. Hieber[a], Andreas Zumbuehl[b], and Bert Müller*[a]
[a]Biomaterials Science Center, University of Basel, Gewerbestrasse 14, 4123 Allschwil, Switzerland;
[b]Department of Chemistry, University of Fribourg, Chemin du Musée 9, 1700 Fribourg, Switzerland

ABSTRACT

Cardiovascular diseases are the worldwide number one cause of mortality. The blood flow in diseased human coronary arteries differs from the blood flow in the healthy vessels. This fact should be used for designing targeted localized delivery of vasodilators with a purely physical drug release trigger. Thus, we have proposed mechano-sensitive liposomes as mechano-sensitive containers. One has to tailor the liposome's properties, so that containers are stable under physiological conditions in health, but release their cargo near the constricted vessels at body temperature. In order to determine the shear stress threshold for release, both the morphology of the healthy and diseased human arteries and the mechanical property of the liposomes have to be known. We have shown that micro computed tomography (μCT) techniques allow visualizing the lumen of human coronary arteries and provide the basis for flow simulations to extract the wall shear stress of healthy and stenosed regions in human coronary arteries. The behavior of the mechano-sensitive liposomes is currently investigated by means of microfluidics and spatially resolved small-angle X-ray scattering. The liposomes are injected into micro-channels mimicking *in vivo* situation. The scattering signal from the liposomes reveals information about their size, shape, and wall thickness.

Keywords: Drug delivery, liposome, micro computed tomography, stenosed human artery, mimicking, microfluidics, flow simulation, small-angle X-ray scattering

1. INTRODUCTION

Heart and blood vessel disease includes numerous problems, many of which are related to atherosclerosis. Atherosclerosis develops when the accumulation of white blood cells and the proliferation of intimal-smooth-muscle cells lead to a fibro-fatty plaque. Plaques create a thickening of the artery walls. The thickening narrows the vessel diameter, making it harder for blood to flow through. If a blood clot forms, it can block the blood flow leading to heart attack or stroke [1]. Infarcts are often treated with vasodilator drugs. A systemic administration of these substances has the drawback of lowering the patient's blood pressure, as all vessels including the veins increase in diameter. Therefore, a localized release of vasodilator is beneficial.

At the location of the constriction, the blood flow in diseased human coronary arteries differs from that in healthy arteries [2]. Therefore, one may overcome the systemic delivery of vasodilators and use the modified flow as a purely physical trigger for drug release. We have recently reported on a shear stress-sensitive liposomal formulation for the treatment of myocardial infarction via the release of a vasodilator drug [3]. The liposomes, around 100 nm in diameter, consist of phospholipids organized as shown in Figure 1. The novelty of such lentil-shaped liposomes relies on their sensitivity to local shear stress present in human arteries. At the constrictions, the blood velocity is significantly increased and thus the wall shear stress. The enhanced shear stress should trigger the drug release. To further enhance the technology, the morphology of stenosed human coronary arteries has to be determined with the necessary precision and the mechanical properties of the mechano-sensitive liposomes have to be investigated and adapted accordingly.

Micro computed tomography (μCT) allows non-destructively imaging hard and soft tissues. The spatial resolution reaches the true micrometer scale [4]. Absorption and phase contrast-based tomography modes are widely used to study hard tissues such as tooth crowns [5], and soft tissues such as brain [6] and tumors [7]. The μCT data of human coronary arteries [8, 9] allows for a deeper understanding of the morphology in healthy and diseased situations.

*bert.mueller@unibas.ch; phone +41 61 207 54 31; fax +41 61 265 96 99; www.bmc.unibas.ch

Bioinspiration, Biomimetics, and Bioreplication 2016, edited by Raúl J. Martín-Palma, Proc. of SPIE
Vol. 9797, 97970S · © 2016 SPIE · CCC code: 0277-786X/16/$18 · doi: 10.1117/12.2222033

Recently, the shear-stress sensitive liposomes were tested with respect to complement activation related-pseudoallergy (CARPA). Surprisingly, no significant complement activation was found in human sera and pig plasma [10]. Accordingly, animal experiments with pigs have shown much less reactions than liposomal formulations approved by the FDA [10].

To investigate the morphology of self-assembled phospholipid liposomes small-angle X-ray scattering (SAXS) is a powerful and widely used method. SAXS measurements are usually performed in wax-sealed glass capillaries [11, 12]. Information on liposome's parameters in terms of shape, size, and bilayer thickness can be extracted. Measurements in glass capillaries, however, do not allow for the detection of structural changes of the liposomes, while temporal and spatial conditions change. Microfluidics combined with SAXS is a valuable tool to investigate biological matter [13, 14]. It can be used to characterize how the liposomes react to changes in shear stress by tuning the flow conditions (shear rate) within the microfluidic device in order to mimic clinically relevant situations. The microfluidic system consists of a flexible, reproducible X-ray compatible device with a well-defined geometry to mimic healthy and diseased blood vessels. Knowing the artery morphology and the magnitude of the wall shear stress in normal and stenosed blood vessels, the mechanical properties of the liposomes can be investigated by adjusting the flow condition in the microfluidic device, accordingly.

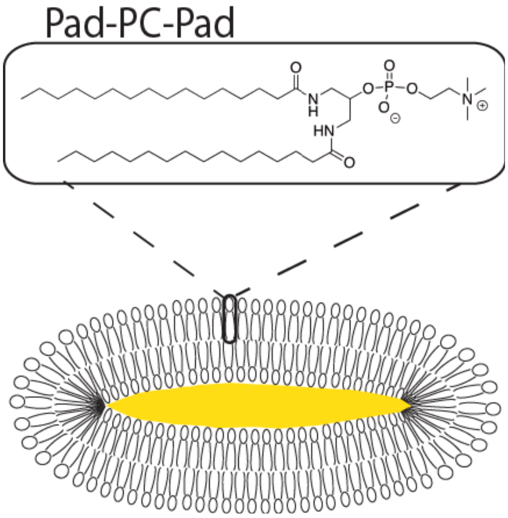

Figure 1. Schematic drawing of shear-stress sensitive phospholipid Pad-PC-Pad with an inner cavity shown in yellow, available for the vasodilator. At enhanced wall shear stress, as present in the diseased sections of arteries, the drug should be released. The chemical structure of the liposome is also given.

2. MATERIALS AND METHODS

2.1 Microfluidic device preparation

X-ray compatible microfluidic devices have been produced as previously described [15-17]. The main steps for preparing a microfluidic device are illustrated in Figure 2. Photolithography of SU-8 negative resist on silicon wafers was used to fabricate masters for the device fabrication. A layer of resist, either 50 or 100 µm thick, was exposed to UV-light through a photo mask containing the microfluidic design and was afterwards developed. PDMS and cross-linker were mixed at a ratio of 10:1 to form flexible replica stamps. The liquid PDMS mixture was poured on the photolithographic master and cured overnight at a temperature of 80 °C. Afterwards, the PDMS stamp was peeled off from the master. Norland Optical Adhesive 81 (NOA 81) was coated on a polyimide film 25 µm thick and the PDMS stamp was placed on the NOA 81 coated polyimide film in order to imprint the microfluidic structure into the NOA 81 coat. After exposure under UV light, λ = 366 nm, to crosslink NOA 81, the flexible PDMS stamp was peeled off. By using a puncher 0.75 mm in diameter, inlet and outlet holes were obtained. The microfluidic NOA 81/polyimide device was sealed with a second polyimide film, cured, and tightly bound for the related measurements.

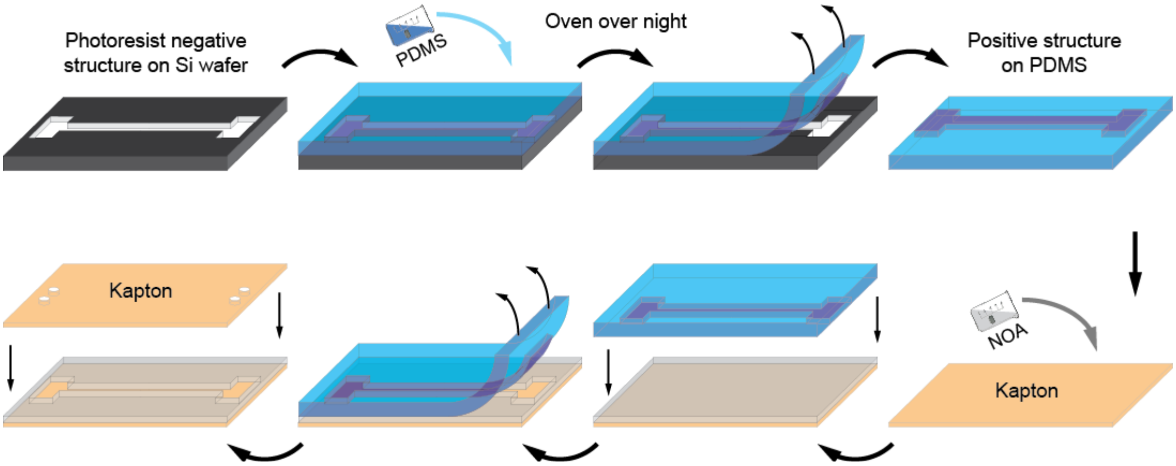

Figure 2. Microfluidic devices are fabricated using soft lithography combined with poly(di-methylsiloxane) (PDMS), UV-curable adhesive material NOA and polyimide film. The pattern of the microfluidic device consists of a main channel with a constriction to reproduce the morphology of a constricted blood vessel.

2.2 Micro computed tomography

Micro computed tomography measurements were performed on a nanotom® m (GE Sensing & Inspection Technology, GmbH, Wunstorf, Germany) with tungsten target at an acceleration voltage of 40 kV and beam current of 450 µA. Two devices, presenting 50 µm and 100 µm constrictions, respectively, were scanned. The devices were mounted on a high precision manipulator and continuously rotated by 360° through the X-ray beam, *cf.* Figure 3, within a period of eight minutes. During specimen rotation, 959 projections with an exposure time of 0.5 s each were acquired. Data reconstruction was performed with the supplier’s software datos|x 2.2.

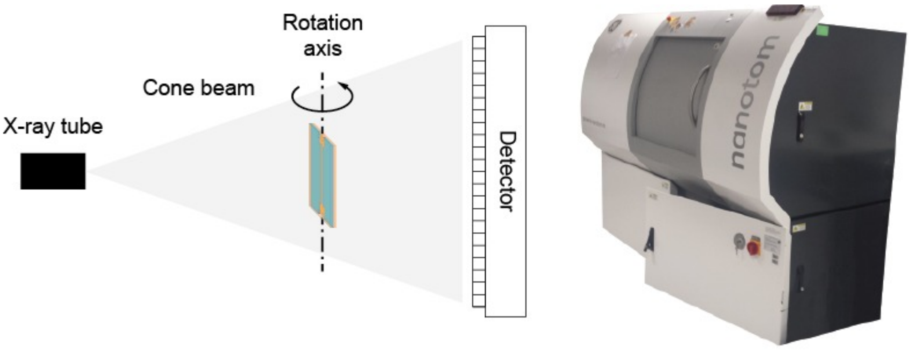

Figure 3. Schematic of µCT setup: the specimen is placed on a rotation axis between the X-ray source and the detector. A photograph of the laboratory µCT used for the present study, i.e. nanotom® m (GE Sensing & Inspection Technology, GmbH, Wunstorf, Germany) is represented.

2.3 Flow simulations

The simulations were carried out using COMSOL Multiphysics 4.3a (COMSOL, Palo Alto, CA, USA) by numerically solving partial differential equations using the finite element method (FEM) [18]. The used mesh of the microfluidic constriction consisted of 624’355 elements. The NAVIER-STOKES equation was solved for an incompressible fluid in laminar flow with the constriction geometry and no-slip boundary conditions at the walls. For the simulations a volume flow rate of $Q_{\text{in}} = 1$ µL/s, density $\rho = 1000$ kg/m^3, and dynamic viscosity $\eta = 8.9 \cdot 10^{-4}$ Pa·s were assumed.

2.4 Small-angle X-ray scattering

Laboratory-based X-ray source: In-house SAXS measurements were carried out using a Bruker Nanostar setup with a microfocus X-ray source (Cu-K_α-radiation, $\lambda = 1.54$ Å). The beam was collimated to reach a diameter of 200 µm. The signal was recorded using a 2D HiStar detector (Bruker AXS, Madison, WI, USA). The aqueous suspension containing the phospholipid liposomes was measured in a glass capillary under vacuum conditions. The glass capillary was 1.5 mm in diameter with a wall thickness of 10 µm.

Synchrotron radiation-based X-ray source: SAXS data were acquired at the cSAXS beamline of the Swiss Light Source storage ring (PSI, Villigen Switzerland) [19] using a photon energy of 12.4 keV. The X-ray beam was focused to 40 µm × 40 µm spot size at the specimen location, 2.2 m upstream from the PILATUS 2M detector [20]. Measurements were performed on microfluidic devices scanning 150 lines across the channel. The micro-channel was filled with a 20 mg/ml DPPC/DSPE-PEG$_{2000}$ (95:5 mol %) solution in PBS. Flow rate was adjusted to 0.083 µL/s by using a syringe pump system (Nemesys, Cetoni GmbH, Korbussen, Germany). The micro-channel was connected to the pump using Teflon (PTFE) tubing.

3. RESULTS AND DISCUSSION

3.1 Mimicking the geometry in human coronary artery by using microfluidic devices

High-resolution hard X-ray computed tomography in absorption mode has been used to characterize human coronary arteries [2, 8]. To better understand how the mechano-sensitive liposomes behave, when the diameter of a blood vessel changes, one may take advantage of microfluidic channels with suitable geometry. They are invaluable tools to mimic the *in vivo* situation. In Figure 4, the µCT-slice shows the cross section of a human diseased coronary artery (left image). One recognizes the vessel wall in light grey, the surrounding tissues represented by white and dark grey spots, and the plaque in white that obstructs the blood flow along the artery. We have also used µCT to visualize the cross sections of the microfluidic channels. The central and right parts of Figure 5 show selected cross sections of the micro-channels with two prepared geometries. The 200 µm-wide micro-channels decrease to 50 and 100 µm, respectively. These geometries with 75 % or 50 % narrowing are suitable to test liposome properties changing flow rate and temperature.

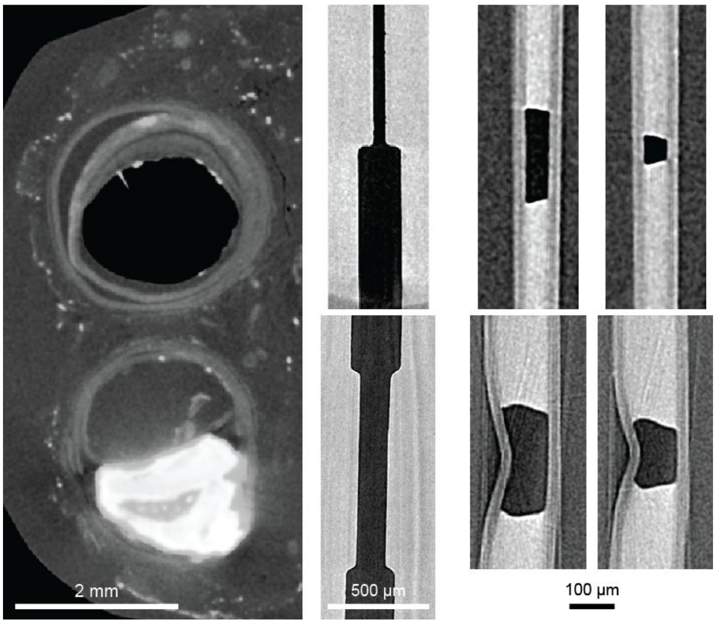

Figure 4. Left: A cross section through the µCT data of a human coronary artery with a cholesterol plaque (white) obstructing one of the vessels. The vessel walls (light grey) and the surrounding tissues (white and dark grey spots) are visible. Central column: View of two 200 µm-wide micro-channels with 50 µm- (top) and 100 µm-wide (bottom) constrictions. Right: Cross sections through same micro-channels at non-constricted and constricted locations.

3.2 Microfluidic flow simulation: Velocity and shear rate profiles

Flow simulations predict the profile of the shear stress in the microfluidic channel. Figure 5 shows the velocity and the shear rate profiles found by simulation and analytical solution for a microfluidic channel designed to mimic the healthy and constricted areas of a blood vessel. The channel width changes from 200 to 50 µm over a distance of 50 µm. The parabolic trend of the velocity field is present along the entire micro-channel. The velocity exhibits the highest value in the center of the device and decreases toward the walls. On the contrary, the shear rate is zero in the center of the channel and increase up to 7.7 10^4 s^{-1} at the walls according to the analytic solution, for a flow rate of 1 µL/s. The average shear rate yields 4.0 10^4 s^{-1}. The trend can be better visualized from the cross section of the micro-channel (see zoom), both in the wide and in the constricted areas of the micro-channel.

The shear stress in blood vessels is the fluid viscosity times the shear rate [21]. The liposome properties have to be tested in a shear stress range compatible with that found in constricted arteries. From flow simulation on human coronary arteries and µCT data, the shear stress in normal arteries was found to be below 5 Pa, whereas in the constricted areas it was above 15 Pa [2]. By adjusting the flow rate through the microfluidic device by means of the syringe pump, the desired shear stress in the channel can be realized. To mimic the *in vivo* wall shear stress conditions by using the microfluidic device with a constriction of 50 µm × 50 µm, the flow rate of the aqueous solution can be set to 0.021 µL/s, which corresponds to a shear stress of 1 Pa (healthy case). Higher flow rates, such as 0.33 µL/s, are used to get shear stresses of around 16 Pa (diseased case).

(a) Fluid velocity

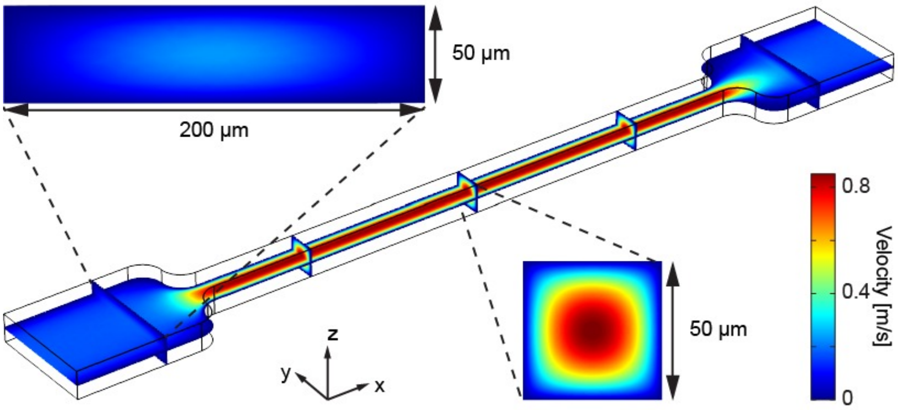

(b) Shear rate

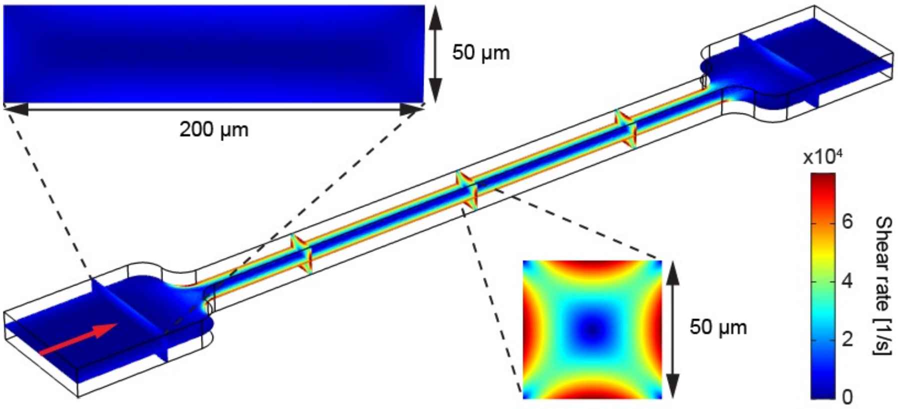

Figure 5. Flow simulations showing the velocity (a) and shear rate (b) profiles for a straight polyimide-based micro-channel 200 µm wide with a constriction 50 µm wide. The height is fixed to 50 µm. The flow rate is set to 1 µL/s. The red-colored arrow shows the flow direction. The zoom of cross sectional slide shows the analytical solution as insert.

3.3 SAXS measurements of liposomes in glass capillaries and microfluidic devices

Preliminary measurements to test the accessibility of SAXS signal of liposomes were performed both on glass capillaries in a lab setup and in microfluidic devices at a synchrotron radiation source (SLS, PSI, Villigen, Switzerland). Figure 6 shows, on the left side, a schematic experimental setup of the SAXS experiments. The SAXS-signal is collected on a 2D detector around a direct microfocus X-ray beam, which is absorbed in the beam stop. The SAXS signal is azimuthally integrated to obtain the q-plots, i.e. the intensity versus scattering angle. Results shown here were obtained from DPPC liposomes prepared as previously described [3]. The momentum transfer q (reciprocal space) is inversely proportional to the related real-space distances d ($d = 2\pi/q$). In Figure 6, right side, the q-plots from lab source (blue-colored triangles) measured in a glass capillary and synchrotron radiation source (red-colored dots) collected in the microfluidic device are shown. The scattering signals show similar behavior and are characterized by a shoulder for $q = 0.01$ Å^{-1} ($d = 62.8$ nm) indicating the average size of the liposomes; a bump is visible for higher q values, indicating the thickness of the phospholipid bilayer. It was found to be around $q = 0.1$ Å^{-1}, which corresponds to $d = 6.3$ nm. This value for DPPC in the L-alpha phase agrees with the value of 6.5 nm reported in literature [22, 23]. Similarity of the curves underlines the feasibility of phospholipid liposomes investigation in microfluidic devices. The obtained signal is comparable to that from measurements in glass capillaries, considered as standard, and no apparent interference from the devices could be found.

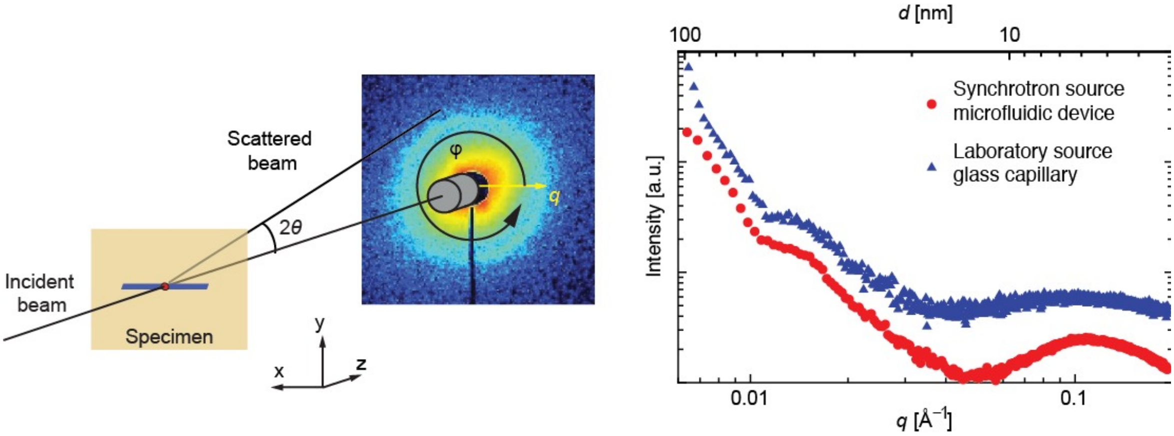

Figure 6. On the left, a scheme of the SAXS setup; on the right the q-plot showing the SAXS signal of liposomes measured both by using an in-house setup (blue-colored triangles) and at synchrotron radiation facility (red-colored dots). In house measurements were carried out in glass capillary, whereas the microfluidic channels were tested at the synchrotron radiation source.

4. SUMMARY AND CONCLUSION

The task to characterize the release of vasodilator drugs from mechano-sensitive containers of nanometer size is challenging. Since the phenomenon could not be reliably assessed within the patient, suitable *in vitro* set-ups have to be realized. Microfluidic systems belong to the key devices that allow for the detailed understanding of the release mechanisms and a related optimization of the liposomal formulations. Such devices have to mimic both healthy and diseased situations. Here, flow simulations of the designs are helpful, but also need to be complemented by experiments as a counterpart to the patient's blood vessels. To this end, high-resolution three-dimensional imaging of both devices and human arteries has to be performed in detail.

In a next step, the microfluidic systems are applied to study the behavior of liposomes along the simulated blood stream by means of spatially resolved X-ray scattering, which gives access to potential structural changes due to shear stress adaptations.

Although shear-sensitive liposomes are already identified, extensive scientific work has to be invested before the first patient might benefit from such a physically triggered mechanism. Thus, further experiments will be performed using techniques as rheology combined with both light scattering and small-angle neutron scattering and microfluidics combined with fluorescence microscopy.

Currently, the mechanical properties including the stiffness as function of temperature, polymer length, and nanocontainer size are locally studied using atomic force microscopy.

ACKNOWLEDGMENTS

This work was primarily funded by the Swiss National Science Foundation (SNSF) in the National Research Program (NRP) 62 'Smart Materials'. SAXS experiments were partially performed at the cSAXS beamline at SLS (PSI, Villigen, Switzerland). The financial contribution of the Swiss National Science Foundation in the frame of the R'equip initiative (316030 133802) to acquire the micro computed tomography system is also acknowledged. We thank M. Müller-Gerbl of the Department of Anatomy, University of Basel, who provided the human coronary arteries.

REFERENCES

[1] http://www.heart.org,

[2] Holme, M. N., Schulz, G., Deyhle, H., Weitkamp, T., Beckmann, F., Lobrinus, J. A., Rikhtegar, F., Kurtcuoglu, V., Zanette, I., Saxer, T., and Müller, B., "Complementary X-ray tomography techniques for histology-validated 3D imaging of soft and hard tissues using plaque-containing blood vessels as examples," Nature Protocols 9, 1401-1415 (2014).

[3] Holme, M. N., Fedotenko, I. A., Abegg, D., Althaus, J., Babel, L., Favarger, F., Reiter, R., Tanasescu, R., Zaffalon, P.-L., Ziegler, A., Müller, B., Saxer, T., and Zumbuehl, A., "Shear-stress sensitive lenticular vesicles for targeted drug delivery," Nature Nanotechnology 7, 536-543 (2012).

[4] Schulz, G., Waschkies, C., Pfeiffer, F., Zanette, I., Weitkamp, T., David, C., and Müller, B., "Multimodal imaging of human cerebellum - merging X-ray phase microtomography, magnetic resonance microscopy and histology," Sci. Rep. 2, 826 (2012).

[5] Deyhle, H., Dziadowiec, I., Kind, L., Thalmann, P., Schulz, G., and Müller, B., "Mineralization of early stage carious lesions in vitro - A quantitative approach," Dentistry Journal 3, 111-122 (2015).

[6] Schulz, G., Morel, A., Imholz, M. S., Deyhle, H., Weitkamp, T., Zanette, I., Pfeiffer, F., David, C., Müller-Gerbl, M., and Müller, B., "Evaluating the microstructure of human brain tissues using synchrotron radiation-based micro computed tomography," Proceedings of SPIE 7804, 78040F (2010).

[7] Lang, S., Dominietto, M., and Müller, B., "Visualization of tumor vessels using synchrotron radiation-based micro computed tomography " Journal of Physics: Conference Series 186, 012088 (2009).

[8] Buscema, M., Holme, M. N., Deyhle, H., Schulz, G., Schmitz, R., Thalmann, P., Hieber, S. E., Chicherova, N., Cattin, P. C., Beckmann, F., Herzen, J., Weitkamp, T., Saxer, T., and Müller, B., "Grating interferometry-based phase microtomography of atherosclerotic human arteries," Proceedings of SPIE 9212, 921203 (2014).

[9] Holme, M. N., Schulz, G., Deyhle, H., Hieber, S. E., Weitkamp, T., Beckmann, F., Herzen, J., Lobrinus, J. A., Montecucco, F., Mach, F., Zumbuehl, A., Saxer, T., and Müller, B., "Morphology of atherosclerotic coronary arteries," Proc. of SPIE 8506, 850609 (2012).

[10] Bugna, S., Buscema, M., Matviykiv, S., Urbanics, R., Weinberger, A., Meszaros, T., Szebeni, J., Zumbuehl, A., Saxer, T., and Müller, B., "Surprising lack of liposome-induced complement activation by artificial 1,3-diamidophospholipids in vitro," Nanomedicine: Nanotechnology, Biology and Medicine 12, 845-849 (2016).

[11] Soloviov, D. V., Gorshkova, Y. E., Ivankov, O. I., Zhigunov, A. N., Bulavin, L. A., V I Gordeliy, and Kuklin, A. I., "Ripple Phase Behavior in Mixtures of DPPC/POPC lipids: SAXS and SANS Studies," Journal of Physics: Conference Series 351, 012010 (2012).

[12] Sakaia, K., Tomizawaa, H., Tsuchiyaa, K., Ishidac, N., Sakaia, H., and Abea, M., "Characterizing the structural transition of cationic DPPC liposomes from the approach of TEM, SAXS and AFM measurements," Colloids and Surfaces B: Biointerfaces 67, 73-78 (2008).

[13] Köster, S., and Pfohl, T., "X-ray studies of biological matter in microfluidic environments," Mod. Phys. Lett. B 26, 1230018 (2012).

[14] Dootz, R., Toma, A. C., and Pfohl, T., "Structural and dynamic properties of linker histone H1 binding to DNA," Biomicrofluidics 5, 024104 (2011).

[15] Dootz, R., Evans, H., Köster, S., and Pfohl, T., "Rapid prototyping of X-ray microdiffraction compatible continuous microflow foils," Small 3, 96-100 (2007).

[16] Brennich, M. E., Nolting, J.-F., Dammann, C., Nöding, B., Bauch, S., Hermann, H., Pfohl, T., and Köster, S., "Dynamics of intermediate filament assembly followed in micro-flow by small angle x-ray scattering," Lab on a Chip 11, 708-716 (2011).

[17] Lutz-Bueno, V., Liebi, M., Zhao, J., Mezzenga, R., Pfohl, T., and Fischer, P., "Scanning-SAXS of microfluidic flows: nanostructural mapping of soft matter," Lab on a Chip (submitted)

[18] Laurell, T., and Lenshof, A., [Microscale Acoustofluidics], (2014).

[19] Bunk, O., Bech, M., Jensen, T. H., Feidenhans'l, R., Binderup, T., Menzel, A., and Pfeiffer, F., "Multimodal x-ray scatter imaging," New Journal of Physics 11, 123016 (2009).

[20] Kraft, P., Bergamaschi, A., Broennimann, C., Dinapoli, R., Eikenberry, E. F., Henrich, B., Johnson, I., Mozzanica, A., Schlepütz, C. M., Willmott, P. R., and Schmitt, B., "Performance of single-photon-counting PILATUS detector modules," Journal of Synchrotron Radiation 16, 368–75 (2009).

[21] Saxer, T., Zumbuehl, A., and Müller, B., "The use of shear stress for targeted drug delivery," Cardiovascular Research 99, 328-333 (2013).

[22] Lúcio, M., Bringezu, F., Reis, S., Lima, J. L. F. C., and Brezesinski, G., "Binding of Nonsteroidal Anti-inflammatory Drugs to DPPC: Structure and Thermodynamic Aspects," Langmuir 24, 4132-4139 (2008).

[23] Weinberger, A., Tanasescu, R., Stefaniu, C., Fedotenko, l. A., Favarger, F., Ishikawa, T., Brezesinski, G., Marques, C. M., and Zumbuehl, A., "Bilayer Properties of 1,3-Diamidophospholipids," Langmuir 31, 1879-1884 (2015).

2.3 Spatially resolved small-angle X-ray scattering for characterising mechano-responsive liposomes using microfluidics

Materials Today Bio, submitted

Spatially resolved small-angle X-ray scattering for characterising mechano-responsive liposomes using microfluidics

Marzia Buscema,[†] Hans Deyhle,[†] Thomas Pfohl,[†,‡] Andreas Zumbuehl,[¶,§] and Bert Müller[*,†]

†*Biomaterials Science Center, Department of Biomedical Engineering, University of Basel, Gewerbestrasse 14, CH-4123 Basel, Switzerland*

‡*Institute of Physics University of Freiburg, Freiburg, Germany*

¶*Department of Chemistry, University of Fribourg, Fribourg, Switzerland*

§*National Center of Competence in Research in Chemical Biology, Geneva, Switzerland*

E-mail: bert.mueller@unibas.ch

Abstract

Atherosclerosis gives rise to blood vessels occlusion associated with blood flow alteration and substantial increase of average wall shear stress. This modification was proved acting as a purely physical trigger for targeted vasodilator release from 1,3-diaminophospholipid (Pad-PC-Pad) liposomes. The flow-induced structural changes of the faceted liposomes, however, are completely fameless. Therefore, spatially resolved small-angle X-ray scattering was combined with microfluidics. The microfluidic device, designed to mimic a stenotic blood vessel, consisted of a horizontal channel 1 mm wide with a constriction 125 µm in diameter. Here, the changes of the average bilayer thickness and the mean size of the mechano-responsive liposomes have been detected locally.

Overall shape and bilayer thickness do change already near the constriction inlet, but the alteration is dominant near the outlet. At a flow rate of 0.2 µL/s, the liposome's bilayer thickness increased by 30% compared to the thickness well before the constriction and under static condition. The detected bilayer thickness increase of the faceted liposomes is in line with the mechanically induced loss of interdigitation between the phospholipid amide chains. These results imply that rather the gradient in the wall shear stress than the amplitude provokes structural changes of Pad-PC-Pad liposomes and the related drug release at stenosis.

1 Introduction

The local dysfunction of arteries can expose the patient to life-threatening situations, including myocardial infarction. Under these circumstances, the heart is insufficiently supplied with oxygen via coronary arteries. Here, the delivery of vasodilatory drugs is necessary and appropriate, although adverse effects have been reported.[1] Stenosed arteries have a drastically altered morphology with a cross section reduction, which causes a substantial increase of the blood flow velocity and, as a consequence, gives rise to an increase of the average wall shear stress by at least one order of magnitude.[2] It has been proposed that this increased shear stress could be used as a purely physical trigger for targeted vasodilator delivery.[3,4] Nanometer-sized liposomes are powerful containers to entrap, transport, and deliver a wide variety of drugs in the human body.[5,6] The artificial 1,3-diaminophospholipid, Pad-PC-Pad,[7] self-assembles in aqueous solution and can form faceted liposomes.[3,8] These liposomes are stable at rest and release their cargo at elevated shear stresses.[3] The mechanism behind, however, is hardly understood and was previously related to an attenuation of the defects in the contact lines between the facets of a vesicle.[9]

Understanding how Pad-PC-Pad liposomes behave under dynamic condition might support them as powerful drug delivery system. In fact recent studies report that the adverse effects observed for bare and nitroglycerin-loaded Pad-PC-Pad liposomes *in vitro* and *in vivo* are comparable or even lower than for established liposomal formulations.[10,11]

In order to quantitatively assess the structure of liposomes, many methods have been employed including nuclear magnetic resonance (NMR),[12] dynamic light scattering (DLS),[13] cryogenic transmission electron microscopy (Cryo-TEM),[14] as well as small-angle X-ray and neutron scattering (SAXS and SANS).[15,16] SAXS is of particular interest, because this method gives access to numerous characteristic quantities of the liposomes in terms of shape, size, lamellarity, and bilayer thickness. Garcia *et al.* have shown, for example, that SAXS allows not only for the determination of size, but also for the structural dependence on the solvent used and the osmotic shrinkage of a complex liposomal drug.[15] SAXS, however, does not only enable to perform static measurements, but the combination with microfluidics permits dynamic studies,[17] i.e. studies of the mechano-responsive properties of non-spherical liposomes. Spatially resolved SAXS using synchrotron radiation[18] has been applied to visualize human tissues in two dimensions[19,20] and more recently even in three dimensions.[21] It has been also used to map soft matter within a flow field.[22] The payoff of combining microfluidics and SAXS can been seen for diverse examples. One can observe the mixing of fluids,[23,24] the *in situ*, real-time changes of the structural properties of proteins,[23,25] of DNA,[26] of surfactant solutions,[27] of polymers,[28] of liquid crystals,[29] of worm-like micelles,[22] and of nanocapsules.[30] Poulos *et al.* have reported that under shear, the lamellar phases of highly concentrated complex surfactant solutions depend strongly on the fluid direction. Multi-lamellar phases, subjected to the identical flow fields, were insensitive to contraction-expansion flows.[27] The study, however, is limited to the flow field on the lamellar periodicity and does not include overall shape alterations.

Herein, we examine how Pad-PC-Pad liposomes in low-concentration suspension responds to shear-stress changes by tuning the flow conditions in a microfluidic device. The design of the device mimics constricted blood vessels. In this manner, the alterations of the shear stress in wide (healthy) and constricted (diseased) segments of the device (artery) can be simulated. It should be noted that three q-ranges were of specific interest and includes the size of the liposomes and the size of the bilayer thickness. The q-range of the SAXS pattern covers two orders of magnitude. The two-dimensional data represent the modifications in the flow field as a function of the flow rate.

2 Materials and Methods

2.1 Liposomes preparation

Two phospholipids, the commercially available natural 1,2-dipalmitoyl-*sn*-glycero-3-phosphatidylcholine (DPPC) with 5% molar DSPE-PEG2000 (Lipoid, Zug, Switzerland) and the 1,3-palmitoyl-amido-1,3-deoxy-*sn*-glycero-2-phosphatidylcholine (Pad-PC-Pad) synthesized according to the recently reported protocol,[7] were used to prepare liposomes. Briefly, the liposomes were formulated via the standard thin-film method[31,32] and hydrated with ultra-pure water. Each suspension obtained has a lipid content of 20 mg/mL, which corresponds to the highest concentration achievable using Pad-PC-Pad. The suspensions were freeze-thawed in a twelve-step series of liquid nitrogen cooling and water bath heating (60 °C). To obtain liposomes with a diameter of about 100 nm with a narrow size distribution, multiple barrel extrusions using Liposofast LF-50 (Avestin Inc., Canada) through track-edged polycarbonate filter membranes (Whatman Nucleopore, Sigma-Aldrich, Buchs, Switzerland) were applied. The pore sizes were reduced from 400 nm (five times) via 200 nm (five times) to 100 nm (15 times).

2.2 Liposomes characterization

The lipid concentration of the two formulations was determined using the phosphate test.[33] Size and size distribution of the liposomes were quantified by means of dynamic light scattering (DLS) using a Delsa Nano C (Beckman Coulter, USA). DLS measurements were performed at a temperature of 25 °C, using two laser diodes working at a wavelength of 658 nm. The scattering angle was set to 165 degrees. Cryo-TEM images of Pad-PC-Pad liposomal suspension were taken by mounting the liposomal suspension on glow-discharged holey carbon grids, quickly frozen by a Cryoplunge CP3 system (Gatan, USA), and transferred to a JEM2200FS transmission electron microscope (JEOL, Japan) using a Gatan626 cryo-holder. Cryo-TEM micrographs were recorded at an acceleration voltage of 200 kV at a magnification of 20,000, 4-8 μm under-focus, and a dose of $10\,\text{electrons}/\text{Å}^2$, using a F416 CMOS detector (TVIPS, Germany).

2.3 Microfluidic device fabrication

X-ray compatible microfluidic devices were prepared as reported previously.[22] Briefly, photolithography of SU-8 negative resist (Nano SU-8 100, MicroChem Corp., MA, USA) on Si wafers was used to fabricate the masters. A layer of 250 µm thick photoresist was exposed to UV light through a photo mask with the microfluidic design and was afterwards developed. The microfluidic device design consisted of a horizontal channel of 1000 µm width with a constriction in the middle 2000 µm long. Two designs were realized, with constriction widths of 125 µm and 250 µm. Polydimethylsiloxane (PDMS, Sylgard 184, Dow Corning Corp., Midland, USA) and crosslinker were mixed at a ratio of 10:1 to form flexible replica stamps. The liquid PDMS mixture was poured on the photolithographic master and cured overnight at a temperature of 80 °C. Afterwards, the PDMS stamp was peeled off from the master. Norland Optical Adhesive 81 (Norland Products Inc., Cranbury, USA) was poured on a polyimide film of a thickness of 25 µm (Goodfellow Corp., Cambridge, UK). PDMS stamp was placed on the NOA 81 coated polyimide film in order to imprint the microfluidic structure into the NOA 81 coat. After 1 min exposure to UV light, $\lambda = 366$ nm, to crosslink NOA 81, the flexible PDMS stamp was peeled off. By using a puncher 0.75 mm in diameter, inlet and outlet holes were obtained. The microfluidic NOA 81/polyimide film was then sealed with a second polyimide film with a thickness of 25 µm.

2.4 SAXS measurements

The spatially resolved SAXS measurements were performed at the cSAXS beamline at the Swiss Light Source (PSI, Villigen, Switzerland). The X-ray beam was focused to 25 µm × 50 µm (vertical × horizontal) spot size at the specimen location, the photon energy was set to 11.2 keV (λ =1.1 Å), and the sample-detector distance to 7.102 m, determined by the first scattering order of a silver behenate specimen. The scattering signal was recorded using the Pilatus 2M detector[34] (pixel size: 172 µm × 172 µm). Dynamic spatially resolved SAXS measurements of the liposomal suspensions were performed using microfluidic devices mounted on an aluminum/polyetheretherketone/aluminum sample holder. Two-dimensional (2D) scans were realized line-by-line by continuously moving the device in horizontal direction, while the detector recorded the data in burst mode. 48 (v) × 96 (h) points at step size 25 µm (v) × 50 µm (h) were acquired in a pre-selected region of the microfluidic device with an exposure time of 1.5 s per point. The data were processed using the Matlab package available from the beamline (https://www.psi.ch/sls/csaxs/software). During the experiment, the flow rates were adjusted using a syringe pump system (Nemesys, Cetoni GmbH, Korbussen, Germany) connected to the microchannel using polytetrafluoroethylene (PTFE) tubing. For the point-wise background correction, the scattering signal of ultra-pure water in the microfluidic device for all the measured flow rates was recorded before the acquisition of the SAXS signal of the liposomal suspensions. For the microfluidic device with a rectangular channel cross-section, the wall shear rates γ were calculated from the volumetric flow rates v using the following equation:[30]

$$\gamma = 6v/h^2w \tag{1}$$

with γ the shear rate [s^{-1}], v the volumetric flow rate [µL/s], and w and h the width and height [µm] of the channel, respectively.

In addition, static SAXS measurements of the two liposomal suspensions and the ultra-pure water were carried out in boron silicate glass capillaries (Hilgenberg, Malsfeld, Germany) having an outer diameter of 1.5 mm and wall thickness of 0.01 mm using the parameters given above.

3 Results and Discussion

3.1 Liposomes characterization

The final concentration of Pad-PC-Pad liposomes was (19.6 ± 1.3) mg/mL, whereas that of DPPC/DSPE-PEG was (20.2 ± 6.5) mg/mL.

The DLS results showed a mean diameter of (131.6 ± 0.9) nm for Pad-PC-Pad and a polydispersity index (PDI) of (0.103 ± 0.009), whereas for DPPC/DSPE-PEG a mean diameter of (101.3 ± 0.5) nm and PDI of (0.256 ± 0.005) was found.

The Cryo-TEM micrograph in Figure 1 shows the morphology of Pad-PC-Pad, characterized by faceted and lentil-like shape.[3,9] The overall diameter appears to be in the range 100 nm to 200 nm, in agreement with DLS. The presence of round liposomes can be linked to the projective nature of cryo-TEM, as lenticular shapes seen top-on or slightly tilted will appear round. Nevertheless, the presence of spherical liposomes cannot be excluded.

3.2 SAXS measurement under static condition

The investigated q-range between $0.02\,\mathrm{nm}^{-1}$ and $1.65\,\mathrm{nm}^{-1}$ corresponds to real-space distances d between 314 and 3 nm and, therefore, covers almost the entire nanometer range relevant for the characterization of the liposomes. The diagrams in Figure 2 show the radially integrated scattering signal of DPPC-DSPE/PEG (top panel) and Pad-PC-Pad (bottom panel) liposomes acquired in suitable glass capillaries.

For DPPC/DSPE-PEG, the intensity peak at around $1.1\,\mathrm{nm}^{-1}$, corresponding to 5.7 nm in real space, relates to the bilayer thickness.

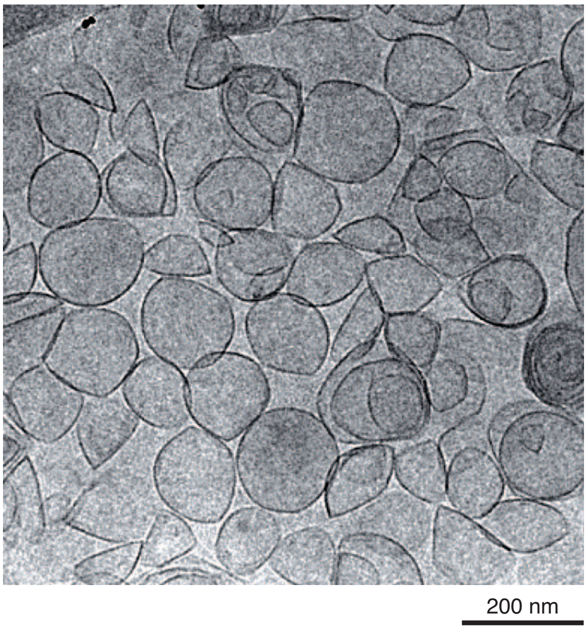

Figure 1: Cryo-TEM micrograph of Pad-PC-Pad showing faceted liposomes with a size between 100 and 200 nm. The liposomes exhibit a wide variety of shapes.

For Pad-PC-Pad, the peak related to bilayer thickness is located at the edge of the detectable q-range, which additionally incurs into increased noise, and thus cannot be unequivocally characterized.

Suitable models are often utilized in the interpretation of the scattering signal of the system investigated.[35] Herein, the scattering curves of DPPC/DSPE-PEG and Pad-PC-Pad were both fitted using a decoupling approach, which allowed to factorize the total form factor as product of a cross section term for long dimension and a cross section term for shorter dimension.[36] To fit the form factor related to the overall shape of DPPC/DSPE-PEG, a thin spherical shell model was used,[37] whereas the intensity peak related to the bilayer was fitted using a function for a bilayer with a Gaussian electron density profile.[38,39] The model utilized to fit the bilayer provided the bilayer thickness as the distance head-to-head d_{hh} between the two phospholipid heads and the standard deviation over the phoshpolipid heads.

To account for the polydispersity, the radii R and the d_{hh} were assumed to be normally distributed with means $R = 44.6\,\mathrm{nm}$ and $d_{\mathrm{hh}} = 2.4\,\mathrm{nm}$.

The DPPC/DSPE-PEG liposomes mean diameter of 89.2 nm is smaller than the mean value obtained from the DLS (101.3 nm). It has been reported that DLS provides values up to 20% higher compared to SAXS, as in SAXS solvent contrast variation does not allow to detect the hydrodynamic size of PEG bound to the liposomes surface.[15] As displayed in Figure 2 the drop in intensity of the scattering curve of DPPC/DSPE-PEG at the lowest q-values is attributed to inter-particle interference.[40] The addition of PEG was reported to prevent liposomes aggregation,[41] i.e. providing for a repulsive interaction between the particles. In the model utilized, PEG contribution was not included.

The distance head-to-head $d_{\mathrm{hh}} = 2.4\,\mathrm{nm}$ found for DPPC/DSPE-PEG is in line with the bilayer thickness value of 5.6 nm reported in Ref. 42, if one includes the calculated standard deviations $2\sigma = 3.0$ nm over the two phospholipid heads.

To fit the form factor related to the overall shape of Pad-PC-Pad a thin ellipsoidal shell model was used.[37] An eccentricity ϵ of 0.43 was found, in agreement with the value reported in Ref. 11. As for DPPC/DSPE-PEG, the intensity peak related to the phospholipid head-to-head distance d_{hh} was fitted using a function for a bilayer with a Gaussian electron density profile[38,39] and a normal distribution over d_{hh}. The results showed a mean value of $d_{\mathrm{hh}} = 3.3\,\mathrm{nm}$ and standard deviation of $2\sigma = 1.4$ nm over the two phospholipid heads.

At low q-values of Pad-PC-Pad scattering curve, the Guinier approximation[43] was used to determine the radius of gyration (R_{g}) and found $R_{\mathrm{g}} = 60.3\,\mathrm{nm}$ with standard deviation $\sigma_{R_{\mathrm{g}}} = 0.4\,\mathrm{nm}$ (see Table 2), in line with the averaged diameter value obtained from the DLS (131.6 nm).

3.3 SAXS measurements of Pad-PC-Pad under dynamic condition

The measurement in glass capillaries provided the fingerprint of Pad-PC-Pad liposome structure in static condition. In order to investigate the behavior of Pad-PC-Pad liposomes under an external perturbation, such as a shear stress gradient, 2D raster SAXS scans of Pad-PC-Pad liposomes under flow conditions, produced in a microfluidic device, were recorded.

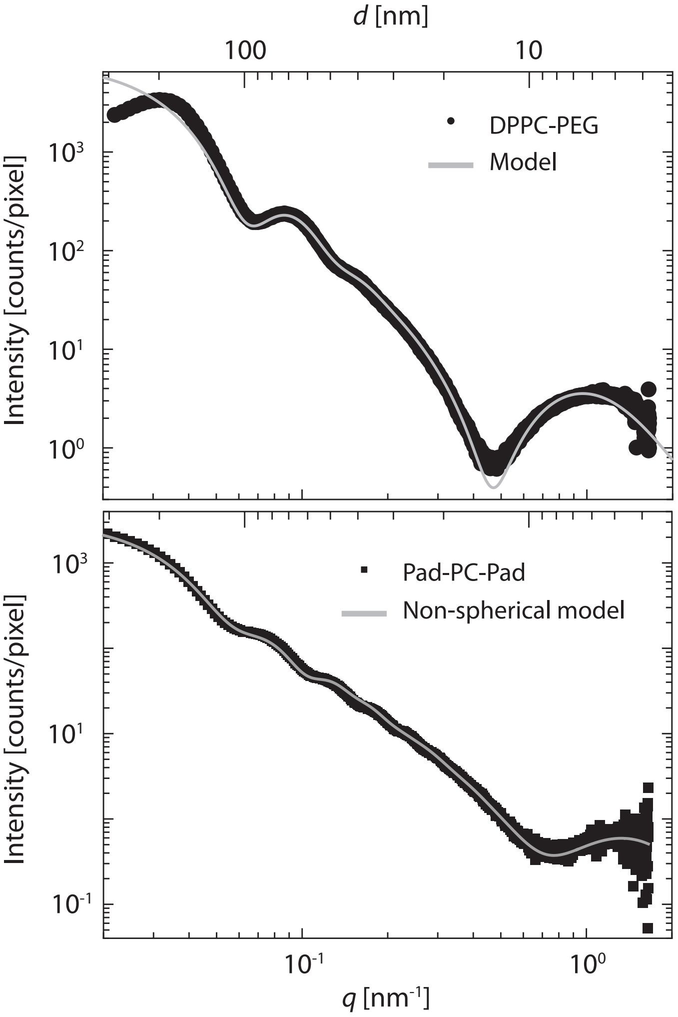

Figure 2: Integrated scattering signals of DPPC/DSPE-PEG (black dots, top diagram) and Pad-PC-Pad (black squares, bottom diagram) under static condition. The DPPC/DSPE-PEG signal was fitted with a thin spherical shell model and a bilayer Gauss electron density profile model (grey line, top panel) with head-to-head distance $d_{\mathrm{hh}} = 2.4$ nm and $2\sigma = 3.0$ nm over the two phospholipid heads. Pad-PC-Pad scattering signal was fitted with a thin ellipsoidal shell model and a bilayer Gauss electron density profile model (grey line, bottom panel) with eccentricity ϵ of 0.43, head-to-head distance of $d_{\mathrm{hh}} = 3.3$ nm and $2\sigma = 1.4$ nm over the two phospholipid heads.

Three flow velocities v were tested: $v = 0.002\,, 0.02\,,$ and $0.2\,\mu\text{L/s}$. The corresponding shear rates were determined using Eq. 1. From the lowest to the highest flow rate, the shear rates in the constriction ($h = 250\,\mu\text{m}$, $w = 125\,\mu\text{m}$) were $\gamma = 1.54$, 15.4, and 154.0 s^{-1}, whereas in the wide region ($h = 250\,\mu\text{m}$, $w = 1000\,\mu\text{m}$) they corresponded to $\gamma = 0.2$ s^{-1}, 2.0 s^{-1}, and 20.0 s^{-1}.

2D maps of the mean scattering intensity in the range $\Delta q = 0.096$ to $0.102\,\text{nm}^{-1}$ corresponding to a real space range $\Delta d = 65.4$ to $61.6\,\text{nm}$ between the overall size and the size of the phospholipid head-to-head distance are shown in Figure 3.

The non symmetric intensity distribution observed in the 2D maps is indicative of the complex behavior of the liposomes under varying flow conditions, and it is apparent that the flow rate, and as a consequence, the shear stress, affects the liposomes, giving rise to variations in scattering signal depending on the location within the device. At the lowest flow rate, slightly increased intensity on the inlet side was observed.

At the intermediate flow rate, the constriction significantly changed the flow field, which accelerated approaching the constriction, diverged in a plume-like shape immediately after the constriction, and finally decelerated far from the constriction. Surprisingly, within the constriction and for the whole length of it, the scattering signal decreased with respect to its entrance.

For the highest flow rate, a similar behavior was observed, with the difference that the intensity distribution at the inlet was “inverted”, i.e. stronger along the device walls. This stronger intensity at the device walls is indicative of a stagnation-zone, which was already incipient at the intermediate flow rate. Immediately after the constriction, a high-intensity “plume” akin to that at the intermediate flow rate was observed.

The local modifications of the averaged scattering intensity distribution observed in the 2D scanning SAXS maps of Figure 3 supported the selection of seven regions of the microfluidic device, as shown in the sketch of Figure 4. Three regions were selected before the constriction: one far (#1), one approaching (#2), and one very close (A); symmetrically, on

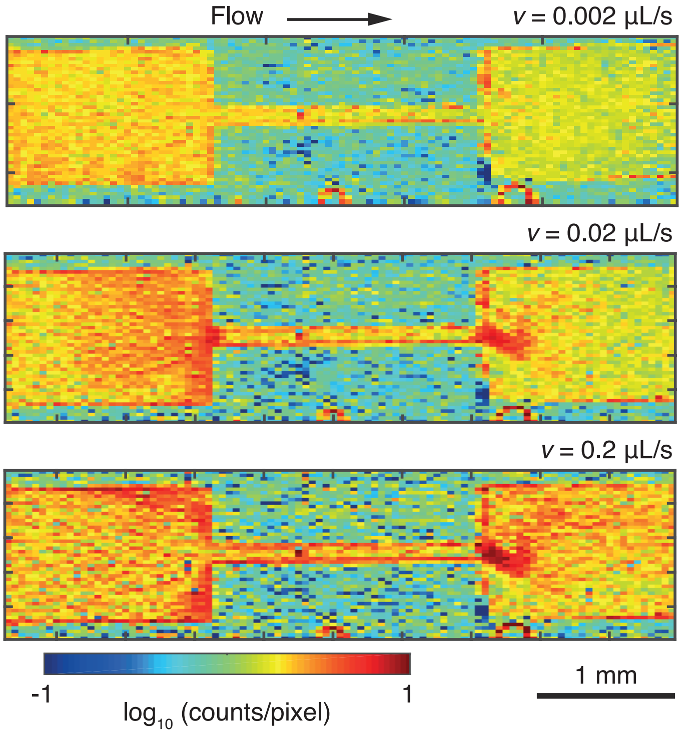

Figure 3: 2D maps of the average scattered intensity at three flow rates v in the q-range from 0.096 to 0.102 nm^{-1}. At the flow rate $v = 0.002\,\mu\text{L/s}$ the intensity appears rather homogeneous on both sides of the constriction, albeit slightly higher intensity is registered on the inlet side. At higher flow rates ($v = 0.02\,, 0.2\,\mu\text{L/s}$), a signal of increased intensity with a distinct plume-like shape is visible immediately at the constriction exit, whereas at the constriction entrance the signal reveals high intensity at intermediate flow rate and reduced intensity with stagnation zones at the device walls at the highest flow rate.

the outlet side, three areas were chosen one very close (B), one close (#4), and one far from the constriction (#5). Region #3 was selected in the constriction avoiding the edges of the device. For each region, the radially integrated scattering intensity I as a function of the scattering vector q at each flow rate v is shown.

On the inlet side (regions #1 and #2) no significant change at low and medium q can be observed as a function of v.

The oscillations of $I(q)$ observed at medium q overlap, indicating similar shape and size distributions of the liposomes. In contrast, the head-to-head distance d_{hh} slightly decreased with increasing flow, indicated by the shift of the position of the minimum to higher q (see Table 1).

In region A at the lowest flow rate, the scattering signal was comparable to the one observed in regions #1 and #2 at all q-ranges. At the intermediate flow rate and at intermediate q the oscillations smeared out. The smearing might indicate a change in the overall shape of the liposomes.

At $v = 0.2\,\mu\mathrm{L/s}$, the oscillation appeared again more pronounced, similar to the lowest flow rate, and the position of the minimum shifted to the right, in line with a decrease of d_{hh}.

Within the constriction (region #3), the scattering curves of the liposomes did not display any significant difference by varying the flow rate. However, an increase of the R_{g} values was observed at the three flow rates (see Table 2) with respect to the static condition and the regions before the constriction. No significant change in the d_{hh} values was detected. It should, however, be noted that the signal from the constriction is less reliable due to residual edge scattering from the device walls.

At the constriction exit (region B) the oscillations, still pronounced at the lowest flow rate, smeared out completely at the intermediate and high flow rate. In fact, the R_{g} values reported in Table 2 were comparable to the value found under static condition, but showed a decrease of about 13% at higher flow rate. Furthermore the minimum shifted to lower q

values, from 0.50 to 0.45 nm^{-1} indicating that in this region, the flow field caused an increase of d_{hh} of about 30% compared to the static condition (see Table 1).

The increase of the bilayer thickness of Pad-PC-Pad is in line with a mechanically induced loss of full interdigitation of phospholipid amide chains, which is usually observed at the liquid-crystalline phase (above the transition temperature) and, in presence of cholesterol, at the gel phase (below the transition temperature).[44]

In region #4, the scattering signal gradually reduced. For the intermediate and high flow rates the oscillations were smeared, as in region B, whereas for the lowest flow rate the oscillations were well visible, as in region #2. The position of the minimum did not vary significantly among the three flow rates, indicating no significant modification on the bilayer thickness.

In region #5 and at the three flow rates, the oscillations appeared similar as in region #1. In contrast, the position of the minimum, at the highest flow rate, shifted slightly to the right, from 0.55 to 0.6 nm^{-1}, compared to the intermediate and lowest flow rate.

Due to the impact of the local flow field, alteration of the liposomes morphology in regions A and B is detected (see Figure 4), both at the high and low q, compared to the other regions where modifications, by varying the flow rate, were observed either at low q (e.g., region #5) or at high q (e.g., region #1,#2).

To highlight the changes of regions A (before constriction) and B (after constriction) at the three flow rates (see Figure 4), the scattering curves in these two regions were displayed as normalized difference of their scattering intensities (see graph in Figure 5).

Herein, three Δq ranges were selected including the mean overall size of the liposomes ($\Delta q_1 = 0.04 - 0.05$ nm^{-1}), the size around the bilayer thickness ($\Delta q_3 = 0.83 - 1.12$ nm^{-1}) and a range in between ($\Delta q_2 = 0.16 - 0.17$ nm^{-1}). 2D maps of the integrated scattered intensity in each selected Δq at each flow rate are displayed.

The 2D map at the lowest flow rate and in the range Δq_3 (see Figure 5, bottom right), showed vertical stripes before and after the constriction, clear sign of the presence of artifacts

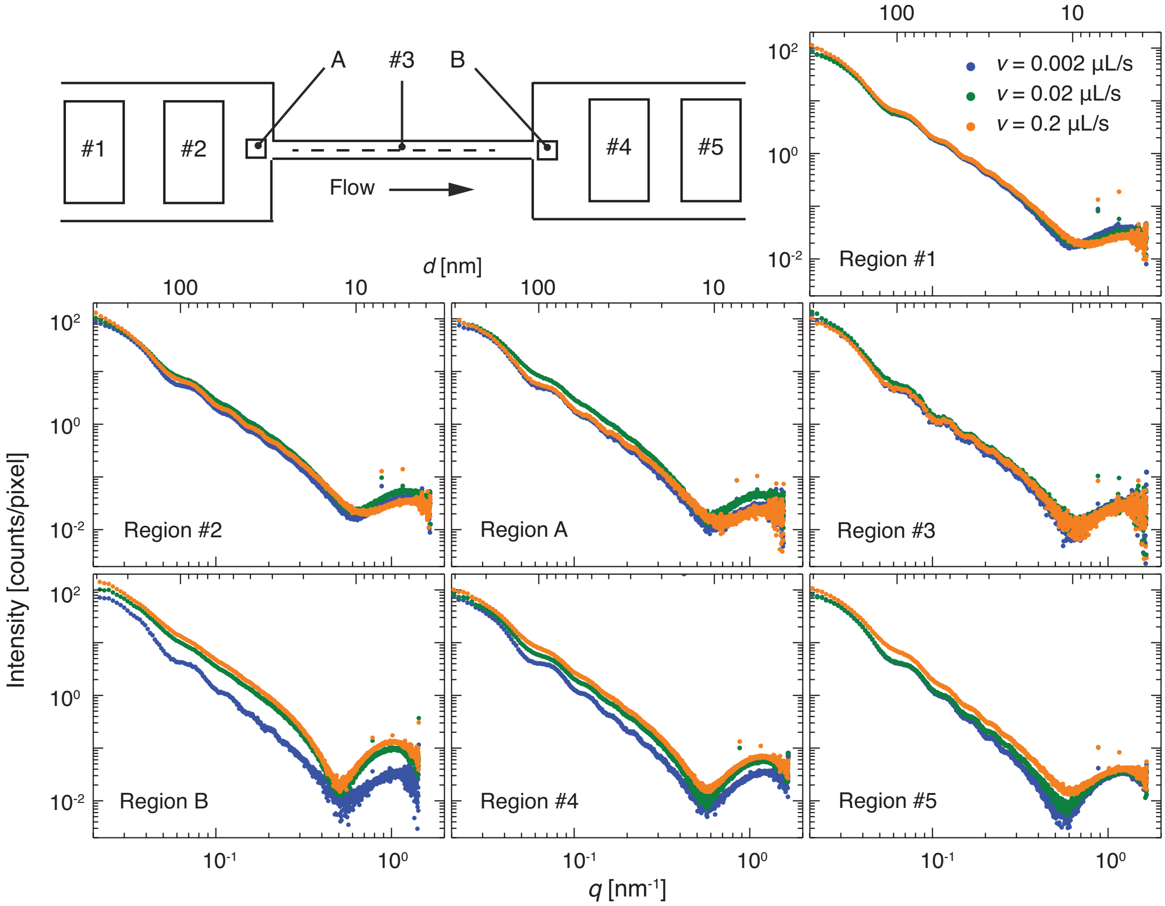

Figure 4: Top left, sketch of the microfluidic device showing the seven regions selected. For each region, the radially integrated scattering signal is plotted for the three flow rates ($v = 0.002\,\mu\mathrm{L/s}$ in blue, $v = 0.02\,\mu\mathrm{L/s}$ in green, and $v = 0.2\,\mu\mathrm{L/s}$ in orange). Differences at high q-values are apparent in the regions before and after constriction, indicating changes in bilayer thickness, and are pronounced at higher flow rates.

within the microfluidic device. At the three Δq ranges selected, the 2D maps (see Figure 5) a trend comparable to the one shown in Figure 3 was observed.

Table 1: Pad-PC-Pad liposomes head-to-head distance d_{hh} under static condition (glass capillary) and under dynamic condition in the seven regions (see sketch of Figure 4) of the microfluidic device. The data represent the mean values of the normal distribution, including the associated errors derived from the standard deviation.

	d_{hh} [nm]							
		microfluidic device positions						
flow rate [μL/s]	**glass capillary**	#1	#2	**A**	#3	**B**	#4	#5
0	3.3±0.8							
0.002		3.4±0.7	3.1±0.4	3.4±0.5	3.9±0.7	4.0±0.6	3.9±0.4	3.8±0.3
0.02		3.4±0.7	2.9±0.2	2.9±0.2	3.5±0.6	4.3±0.5	3.6±0.3	3.9±0.4
0.20		3.4±0.9	3.4±0.7	3.2±0.6	3.8±0.8	4.4±0.4	4.0±0.6	4.0±0.7

The response of Pad-PC-Pad liposomes to the flow field was compared to the one of DPPC/DSPE-PEG as reported in Figure 6. Herein, the scattering signals of Pad-PC-Pad and DPPC/DSPE-PEG were radially integrated in the two areas – blue and red boxes– indicated in the device sketches of Figure 6.

DPPC/DSPE-PEG measurements in dynamic condition were carried out in a microfluidic device having a constriction width two times wider ($w_{constriction} = 250\,\mu\mathrm{m}$) than the one utilized for Pad-Pad-Pad. For a fair comparison, and considering Eq. 1, the same shear condition at the constriction location was obtained by setting twice the flow rate for DPPC/DSPE-PEG liposomes than the flow rate to which Pad-PC-Pad liposomes were subjected.

Whereas significant differences in scattering curves, including the shift of the bilayer peak,

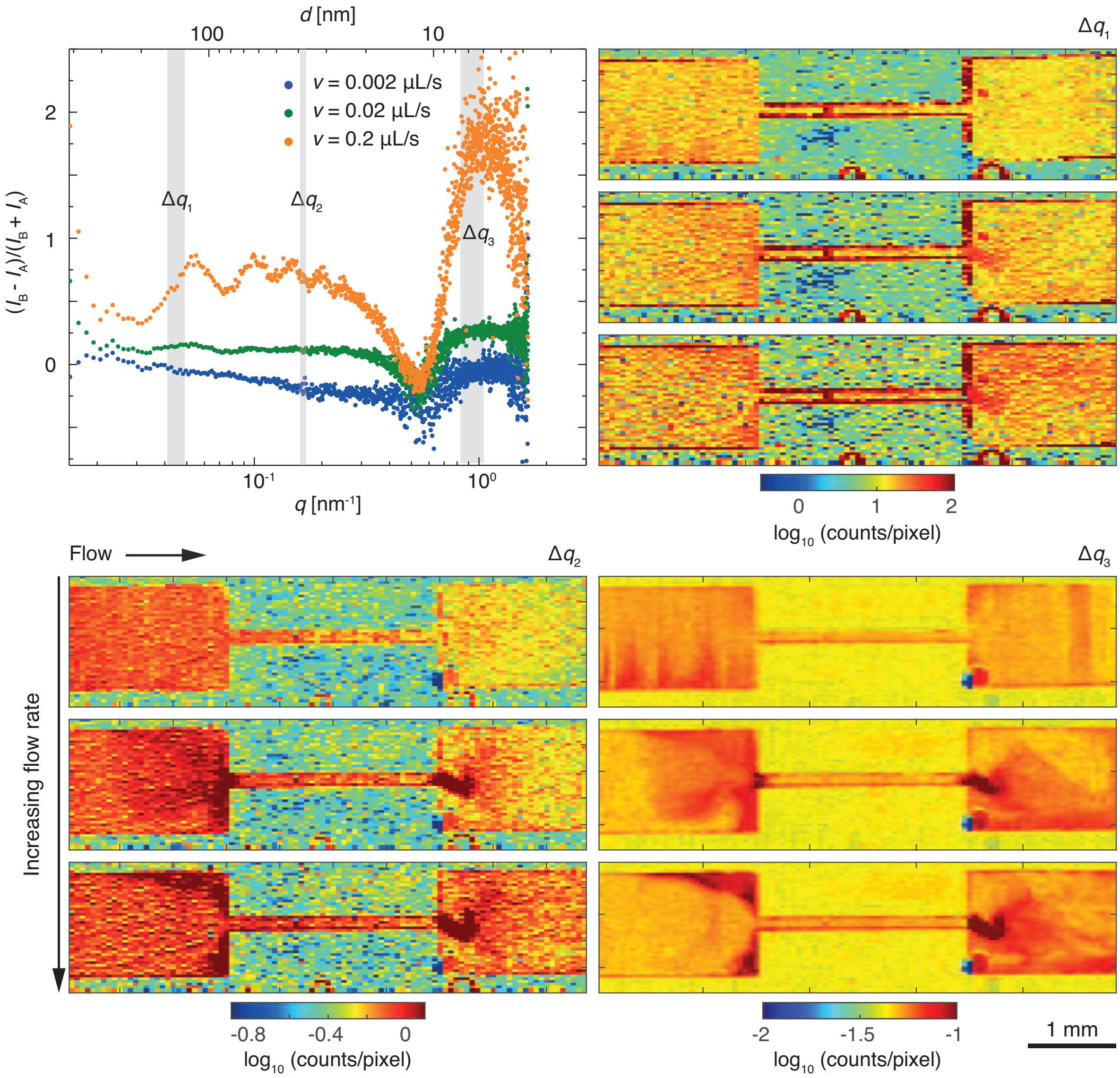

Figure 5: The graph shows the normalized difference $(I_\mathrm{B} - I_\mathrm{A})/(I_\mathrm{B} + I_\mathrm{A})$ of the I *vs.* q curves in regions A and B (*cf.* Figure 4) for the three flow rates. Especially for the highest flow rate, marked differences are seen in scattering signal, prominently at high q, indicating changes in head-to-head distance. 2D maps of average scattered intensity are shown for three selected q-ranges ($\Delta q_1 = 0.04$ to $0.05\,\mathrm{nm}^{-1}$, $\Delta q_2 = 0.16$ to $0.17\,\mathrm{nm}^{-1}$, and $\Delta q_3 = 0.83$ to $1.12\,\mathrm{nm}^{-1}$). As in Figure 3, the establishment of a flow field with increasing flow rate can be observed.

Table 2: Radius of gyration R_g of Pad-PC-Pad liposomes under static condition (glass capillary) and under dynamic condition as a function the microfluidic device positions displayed in the sketch of Figure 4. The data represent the mean values of the normal distribution, including the associated errors derived from the standard deviation.

	R_g [nm]							
		microfluidic device positions						
flow rate [μL/s]	**glass capillary**	#1	#2	**A**	#3	**B**	#4	#5
0	60.3±0.4							
0.002		59.5±0.2	59.1±0.1	60.3±0.4	63.0±0.5	59.3±0.9	61.1±0.2	61.6±0.2
0.02		60.2±0.2	58.0±0.4	55.1±0.5	64.3±0.6	52.4±0.8	59.1±0.3	61.3±0.1
0.20		61.6±0.4	61.0±0.5	61.4±0.6	64.0±0.8	52.3±0.9	58.0±0.3	60.0±0.4

from the SAXS signals Pad-PC-Pad liposomes before and after the constriction are present, no changes of DPPC/DSPE-PEG liposomes could be probed, as their scattering signals under static condition and under dynamic condition (before and after the constriction) overlapped. The comparison with DPPC/DSPE-PEG liposomes supports our hypothesis that Pad-PC-Pad liposomes are mechano-responsive, already before the constriction and at the shear rates here investigated.

4 Conclusions

We have shown that the combination of microfluidics and SAXS is valuable technique for detecting *in situ* and real time the structure modification, at different nanometer scales, of Pad-PC-Pad liposomes which present a broad variety of shape. Modification on the Pad-PC-Pad liposomes, both at high and low q-range, were detected already before the microchannel

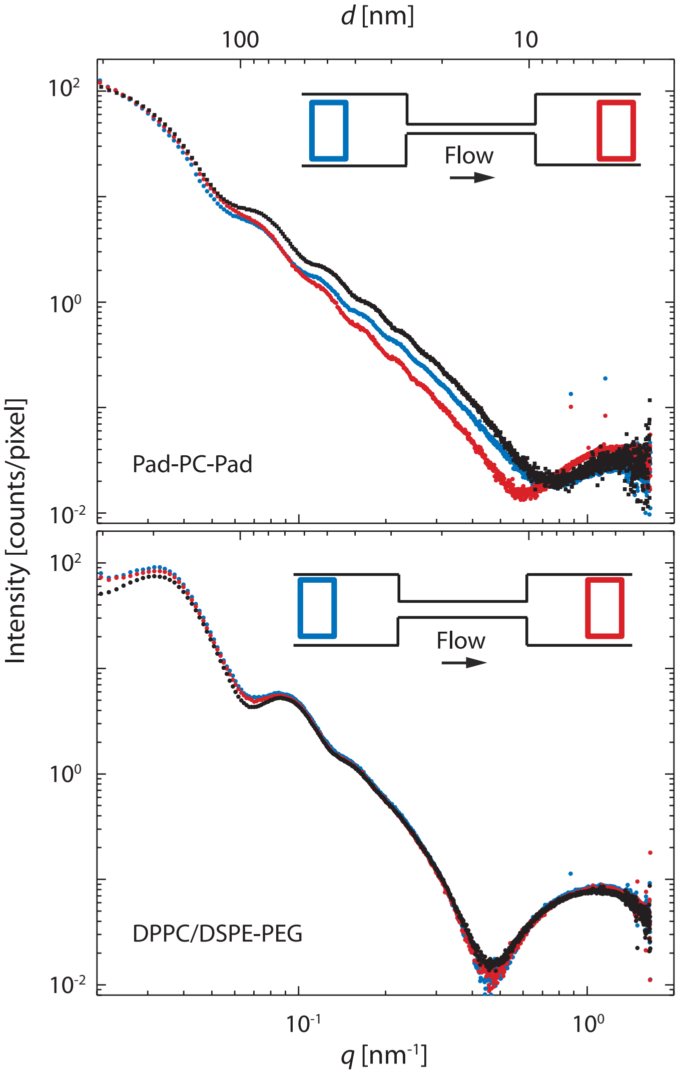

Figure 6: Comparison of the scattering intensity curves for the same maximum shear acting on Pad-PC-Pad (top) and DPPC/DSPE-PEG (bottom) before (blue-colored dots) and after (red-colored dots) constriction. A significant shift of the bilayer peak of Pad-PC-Pad liposomes is observed after the constriction with respect to the scattering signal before the constriction and under static condition (dark-colored dots).

constriction and at the shear rates here investigated, which are much lower than the ones found in healthy and stenotic blood vessels.[30]

We have observed changes in the phospholipid head-to-head distance (high q) of Pad-PC-Pad liposomes, which decreased while approaching the constriction (Region A) and increased immediately after the constriction (Region B). The increasing of the head-to-head distance up to 30% compared to the static condition, suggests that the shear gradient modifies the membrane defects, which characterize Pad-PC-Pad liposomes membrane, in agreement with a mechanically induced loss of the interdigitation between the phospholipid chains. Contrary to DPPC/DSPE-PEG liposomes, Pad-PC-Pad liposomes showed remarkable changes in X-ray scattering already 1 mm before and after the constriction.

Acknowledgement

This work was partially funded by the Swiss National Science Foundation (SNSF) project 126090 via the National Research Program (NRP) 62 'Smart Materials'. The authors thank Sofiya Matviykiv for supporting during liposomes preparation, Dennis Mueller for Pad-PC-Pad lipid synthesis, and Viviane Lutz Bueno for valuable discussion on microfluidic devices and support on masters fabrication. The authors thank Marianne Liebi for supporting during the experiment carried out at the cSAXS beamline (proposal 20151414). The valuable service of Takashi Ishikawa (Paul Scherrer Institute, Switzerland) in collecting the micrograph (Figure 1) at PSI EM Facility is gratefully acknowledged.

Additional information

Competing interests: The authors declare no competing interests.

References

(1) Lanza, G.; Winter, P.; Cyrus, T.; Caruthers, S.; Marsh, J.; Hughes, M.; Wickline, S. Nanomedicine opportunities in cardiology. *Annals of the New York Academy of Sciences* **2006**, 451–465.

(2) Yin, W.; Shanmugavelayudam, S. K.; Rubenstein, D. A. 3D numerical simulation of coronary blood flow and its effect on endothelial cell activation. *Engineering in Medicine and Biology Society, 2009. Annual International Conference of the IEEE* **2009**, 4003–4006.

(3) Holme, M. N.; Fedotenko, I. A.; Abegg, D.; Althaus, J.; Babel, L.; Favarger, F.; Reiter, R.; Tanasescu, R.; Zaffalon, P.-L.; Ziegler, A.; Müller, B.; Saxer, T.; Zumbuehl, A. Shear-stress sensitive lenticular vesicles for targeted drug delivery. *Nature Nanotechnology* **2012**, *7*, 536–543.

(4) Korin, N.; Kanapathipillai, M.; Matthews, B. D.; Crescente, M.; Brill, A.; Mammoto, T.; Ghosh, K.; Jurek, S.; Bencherif, S. A.; Bhatta, D.; Coskun, A. U.; Feldman, C. L.; Wagner, D. D.; Ingber, D. E. Shear-Activated Nanotherapeutics for Drug Targeting to Obstructed Blood Vessels. *Science* **2012**, *337*, 738–742.

(5) Tinkle, S.; McNeil, S. E.; Mühlebach, S.; Bawa, R.; Borchard, G.; Barenholz, Y. C.; Tamarkin, L.; Desai, N. Nanomedicines: addressing the scientific and regulatory gap. *Annals of the New York Academy of Sciences* **2014**, *1313*, 35–56.

(6) Torchilin, V. P. Recent advances with liposomes as pharmaceutical carriers. *Nature reviews Drug discovery* **2005**, *4*, 145–160.

(7) Fedotenko, I. A.; Zaffalon, P.-L.; Favarger, F.; Zumbuehl, A. The synthesis of 1,3-diamidophospholipids. *Tetrahedron Letters* **2010**, *51*, 5382–5384.

(8) Dubois, M.; Zemb, T. Swelling limits for bilayer microstructures: the implosion of lamellar structure versus disordered lamellae. *Current Opinion in Colloid & Interface Science* **2000**, *5*, 27–37.

(9) Weinberger, A.; Tanasescu, R.; Stefaniu, C.; Fedotenko, l. A.; Favarger, F.; Ishikawa, T.; Brezesinski, G.; Marques, C. M.; Zumbuehl, A. Bilayer properties of 1,3-Diamidophospholipids. *Langmuir* **2015**, *31*, 1879–1884.

(10) Bugna, S.; Buscema, M.; Matviykiv, S.; Urbanics, R.; Weinberger, A.; Meszaros, T.; Szebeni, J.; Zumbuehl, A.; Saxer, T.; Müller, B. Surprising lack of liposome-induced complement activation by artificial 1,3-diamidophospholipids in vitro. *Nanomedicine: Nanotechnology, Biology and Medicine* **2016**, *12*, 845–849.

(11) Buscema, M. et al. Immunological response to nitroglycerin-loaded shear-responsive liposomes in vitro and in vivo. *Journal of Controlled Release* **2017**, *264*, 14–23.

(12) Hope, M.; Bally, M.; Webb, G.; Cullis, P. Production of large unilamellar vesicles by a rapid extrusion procedure. Characterization of size distribution, trapped volume and ability to maintain a membrane potential. *Biochimica et Biophysica Acta (BBA) - Biomembranes* **1985**, *812*, 55–65.

(13) Engelhaaf, S. U.; Wehrli, B.; Müller, M.; Adrian, M.; Schurtenberger, P. Determination of the size distribution of lecithin liposomes: a comparative study using freeze fracture, cryoelectron microscopy and dynamic light scattering. *Journal of Microscopy* **1996**, *184*, 214–228.

(14) Helvig, S.; Azmi, I. D.; Moghimi, S. M.; Yaghmur, A. Recent advances in cryo-TEM imaging of soft lipid nanoparticles. *AIMS Biophysics* **2015**, *2*, 116–130.

(15) Garcia-Diez, R.; Gollwitzer, C.; Krumrey, M.; Varga, Z. Size determination of a liposomal drug by small-angle X-ray scattering using continuous contrast variation. *Langmuir* **2016**, *32*, 772–778.

(16) Foglia, F.; Drake, A.; Terry, A.; Rogers, S.; Lawrence, M.; Barlow, D. Small-angle neutron scattering studies of the effects of amphotericin B on phospholipid and phospholipid-sterol membrane structure. *Biochimica et Biophysica Acta (BBA) - Biomembranes* **2011**, *1808*, 1574–1580.

(17) Köster, S.; Pfohl, T. X-ray studies of biological matter in microfluidic environments. *Modern Physics Letters B* **2012**, *26*, 1230018.

(18) Bunk, O.; Bech, M.; Jensen, T. H.; Feidenhans'l, R.; Binderup, T.; Menzel, A.; Pfeiffer, F. Multimodal x-ray scatter imaging. *New Journal of Physics* **2009**, *11*, 123016.

(19) Müller, B.; Deyhle, H.; Bradley, D. A.; Farquharson, M.; Schulz, G.; Müller-Gerbl, M.; Bunk, O. Nanomethods: Scanning X-ray scattering: Evaluating the nanostructure of human tissues. *European Journal of Nanomedicine* **2010**, *3*, 30–33.

(20) Gaiser, S.; Deyhle, H.; Bunk, O.; White, S. N.; Müller, B. Understanding nano-anatomy of healthy and carious human teeth: a prerequisite for nanodentistry. *Biointerphases* **2012**, *7*, 4.

(21) Georgiadis, M.; Guizar-Sicairos, M.; Zwahlen, A.; Trüssel, A. J.; Bunk, O.; Müller, R.; Schneider, P. 3D scanning SAXS: A novel method for the assessment of bone ultrastructure orientation. *Bone* **2015**, *71*, 42 – 52.

(22) Lutz-Bueno, V.; Zhao, J.; Mezzenga, R.; Pfohl, T.; Fischer, P.; Liebi, M. Scanning-SAXS of microfluidic flows: nanostructural mapping of soft matter. *Lab on a Chip* **2016**, *16*, 4028–4035.

(23) Pham, N.; Radajewski, D.; Round, A.; Brennich, M.; Pernot, P.; Biscans, B.; Bonneté, F.; Teychene, S. Coupling high throughput microfluidics and small-angle X-ray scattering to study protein crystallization from solution. *Analytical Chemistry* **2017**, *89*, 2282–2287.

(24) Balbino, T. A.; Azzoni, A. R.; de la Torre, L. G. Microfluidic devices for continuous production of pDNA/cationic liposome complexes for gene delivery and vaccine therapy. *Colloids and Surfaces B: Biointerfaces* **2013**, *111*, 203–210.

(25) Pollack, L.; Tate, M. W.; Darnton, N. C.; Knight, J. B.; Gruner, S. M.; Eaton, W. A.; Austin, R. H. Compactness of the denatured state of a fast-folding protein measured by submillisecond small-angle x-ray scattering. *Proceedings of the National Academy of Sciences* **1999**, *96*, 10115–10117.

(26) Toma, A. C.; Dootz, R.; Pfohl, T. Analysis of complex fluids using microfluidics: the particular case of DNA/polycations assemblies. *Journal of Physics D: Applied Physics* **2013**, *46*, 114001.

(27) Poulos, A. S.; Nania, M.; Lapham, P.; Miller, R. M.; Smith, A. J.; Tantawy, H.; Caragay, J.; Gummel, J.; Ces, O.; Robles, E. S. J.; Cabral, J. T. Microfluidic SAXS study of lamellar and multilamellar vesicle phases of linear sodium alkylbenzenesulfonate surfactant with intrinsic isomeric distribution. *Langmuir* **2016**, *32*, 5852–5861.

(28) With, S.; Trebbin, M.; Bartz, C. B. A.; Neuber, C.; Dulle, M.; Yu, S.; Roth, S. V.; Schmidt, H.-W.; Förster, S. Fast diffusion-limited lyotropic phase transitions studied in situ using continuous flow microfluidics/microfocus-SAXS. *Langmuir* **2014**, *30*, 12494–12502.

(29) Dootz, R.; Evans, H.; Köster, S.; Pfohl, T. Rapid prototyping of X-ray microdiffraction compatible continuous microflow foils. *Small* **2007**, *3*, 96–100.

(30) Molloy, C. P.; Yao, Y.; Kammoun, H.; Bonnard, T.; Hoefer, T.; Alt, K.; Trovar-Lopez, F.; Rosengarten, G.; Ramsland, P. A.; Meer, A. D.; Berg, A.; Murphy, A. J.; Hagemeyer, C. E.; Peter, K.; Westein, E. Shear-sensitive nanocapsule drug release for site- specific inhibition of occlusive thrombus formation. *Journal of Thrombosis and Haemostasis* **2016**, *15*, 972–982.

(31) Walde, P. Preparation of vesicles (liposomes). *Encycl. Nanosci. Nanotechnol.* **2004**, *9*, 43–79.

(32) Olson, F.; Hunt, C.; Szoka, F.; Vail, W.; Papahadjopoulos, D. Preparation of liposomes of defined size distribution by extrusion through polycarbonate membranes. *Biochimica et Biophysica Acta (BBA) - Biomembranes* **1979**, *557*, 9 – 23.

(33) Stalder, E.; Zumbuehl, A. Phosphate Test 2.0. *CHIMIA International Journal for Chemistry* **2013**, *67*, 819–821.

(34) Kraft, P.; Bergamaschi, A.; Broennimann, C.; Dinapoli, R.; Eikenberry, E. F.; Henrich, B.; Johnson, I.; Mozzanica, A.; Schlepütz, C. M.; Willmott, P. R.; Schmitt, B. Performance of single-photon-counting PILATUS detector modules. *J. Synchrotron Radiat.* **2009**, *16*, 368–375.

(35) Vasilca, V.; Sadeghpour, A.; Rawson, S.; Hawke, L.; Baldwin, S.; Wilkinson, T.; Bannister, D.; Postis, V.; Rappolt, M.; Muench, S.; Jeukena, L. Spherical-supported membranes as novel platforms for the screening of membrane protein targets. *Analytical Biochemistry* **2018**, *549*, 58–65.

(36) Porod, G. Die Abhangigkeitder Rontgen-Kleinwinkelstreuung von Form und Grösse der kolloiden Teilchen in verdünnten Systemen, IV. *Acta Physica Austriaca* **1948**, *2*, 255–292.

(37) Breßler, I.; Kohlbrecher, J.; Thünemann, A. F. SASfit: a tool for small-angle scattering data analysis using a library of analytical expressions. *Journal of Applied Crystallography* **2015**, *48*, 1587–1598.

(38) Pabst, G.; Koschuch, R.; Pozo-Navas, B.; Rappolt, M.; Lohner, K.; Laggner, P. Structural analysis of weakly ordered membrane stacks. *Journal of Applied Crystallography* **2003**, *36*, 1378–1388.

(39) Pabst, G.; Rappolt, M.; Amenitsch, H.; Laggner, P. Structural information from multilamellar liposomes at full hydration: full q-range fitting with high quality x-ray data. *Physical Review E* **2000**, *62*, 4000.

(40) Glatter, O.; Kratky, O. *Small angle X-ray scattering*; Academic press, 1982.

(41) Bozzuto, G.; Molinari, A. Liposomes as nanomedical devices. *International Journal of Nanomedicine* **2015**, *10*, 975–999.

(42) Wang, M.; Zander, T.; Liu, X.; Liu, C.; Raj, A.; Wieland, D. F.; Garamus, V. M.; Willumeit-Römer, R.; Claesson, P. M.; Dedinaite, A. The effect of temperature on supported dipalmitoylphosphatidylcholine (DPPC) bilayers: Structure and lubrication performance. *Journal of Colloid and Interface Science* **2015**, *445*, 84–92.

(43) Guinier, A. La diffraction des rayons X aux très petits angles: application à l'étude de phénomènes ultramicroscopiques. *Annales de Physique* **1939**, *11*, 161–237.

(44) Tanasescu, R.; Lanz, M. A.; Mueller, D.; Tassler, S.; Ishikawa, T.; Reiter, R.; Brezesinski, G.; Zumbuehl, A. Vesicle origami and the influence of cholesterol on lipid packing. *Langmuir* **2016**, *32*, 4896–4903.

2.4 Immunological response to nitroglycerin-loaded shear-responsive liposomes *in vitro* and *in vivo*

Published in Journal of Controlled Release

Journal of Controlled Release 264 (2017) 14–23

Contents lists available at ScienceDirect

Journal of Controlled Release

journal homepage: www.elsevier.com/locate/jconrel

Immunological response to nitroglycerin-loaded shear-responsive liposomes *in vitro* and *in vivo*

Marzia Buscema[a], Sofiya Matviykiv[a], Tamás Mészáros[b,c], Gabriela Gerganova[a],
Andreas Weinberger[d], Ute Mettal[d], Dennis Mueller[d], Frederik Neuhaus[d], Etienne Stalder[d],
Takashi Ishikawa[e], Rudolf Urbanics[c], Till Saxer[f], Thomas Pfohl[a], János Szebeni[b,c,g],
Andreas Zumbuehl[d], Bert Müller[a,*]

[a] *Biomaterials Science Center, Department of Biomedical Engineering, University of Basel, Allschwil, Switzerland*
[b] *Nanomedicine Research and Education Center, Institute of Pathophysiology, Semmelweis University Budapest, Hungary*
[c] *SeroScience Ltd., Budapest, Hungary*
[d] *Department of Chemistry, University of Fribourg, Fribourg, Switzerland*
[e] *Paul Scherrer Institute (PSI), Villigen, Switzerland*
[f] *Cardiology Division, University Hospital of Geneva, Geneva, Switzerland*
[g] *Department of Nanobiotechnology and Regenerative Medicine, Faculty of Health, Miskolc University, Miskolc, Hungary*

ARTICLE INFO

Keywords:
Nanomedicine
Drug delivery
Complement activation
Pathway
Metastable liposome
Porcine model
Biophysics
Shear-responsive nano-container

ABSTRACT

Liposomes formulated from the 1,3-diamidophospholipid Pad-PC-Pad are shear-responsive and thus promising nano-containers to specifically release a vasodilator at stenotic arteries. The recommended preclinical safety tests for therapeutic liposomes of nanometer size include the *in vitro* assessment of complement activation and the evaluation of the associated risk of complement activation-related pseudo-allergy (CARPA) *in vivo*. For this reason, we measured complement activation by Pad-PC-Pad formulations in human and porcine sera, along with the nanopharmaceutical-mediated cardiopulmonary responses in pigs. The evaluated formulations comprised of Pad-PC-Pad liposomes, with and without polyethylene glycol on the surface of the liposomes, and nitroglycerin as a model vasodilator. The nitroglycerin incorporation efficiency ranged from 25% to 50%. In human sera, liposome formulations with 20 mg/mL phospholipid gave rise to complement activation, mainly *via* the alternative pathway, as reflected by the rises in SC5b-9 and Bb protein complex concentrations. Formulations having a factor of ten lower phospholipid content did not result in measurable complement activation. The weak complement activation induced by Pad-PC-Pad liposomal formulations was confirmed by the results obtained by performing an *in vivo* study in a porcine model, where hemodynamic parameters were monitored continuously. Our study suggests that, compared to FDA-approved liposomal drugs, Pad-PC-Pad exhibits less or similar risks of CARPA.

1. Introduction

Over the last two decades, liposomal formulations, developed as containers for the targeted and controlled release of drugs, have been studied in detail [1–3]. Some of these drugs have been approved by the Food and Drug Administration (FDA) [4]. Controlled drug release over time in a stenotic artery due to specific liposome sensitivity on higher local wall shear stress, can potentially increase the therapeutic index of an encapsulated vasodilating drug [5]. Simultaneously, when the active drug, protected by encapsulation, is circulating in the human body, side effects observed after systemic administration are reduced as often described for oncological therapeutics [6]. For cardiovascular treatment agents, hypotension is a characteristic side effect which may be observed when vasodilating drugs are systemically administered in case of an acute ischemic event, in order to increase local perfusion pressure in a suffering organ such as the heart, the brain, or the kidneys [7].

The pathology of atherosclerosis is characterized by the narrowing and hardening of blood vessels as a result of atherosclerotic plaque formation [8]. This significant narrowing of the arterial blood vessels alters blood flow and causes changes in the average wall shear stress in comparison to physiological conditions [9]. It has been reported that an 80%-constricted artery gives rise to a wall shear stress increase of one order of magnitude [10]. Such an increase of shear stress has been

---

* Corresponding author at: Biomaterials Science Center, Department of Biomedical Engineering, University of Basel, Gewerbestrasse 14, 4123 Allschwil, Switzerland.
E-mail address: bert.mueller@unibas.ch (B. Müller).

http://dx.doi.org/10.1016/j.jconrel.2017.08.010
Received 8 June 2017; Received in revised form 6 August 2017; Accepted 8 August 2017

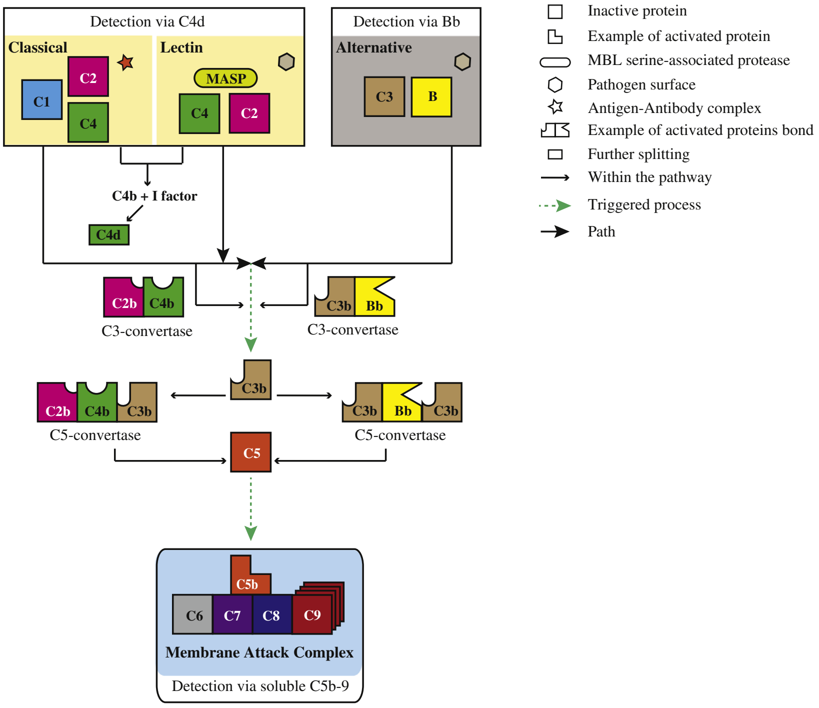

Fig. 1. Main steps of the complement activation cascade. The identification of the SC5b-9 complex (light blue-colored box) through the three pathways provides an insight into understanding the interaction between Pad-PC-Pad liposomes and the immune system. The classical pathway (yellow-colored box) is mediated by an antigen-antibody complex, whereas the lectin pathway (also a yellow-colored box) and the alternative pathway (gray-colored box) are initiated at the pathogen surfaces. (For interpretation of the references to colour in this figure legend, the reader is referred to the web version of this article.)

proposed as a trigger signal for targeted vasodilator delivery [5]. Nanometer-sized, lentil-shaped Pad-PC-Pad liposomes have shown the unique property of being able to release their cargo under mechanical stimuli [11]. Targeted drug delivery by these liposomes can be used to mitigate systemic side effects caused by the intravenous administration of vasodilators during cardiovascular emergencies. Based on these liposomes, we focus on the development of an infusion-based medication to be given to the patient at any location, for example at the site of a myocardial infarction. The medication should be active until the patient reaches the operation theater. As continuous infusion, it should not stay in the blood stream for prolonged residence time.

Nonetheless, liposomal drugs are often recognized as foreign particles and hence are attacked by the immune system leading to a biochemical cascade termed *complement activation*[12]. If there is any complement activation, it is helpful to understand the mechanism behind the interaction of liposomes with the immune system. In the serum, there are > 30 complement proteins which usually contribute as defenders. Some of them can split into fragments when stimulated. The complement protein cleavage (*cf.* Fig. 1) can be activated along three pathways, termed classical, lectin, and alternative [13]. The main differences among the three pathways are displayed in Fig. 1. In the classical pathway, which is mainly mediated by an antigen-antibody complex (star), the C1 complex (light blue-colored) initiates the activation of the C3 (light brown-colored) and C5 (orange-colored) proteins by triggering the proteins C2 (pink-colored) and C4 (green-colored), thereby giving rise to C3- and C5-convertases. In order to cleave the C5 protein, the immune system can also follow another route, namely the lectin pathway, which is mediated by the interaction between mannose-binding lectin (MBL) and the surface of a pathogen, leading to the cleavage of the C3 and C5 proteins. Cleaved C5 links the proteins C6 (gray-colored), C7 (purple-colored), C8 (dark blue-colored), and the polymeric C9 (red-colored), thereby producing the complex C5b-9, known as the *Membrane Attack Complex* (MAC) or the *Terminal Complement Complex* (TCC). The MAC induces the formation of a defect in the cell membrane that damages or destroys the suspected microorganism, and it can also form *via* the alternative pathway, due to interaction with the C3 protein, the B-factor fragment Bb (yellow), and the surface of a pathogen (hexagon). These interactions lead to the C5 protein and the MAC formation [14].

Released complement protein fragments such as C3a and C5a stimulate mast cells, granulocytes and macrophages, which can significantly contribute to cardiovascular distress [15–17]. The particle morphology can play a decisive role in preventing phagocytosis processes [18,19] like those ones mediated by pulmonary intravascular macrophages as it has been recently discussed [20].

The activation of the immune system may lead to an adverse immune phenomenon known as *complement activation-related pseudo-allergy* (CARPA) [21]. CARPA is used to describe acute hypersensitivity reactions (HSRs) to nanomedicines occurring in up to 45% of individuals [22]. In some individuals, these HSRs can be severe or even fatal [23]. It has been proposed that pigs can provide a sensitive, quantitative, and biologically relevant animal model of severe human CARPA [24–28]. The main manifestation of CARPA is cardiopulmonary distress, caused by pulmonary hypertension, which is critical for patients suffering from cardiac pathologies [23]. It leads to changes in pulmonary arterial pressure (PAP) and systemic arterial pressure (SAP) [26,29,30]. Due to this potential reactivity, the European Medicines Agency recommends *in vitro* and *in vivo* assessments of CARPA as a preclinical immune toxicity test in the development of liposomal drugs [31]. Detection and prevention of CARPA at an early stage of nanomedicine research is one of the strategies to successfully develop nanopharmaceutics. Liposomal drugs that cause CARPA have been reported previously [21,32]. Phospholipid bilayers can activate the complement system, and, among other factors, size, shape, lipid composition, and presence of surface charges are all sources for complement activation by liposomes *in vitro*[15,23,24]. Therefore, one step on the road to testing shear-responsive Pad-PC-Pad liposomes clinically is the evaluation and minimization of their risk for HSRs.

In the present communication, we hypothesize that Pad-PC-Pad liposomes, containing PEGylated lipids and nitroglycerin, hardly trigger CARPA.

Table 1
Liposomal suspensions tested *in vitro* and *in vivo*.

Label		Lipid composition (molar %)		Load
In vitro	*In vivo*	Pad-PC-Pad	DSPE-PEG2000	
L1, L1a[a]	L1′	95	5	Nitroglycerin
L2, L2a[a]	L2′	95	5	Bare
L3, L3a[a]	L3′	100	–	Nitroglycerin

[a] Liposomal suspension diluted ten times using saline solution.

We know that the activation of the complement system causes the formation of the lytic C5b-9 complex bound to the S protein. The concentration of the soluble C5b-9 (SC5b-9) protein complex was investigated *in vitro*, using an enzyme-linked immunosorbent assay (ELISA). Herein, human or animal sera were incubated together with the liposomal drug.

For the negative control, each donor's serum was treated with saline (liposome buffer) or nitroglycerin (liposome payload). For the comparison with established liposomal drugs and the positive control, each donor's serum was treated with Doxil, Abelcet, and zymosan. Doxil is widely used in cancer treatment and consists of PEGylated liposomes below 100 nm in size, encapsulating doxorubicin as the active drug [33]. Abelcet is one of the three commercially available lipid formulations containing amphotericin B, which is used to fight against systemic fungal infections. It consists of ribbon-like complexes 1 to 10 µm in size [34]. Zymosan, a well-known complement activator, is a bacterial glucan applied in experiments to quickly induce inflammation and complement activation [35]. Samples containing the human sera were subjected to SC5b-9 level detection. Furthermore, the three possible pathways, through which the MAC can be formed, were investigated individually through the detection of proteins within the complement cascade including C4d (classical and lectin pathways) and Bb (alternative pathway) protein concentrations. In porcine sera, complement activation was evaluated *via* C3 protein consumption. *In vivo,* the immune system response was investigated by intravenous injection of liposomes into pigs with continuous monitoring of the hemodynamic and hematological changes.

2. Materials and methods

2.1. Materials

A 0.1% commercially available nitroglycerin solution (Perlinganit, UCB-Pharma AG, Bulle, Switzerland, and Nitroglycerin Bioren 0.1%, Sintetica, Mendrisio, Switzerland) was used. PEGylated DSPE (DSPE-PEG2000) was a gift from Lipoid (Ludwigshafen, Germany). Zymosan, chloroform, and methanol were purchased from Merck p.a. (Darmstadt, Germany) and Sigma-Aldrich Chemie GmbH (Buchs, Switzerland). Doxil (Janssen-Cilag International NV, Beerse, Belgium) and Abelcet (Teva Pharmaceutical Works Ltd.) were used as purchased. Saline solution (0.9% NaCl, 308 mOsm/L) was purchased from Teva Pharmaceutical Works Ltd. (Budapest, Hungary) and Bichsel AG (Interlaken, Switzerland). All chemicals were of pharmaceutical grade and used without further purification.

Human serum samples of healthy volunteers were obtained according to the institutionally approved phlebotomy protocol at the Semmelweis University (Budapest, Hungary). Porcine sera were provided by the Institute of Animal Breeding and Nutrition Research Institute (Herceghalom, Hungary). All the sera were stored at a temperature of − 80 °C until use.

2.2. Lipid synthesis

Pad-PC-Pad (1,3-palmitoylamido-1,3-deoxy-*sn*-glycero-2-phosphatidylcholine) was prepared following the reported protocol [11,36]. Briefly, starting from 1,3-dichloropropan-2-ol, the protected phosphate head group was introduced by using phosphoryl chloride, *N*-Boc-aminoethanol, and ammonium hydroxide. Subsequent treatment with sodium azide led to the substitution of both chlorides. A Staudinger-type reduction of the resulting bis-azide yielded the free bis-amine.

Using a Schotten-Baumann-type protocol with palmitoyl chloride, fatty acyl chains were introduced. Finally, the head group was deprotected and quarternized, yielding Pad-PC-Pad. The product was purified sequentially by silica gel column chromatography (silica 63–200, 60 Å, Chemie Brunschwig AG, Basel, Switzerland), using a mixture of chloroform, methanol, and water (65:25:4 v/v/v), by precipitation in cold acetone, and by size exclusion chromatography on Sephadex LH-20 (GE Healthcare Biosciences, Uppsala, Sweden), using a mixture of chloroform, methanol, and water (65:25:4 v/v/v).

2.3. Liposome preparation

The phospholipids were dissolved in chloroform in molar ratios as described in Table 1: L1 and L2 contained Pad-PC-Pad and DSPE-PEG2000, while L3 was formulated from Pad-PC-Pad only. The three liposomal formulations were prepared *via* the standard thin film method [37,38], and they were either hydrated with saline solution, in the case of L2, or passively loaded with commercially available nitroglycerin, in the cases of L1 and L3. Each suspension was prepared in order to get a final lipid concentration of 20 mg/mL, the highest concentration achievable using the Pad-PC-Pad lipids. The suspensions were freeze-thawed in a twelve-step series: Frozen in liquid nitrogen and heated in a 60 °C water bath. In order to get a size distribution of around 100 nm in diameter, each liposomal suspension was downsized by multiple barrel extrusions using Liposofast LF-50 (Avestin Inc., Ottawa, Canada) through track-edged polycarbonate filter membranes (Whatman Nucleopore, Sigma-Aldrich, Buchs, Switzerland) of selected pore sizes: 400 nm (five times), 200 nm (five times), and 100 nm (15 times). The non-encapsulated nitroglycerin in the L1 and L3 suspensions was removed by buffer exchange, using PD-10 desalting columns with 5000 Da size exclusion limit, following the manufacturer's gravity protocol (GE Healthcare Bio-Sciences AB, Uppsala, Sweden). In the *in vitro* experiments, the ten-fold diluted counterparts of L1, L2, and L3 were tested and labeled ‘L1a’, ‘L2a’, and ‘L3a’, respectively. The dilution was carried out using saline solution.

For the *in vivo* experiment, three batches of liposomes, labeled L1′, L2′, and L3′, were prepared using the same lipid composition as L1, L2, and L3, respectively (*cf.* Table 1), and by following the protocol described above. For the samples L1′ and L3′, Perlinganit was used as a drug, whereas the sample L2′ comprised drug-free liposomes. Lipid content was obtained by the phosphate test 2.0 [39]: 12 mg/mL for L1′, 16 mg/mL for L2′, and 11 mg/mL for L3′. All the liposomal suspensions were stored at room temperature until use.

2.4. Liposome characterization

Lipid content in the liposomal suspension was determined after purification by phosphate test 2.0 [39]. Briefly, liposome concentration was calculated from the measured phosphate content (phosphate moiety in the head group of the phospholipids): An aliquot (20 µL) of the liposome suspension was diluted with ultrapure water (180 µL, 18.2 MΩcm) in a 0.5 to 2 mL microwave vial (Biotage, Stockholm, Sweden). Then, 500 µL of a mixture (3/1 v/v) of nitric acid (65% Reag. ISO, Reg. Ph. Eur. grade, Honeywell, Morristown, USA) and sulfuric acid (95% Reag. ISO, Reg. Ph. Eur. grade, Honeywell, Morristown, USA) was added. The vial was sealed and heated in a microwave to a temperature of 180 °C for a period of 20 min (Biotage Initiator, Stockholm, Sweden). The vial was allowed to cool down and the following solutions were added in sequence: Water (2.3 mL), ammonium metavanadate and ammonium heptamolybdate coloring agent (1 mL), and sodium hydroxide solution (10 M, 1 mL). The solution was allowed to rest for ten minutes. The solution was then pipetted into a 96-well plate (Nunc-Immuno plate F96 Polysorb, Roskilde, Denmark), using a multi-channel pipette (eight times 300 µL), and the absorbance was measured at a wavelength of 405 nm, using a plate reader (MultiskanFC 96 from Thermo Scientific, Waltham, USA).

Furthermore, the size of the liposomes, including the polydispersity index (PDI), was obtained by dynamic light scattering (DLS), using a Delsa Nano C (Beckman Coulter, Brea, USA). DLS measurements were performed at a temperature of 25 °C, using two laser diodes working at a wavelength of 658 nm. The scattering angle was set to 165 degrees.

The zeta (ζ) potential of the liposomal formulations was determined by laser Doppler micro-electrophoresis, using a Zetasizer Nano-ZS (Malvern Instruments Ltd., Malvern, UK). The measurements were carried out at a temperature of 25 °C, using a wavelength of 633 nm. The scattering angle was set to 173 degrees, using non-invasive backscattered (NIBS) optics. The experimental data were treated according to the Smoluchowski equation.

The suspensions were diluted 30 times with saline prior to both DLS and ζ potential measurements.

Transmission electron microscopy (TEM) images of the three lipid formulations were obtained at cryogenic temperatures. Prior to the measurements, the three liposomal suspensions were diluted to a concentration of 5 mg/mL and were mounted on glow-discharged holey carbon grids, quickly frozen by a Cryoplunge CP3 system (Gatan Inc., Pleasanton, USA), and transferred to a JEM2200FS transmission electron microscope (JEOL Ltd., Tokyo, Japan) using a Gatan626 cryoholder. Cryo-electron micrographs were recorded at an acceleration voltage of 200 kV at a magnification of 20,000, 4 to 8 µm under-focus, and a dose of 10 electrons/Å^2, using a F416 CMOS detector (TVIPS GmbH, Gauting, Germany).

The morphology of the liposomes exhibits deviations from the spherical shape towards ellipsoids, depending on the lipid composition. The local curvature C and the eccentricity ε of the liposomes were estimated from the cryo-TEM projections (*cf.* Fig. 2). Therefore, ellipses have been employed with a and b the major and minor semi-axes. The curvature of an ellipse can be written as $C = a\,b\,/\,(a^2 \sin^2(t) + b^2 \cos^2(t))^{3/2}$ being t the angle between a and a generic point lying on the ellipse. For sphere-like liposome $a = b = r$, the curvature is given by $C_{\mathrm{circle}} = 1/r$, being r the outer radius of the fitted circle. In case of an elliptically shaped liposome, the local curvature C_{ellipse} ranges from b/a^2 to a/b^2. The eccentricity of an ellipse is given by $\varepsilon = \sqrt{1 - b^2/a^2}$ and ranges as $0 < \varepsilon < 1$; for circles it is zero.

The efficiency of nitroglycerin loading was estimated indirectly from the glucose content of the nitroglycerin solution measured by electrospray ionization mass spectrometry (ESI-MS) using a Bruker Daltonics esquire HCT ion trap mass spectrometry [40]. Here, a volume of 0.1 mL of each sample was diluted ten times with methanol and treated with 10 µL of trifluoroacetic acid. The ESI spectra were measured in the negative mode. The ESI-MS signal of the observed glucose-trifluoroacetic acid adduct at 292.92 amu was compared to the ESI-MS signal which an equally treated solution of nitroglycerin (Bioren 0.1% containing 1 mg/mL nitroglycerin as active pharmaceutical ingredient and 49 mg/mL glucose as excipient) yields. It was assumed that the ratio of glucose *versus* nitroglycerin, as found in the commercial nitroglycerin solution, stays constant during the liposome formulation and purification steps.

2.5. *In vitro immunoassay in human sera via SC5b-9*

Human sera from six donors were aliquoted and stored in Eppendorf tubes at a temperature of − 80 °C. Prior to use, they were thawed to 4 °C and kept in an ice bath. Each human serum was mixed with the three liposomal suspensions (L1, L2, and L3) and their ten-times diluted counterparts (L1a, L2a, L3a). Each serum was treated with saline and nitroglycerin solution being the negative controls. For the comparison with FDA-approved liposomal drugs and as positive control, mixtures of each serum with Doxil (2 mg/mL doxorubicin, 12.7 mg/mL phospholipids), Abelcet (5 mg/mL amphotericin B, 4.9 mg/mL phospholipids), and zymosan (1.5 mg/mL) were used. Each mixture was incubated at a temperature of 37 °C. The reaction was terminated after 5, 10, 20 and 40 min by adding 10 mM ethylenediaminetetraacetic acid (EDTA, Sigma-Aldrich Kft, Budapest, Hungary). The level of SC5b-9 was

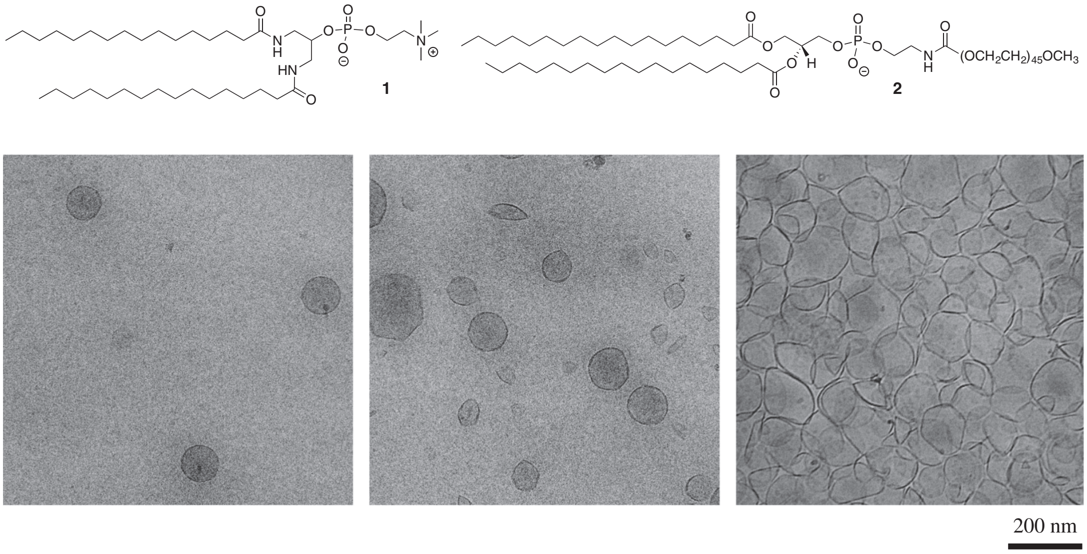

Fig. 2. Structure of the two phospholipids used for the liposome preparations: Pad-PC-Pad (1) and DSPE-PEG2000 (2). Cryo-TEM micrographs of L1 Pad-PC-Pad/DSPE-PEG2000/nitroglycerin (left), L2 Pad-PC-Pad/DSPE-PEG2000/saline (middle), and L3 Pad-PC-Pad/nitroglycerin (right) liposomes. The pure Pad-PC-Pad liposomal suspension contains many aggregated clusters, possibly because the stiff membranes lack repulsive undulation movement. The curvature C of the liposomes was estimated: (51 nm)$^{-1}$ to (44 nm)$^{-1}$ for L1, (130 nm)$^{-1}$ to (10 nm)$^{-1}$ for L2, and (100 nm)$^{-1}$ to (5 nm)$^{-1}$ for L3.

quantified by a MicroVue SC5b-9 Plus ELISA kit (Quidel, San Diego, USA). The assay was carried out following the manufacturer's protocol. Classical and alternative pathways were tested using the MicroVue C4d Plus ELISA and MicroVue Bb Plus ELISA kits (Quidel, San Diego, USA), to detect the concentration of C4d and of Bb, respectively. The samples prepared for SC5b-9, C4d, and Bb assays were diluted 20 times using the specimen diluent provided by the SC5b-9 kit and additional 10 mM EDTA, as the minimum dilution required to detect the optical density. The lectin pathway was investigated using samples treated as described above and supplemented with EGTA/Mg^{2+} (Ca^{2+} chelation), in order to block selectively the classical pathway [41]. In this case, the MicroVue C4d Plus ELISA assay was used to detect C4d concentration. After termination of the reaction, the samples were diluted 30 times with the specimen diluent provided by the C4d kit and additional 10 mM EDTA. Each sample was subjected to a further dilution step before transferring it to the ELISA plate. The optical density was measured with a 96-well plate reader (FLUOstar Omega, BMG Labtech, Ortenberg, Germany) at a wavelength of 450 nm (in the cases of SC5b-9 and Bb) and at a wavelength 405 nm (in the case of C4d).

2.6. *SC5b-9 detection in porcine sera via C3 consumption*

In a previous study [42], we tested complement activation in porcine samples, using the MicroVue Pan-Specific C3 Reagent Kit (Quidel, San Diego, USA). This test, however, is rather qualitative for a study involving porcine sera, because validity has only been demonstrated for human sera. Therefore, we searched for an alternative kit to measure directly the concentration of the SC5b-9 complex in porcine sera. We identified the ELISA kits from MyBioSource Inc. (San Diego, USA) as being possibly suited to this purpose. The manufacturer states that the kit is a quantitative sandwich ELISA assay, to be used for determining the level of SC5b-9 in undiluted original porcine body fluids. Following the guidelines of the manufacturer concerning sample preparation and the assay procedure, we did not find any significant difference between the negative (phosphate-buffered saline) and positive (zymosan) controls. As there was no support available from the supplier, we have to state that the kit was inappropriate for our study. Thereafter, we decided to investigate the level of SC5b-9 in porcine sera through the qualitative detection of C3 consumption, using a MicroVue Pan-Specific C3 Reagent Kit from Quidel Corp., which, to the best of our knowledge, is the only possibility currently available on market.

Each donor's serum was treated with the liposomes, the positive and negative controls as done with the human ones, see description in Section 2.5. As stated above, complement activation in porcine samples was assessed using the Quidel MicroVue Pan-specific C3 reagent kit. This kit allowed for converting the C3 activity in animal samples to the human SC5b-9 protein complex, which could be detected using the SC5b-9 Plus ELISA kit. The optical density was measured with a 96-well plate reader (FLUOstar Omega, BMG Labtech, Ortenberg, Germany) at a wavelength of 450 nm.

2.7. *Statistical analysis*

The statistical analysis was carried out using GraphPad Prism 6 (GraphPad Software Inc., San Diego, USA). All samples, except those incubated with zymosan, were compared with saline after 40 min of incubation, using ordinary one-way ANOVA, followed by Dunnett's multiple comparison test. *P*-values lower than 0.05 were considered as statistically significant.

2.8. *CARPA in the porcine model*

Six domestic male, mixed breed Yorkshire-Hungarian landrace pigs, weighing from 19 to 24 kg, were treated according to the protocol approved by the local Animal Subject Review Committees. Animals were pre-anesthetized intramuscularly with Calypsol/Xilazine 2–3/1.5–2 mL/kg injections in the stalls, to avoid stress, and further anesthesia was maintained with 2 to 3% isoflurane in O_2. Intubation was performed with endotracheal tubes to maintain open airways and to enable controlled ventilation. Spontaneous ventilation was followed by a pulse-oximeter fixed on the tail to monitor oxygen saturation. Temperature was measured rectally and monitored by an Innocare-P anesthesia monitor. A capnograph was connected to the tracheal tube to monitor end tidal CO_2 and respiratory rate (CAP10 Medlab, Medizinische Diagnosegeräte GmbH, Karlsruhe, Germany). Surgery was done after povidone iodine (10%) sterilization of the skin. In order to measure the PAP, a Swan-Ganz catheter (AI-07124, 5 Fr. 110 cm, Arrow International Inc., Reading, USA) was introduced into the pulmonary artery *via* the right external jugular vein, while the SAP was measured in the femoral artery. Blood samples were taken from the left femoral vein, before and after the injection of liposomes (time points after 1, 3, 5, 10, 20, and 30 min), and were collected in hirudin- and K_2-EDTA tubes. Liposome suspensions and zymosan were injected into the animals as bolus within a period of < 10 s *via* the left external jugular vein. Hemodynamic changes (PAP, SAP, and heart rate (HR)) were continuously monitored and either expressed in absolute or in relative terms compared to the baseline throughout this study.

3. Results

3.1. *Liposome characterization*

The total lipid concentration was measured after purification and found to be (20.40 ± 0.16) mg/mL for L1, (16.52 ± 0.10) mg/mL for L2, and (18.72 ± 0.03) mg/mL for L3. Table 2 lists the related DLS and ζ potential results. Within the estimated errors, the results for the liposomes with and without PEGylated lipids were comparable. The measured eccentricity ε of the three liposomal formulations ranged from zero to 0.95 (Table 2); the curvature *C* was estimated (Fig. 2, caption). Preliminary data of the nitroglycerin incorporation efficiency measured by ESI-MS showed 49% for L1 and 27% for L3. These results indicated a beneficial effect of the presence of PEG network for retaining nitroglycerin inside a liposome.

Fig. 2 displays cryo-TEM images representing the morphology of the liposomes. Pure Pad-PC-Pad liposomes formed aggregates (Fig. 2, right), probably due to limited membrane flexibility. Membrane undulation typically contributes to liposome-liposome repulsive forces [43], but this aggregation of Pad-PC-Pad liposomes can be prevented by adding a steric barrier in the form of 5% PEGylated lipids, as indicated in the other two cryo-TEM images (Fig. 2, left and middle). Cryo-TEM data further indicated that the liposome suspensions, containing the PEGylated lipids, were less faceted compared to the liposomes made

Table 2
Characteristics of the liposomal formulations tested *in vitro*.

Label	Lipid composition	Lipid content (mg/mL)	Mean diameter (nm)	PDI	Eccentricity		ζ potential (mV)
					ε_{min}	ε_{max}	
L1	Pad-PC-Pad/DSPE-PEG2000 (nitroglycerin)	20.40 ± 0.16	122 ± 2	0.09 ± 0.01	0	0	− 0.78 ± 0.18
L2	Pad-PC-Pad/DSPE-PEG2000 (bare)	16.52 ± 0.10	151 ± 2	0.21 ± 0.03	0.40 ± 0.01	0.91 ± 0.01	− 1.78 ± 0.14
L3	Pad-PC-Pad (nitroglycerin)	18.72 ± 0.03	166 ± 9	0.19 ± 0.03	0.47 ± 0.01	0.95 ± 0.01	− 0.60 ± 0.15

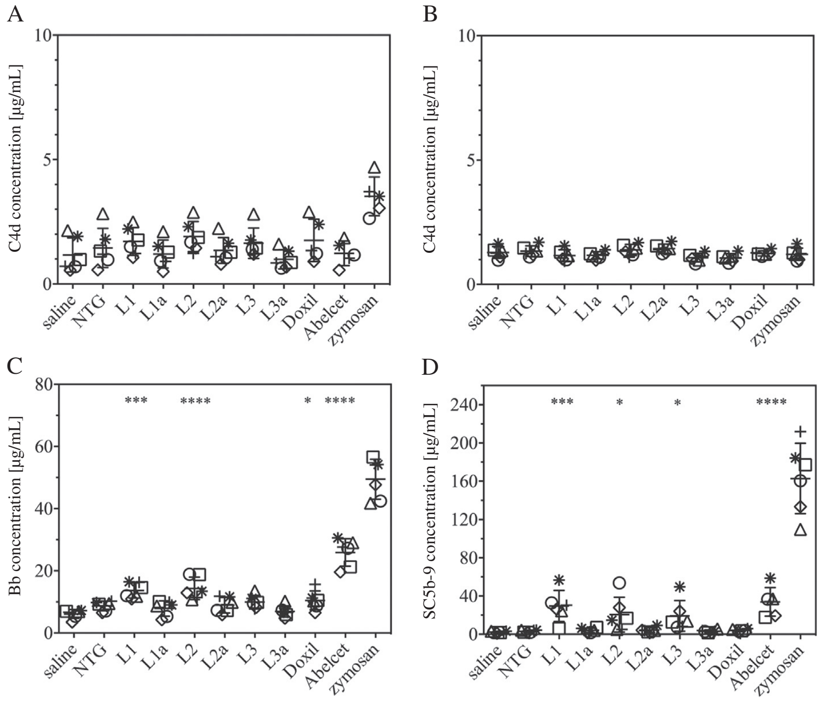

Fig. 3. The level of C4d (A), of C4d supplemented by EGTA/Mg^{2+} (B), of Bb (C), and of SC5b-9 (D) from human sera of six donors incubated for a period of 40 min at a temperature of 37 °C with saline, nitroglycerin (NTG), liposomes containing low (L1a, L2a, L3a) and high (L1, L2, L3) lipid contents, Doxil, Abelcet, and zymosan. The data are presented as mean values, including error bars derived from the standard deviation among the sera. Each symbol (triangle, square, circle, star, cross, rhombus) represents data from one of the six donors. The values were adjusted to the liposome concentrations of 2 and 20 mg/mL, respectively. For the statistical analysis, zymosan was excluded.

from pure Pad-PC-Pad, and the addition of nitroglycerin reduced the faceting of the liposomes, *cf.* Fig. 2. The diameters of liposomes derived from the cryo-TEM images were in agreement with those from the DLS data.

3.2. *In vitro immunoassay in human sera*

Fig. 3 shows the concentration of the protein C4d, without (A) and with (B) the addition of EGTA/Mg^{2+}, Bb (C), and the terminal complex SC5b-9 (D) tested in human sera from six donors. The sera were incubated with the liposomes or the appropriate controls for a period of 40 min. As the experimentally found lipid contents of the three liposomal formulations corresponded to (20.40 ± 0.16) mg/mL for L1, (16.52 ± 0.10) mg/mL for L2, and (18.72 ± 0.03) mg/mL for L3, the obtained data were adjusted to the liposome concentration of 20 mg/mL, in order to mitigate the effect of the lipid concentration on the complement protein levels. Thus, the data were multiplied by the factor 0.98 for L1, 1.21 for L2, and 1.07 for L3. The phosphate test and the DLS results enabled us to estimate the average liposome-entrapped volume, which was 61.7 µL per mL suspension for L1 and 91.4 µL per mL suspension for L3. According to the ESI-MS results, being the encapsulation efficiency 49% for L1 and 27% for L3, the total amount of nitroglycerin per mL suspension was 30.4 µg for L1 and 24.6 µg for L3.

The diagrams in Fig. 3A and B provide the results of the classical and lectin pathways, respectively. For the lectin pathway, the C4d level of the sample containing Abelcet was not available. The C4d concentration of the samples did not show any significant difference compared to saline. The only exception was zymosan, where a slight increase in C4d concentration was observed, as illustrated in the diagram of Fig. 3A.

Bb concentrations, see Fig. 3C, in the samples containing Abelcet and zymosan increased four- and eight-fold with respect to saline. For the liposomal suspensions L1 and L2, Bb concentration was found comparable to Doxil and more than twice that of saline. Liposome suspensions at a lower phospholipid content (L1a, L2a, and L3a), as well as L3, did not show any significant increase in Bb level with respect to saline.

The three pathways can lead to the formation of the terminal complement complex detected by soluble C5b-9 concentration in the serum. Fig. 3D displays the results with respect to the SC5b-9 concentration. It was found that zymosan activated the formation of the SC5b-9 complex within only five minutes of incubation, *cf.* Supplementary information, Fig. S1, and increased up to 80 times after 40 min of incubation as compared to saline. Abelcet increased SC5b-9 concentration > 15 times compared to saline. SC5b-9 concentration in the liposomal suspensions L2 and L3 increased five-fold compared to Doxil and ten-fold compared to the negative control, whereas L1 showed more than seven times and 15 times higher SC5b-9 levels compared to saline and Doxil, respectively. At a lower phospholipid concentration, *i.e.* L1a, L2a, and L3a, the level of SC5b-9 increased less than twice the amount of saline and, within the standard deviation, the results were comparable to Doxil.

The controls and the liposomes were also incubated with each human serum for 5, 10, and 20 min. These data at the selected time points show a trend summarized in Supplementary information, Fig. S1.

3.3. *Validation of the in vitro human sera study*

The results of the *in vitro* study using human sera were underpinned by the *in vitro* assessment of complement activation with porcine sera from six animals, and the *in vivo* experiment with continuous monitoring of the hemodynamic behavior of six Yorkshire pigs after the injection of Pad-PC-Pad liposomes.

3.3.1. *In vitro immunoassay in porcine sera*

The level of complement activation in porcine sera from six animals, tested through C3 consumption, is displayed in Fig. 4. The sample containing saline was used as a baseline. The level of C3 consumption in Abelcet increased up to 72% over the baseline and was twice that of zymosan. Doxil led up to a 20% increase, showing similar complement

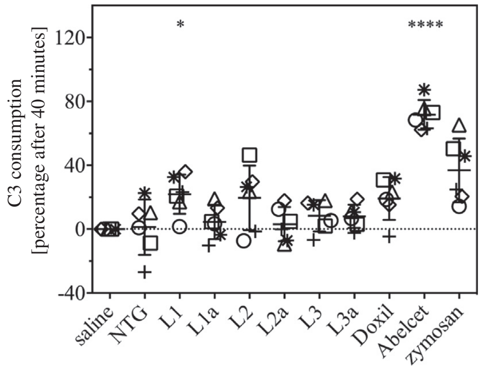

Fig. 4. Complement activation through C3 protein consumption relative to saline in porcine sera from six different animals incubated for a period of 40 min at a temperature of 37 °C with saline and nitroglycerin (NTG), liposomes containing low (L1a, L2a, L3a) and high (L1, L2, L3) lipid contents, Doxil, Abelcet, and zymosan. The data are shown as mean values, including standard deviation among animals. Each symbol (triangle, square, circle, star, cross, rhombus) represents data from one porcine serum. The values were adjusted to liposome concentrations of 2 and 20 mg/mL, respectively. For the statistical analysis, zymosan was excluded.

activity as in L1 and L2 with 22% and 20% rises over saline, respectively. Lower levels of C3 consumption were found for L3 and L3a - an increase of < 10% – and even less for L1a and L2a with increases over the baseline of 4% and 3%, respectively. According to the statistics, significant differences with respect to saline were only found for the undiluted sample containing Pad-PC-Pad/DSPE-PEG2000 loaded with nitroglycerin (L1) and for Abelcet.

3.3.2. *In vivo study in the porcine model*

Six pigs were used to explore in each the hemodynamic changes caused by sequential intravenous administrations of selected liposome boluses, as specified in Tables 3 and 4. L1′ was tested in three doses. L2′ and L3′ were injected using a pre-defined dose in the six animals. At the end of each experiment, zymosan was injected as positive control. The sequences, with which the liposomal formulations were injected, are represented in Supplementary information, see Table S2.

The human therapeutic dose (HTD) of intravenous nitroglycerin solution ranges from 13 to 133 μg in one minute [44,45]. The liposome doses were adjusted in order to obtain 0.5 mg Pad-PC-Pad per kg of pig and flushed into the circulation with 5 mL saline solution. Therefore, the total amounts of phospholipids for the samples containing PEGylated lipids (L1′, L2′) were 0.6 mg/kg (0.5 mg/kg Pad-PC-Pad plus 0.1 mg/kg DSPE-PEG2000) for HTD. Using the same lipid formulation as in L1′, another two nitroglycerin dosages were prepared: 0.33 × HTD and 3 × HTD with a total concentration of 0.2 mg/kg (0.17 mg/kg Pad-PC-Pad plus 0.03 mg/kg DSPE-PEG2000) and 1.8 mg/kg (1.5 mg/kg Pad-PC-Pad plus 0.3 mg/kg DSPE-PEG2000), respectively. According to ESI-MS measurements the dose of nitroglycerin was 94 μg per minute for L1′ and 79 μg per minute for L3′, in agreement with the HTD. As the injection time of the liposomal suspension was about 10 s, the nitroglycerin payload was 0.8 μg per kg pig for L1′ and 0.7 μg per kg pig for L3′.

Table 3
Relative maximal changes in pulmonary arterial pressure. Bolus injections were separated by at least 30-minute recovery periods. Lipid concentrations correspond to the amounts of Pad-PC-Pad per kg (of pig). The sequence of liposomal injection is given in Supplementary information (Table S2).

Pig ID	L1′ 0.5 mg/kg	1/3 × L1′ 0.17 mg/kg	3 × L1′ 1.5 mg/kg	L2′ 0.5 mg/kg	L3′ 0.5 mg/kg
	PAP (%)				
1	14.9	17.7	16.9	4.7	3.5
2	NA	3.5	30.4	8.1	0.0
3	1.9	NA	75.9	2.9	0.0
4	0.0	NA	19.4	8.5	1.5
5	6.3	NA	7.2	NA	4.2
6	6.0	4.8	32.7	1.7	10.1
Mean ± SD	5.8 ± 5.7	8.7 ± 7.9	30.4 ± 24.2	5.2 ± 3.0	3.2 ± 3.8

As expected, the injection of liposomal drugs led to HR modification, a PAP increase, and a change of SAP. In one of the six pigs, the L1′ injection led to a slight increase of HR, which returned to baseline level within minutes. All other samples did not cause any visible change of the HR, besides the gradual, slow increase of the HR during the course of the experiment, owing to anesthesia. Moreover, no cardiac arrhythmia in the form of tachycardia or bradycardia, or extrasystoles, was observed.

Changes in PAP and SAP observed upon injecting the liposomes were calculated as relative changes in percentage terms of the baseline value at pre-injection time. An overview of the recorded PAP, SAP, and HR graphs upon injection of Perlinganit-loaded and drug-free liposomes is represented in the Supplementary information, see Figs. S2 to S7.

The zymosan injection always led to an immediate PAP increase of up to 180%. The injection of 70 μg nitroglycerin, however, caused a decrease in the PAP of maximal 25%. These results set the stage for assessing the CARPA caused by the liposomal suspensions.

The measured maximal changes in PAP upon injecting the corresponding liposomal formulations are listed in Table 3. In all cases, sample L1′ with 1.5 mg/kg of Pad-PC-Pad showed an increase of the PAP of up to 76%, thus indicating mild complement activation. This increase is similar to the hemodynamic changes that occurred following an injection of Doxebo liposomes [25]. Compared to other liposomal drugs, such as Ambisome, where the PAP increases by 200% for an injection of 0.01 mg/kg [27], or Doxil, with an increase up to 400% of the baseline [25] for 0.06 mg/kg phospholipid, the observed increase in PAP with liposomes encapsulating nitroglycerin also had a minimal effect of about a 33% increase in PAP, most likely caused by the aggregation of liposomes [42]. Furthermore, it should be noted that it is only the response to the first injection where cumulative effects can be excluded. In fact, self-induced tolerance, *i.e.*, tachyphylaxis has been known in case of certain liposomes. However, the fact that we saw reactions to the second and third boluses of L1′ argued against full tachyphylaxis after the first injection, enabling us to test L2′ and L3′ at the same doses as L1′ was first injected (0.5 mg/kg). The presence of very similar, small reactions to L2′ and L3′ cannot be explained by tachyphylaxis, as tachyphylaxis prevents follow-up reactions to identical doses, and L1′ was applied three times at much higher doses, which would fully eliminate any further reaction in the presence of tachyphylaxis. Partial tachyphylaxis cannot be ruled out, but overall, these pig data showed very mild changes, which are most likely biologically irrelevant. However, the mere presence of even small hemodynamic changes point to a risk of CARPA in case of substantial overdosing of test liposomes.

3.3.3. *Tachyphylaxis in pigs after Pad-PC-Pad injection*

PAP usually increased after the first liposome injection. The reaction to a subsequent injection showed possible tachyphylaxis. An example of the PAP response is represented in Fig. 5 regarding the injection regimes, with the injection sequence being modified for samples L1′ through L3′. The upper panel on Fig. 5 displays PAP changes in a selected animal, induced by injecting the L1′ samples in order of increasing concentration, starting with the lowest lipid concentration of 0.17 mg/kg and finishing with the highest one of 1.5 mg/kg. The PAP always reached the same level. Changes in PAP monitored in another animal are shown in the lower panel in Fig. 5. When the highest phospholipid concentration was injected first, partial tachyphylaxis was observed.

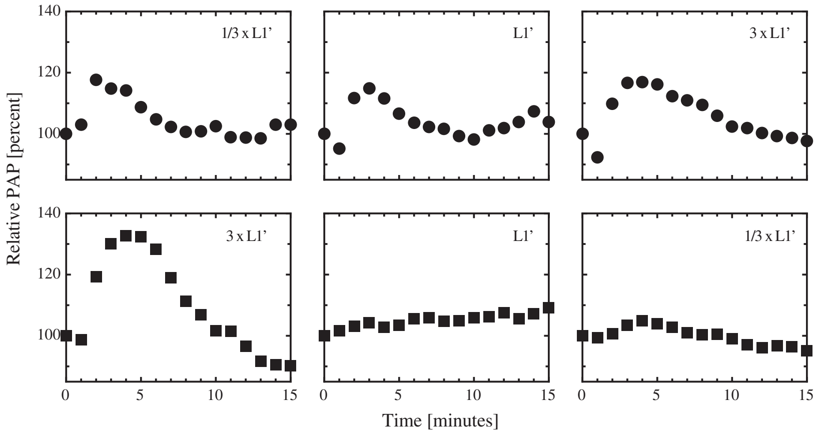

Fig. 5. Injection of PEGylated nitroglycerin-loaded Pad-PC-Pad liposomes in two selected animals. The results for the first animal are represented using filled black circles (three diagrams on the upper row) and the ones for the second animal are given by filled black squares (three diagrams on the lower row). Each row represents a consecutive injection protocol in one animal. The bolus injections were separated by a recovery time of at least 30 min.

Table 4
Relative maximal changes in systemic arterial pressure. Lipid concentrations correspond to the amounts of Pad-PC-Pad per kg (of pig). The sequence of liposomal injection is given in Supplementary information (Table S2).

Pig ID	L1 0.5 mg/kg	1/3 × L1′ 0.17 mg/kg	3 × L1′ 1.5 mg/kg	L2′ 0.5 mg/kg	L3′ 0.5 mg/kg
	SAP (%)				
1	0.0	0.8	9.2	4.9	1.0
2	NA	− 0.4	0.4	2.1	1.5
3	0.0	NA	23.5	0.7	3.5
4	0.0	NA	7.6	2.6	3.3
5	3.6	NA	7.4	NA	2.0
6	1.7	− 0.2	5.7	4.9	4.0
Mean ± SD	1.1 ± 1.6	0.1 ± 0.6	9.0 ± 7.7	3.0 ± 1.8	2.6 ± 1.2

3.3.4. Changes in systemic arterial pressure (SAP)

The extrema of the systemic arterial pressure measurements are listed in Table 4. Contrary to the consistent rise in PAP, SAP showed an immediate increase or decrease of up to 10% for the 0.1 mg/kg zymosan injection, with the type of reaction depending on the individual pig. The injection of 70 μg nitroglycerin caused a maximal decrease of 10% in SAP level. The injection of sample L1′ with 3 × HTD resulted in a significant change in SAP, albeit only for Pig 3.

4. Discussion

Liposome preparation through the extrusion technique is one of the common methods used to generate uniform liposome suspensions [37]. The mean sizes of the liposomes, being 20% to 70% larger than the smallest membrane pore size of the filters used, agrees with previous findings [46]. The liposomes of L2 and L3 exhibit a mean size that reflects their stiffness and degree of faceting. These liposomes were extruded above the membrane main phase transition temperature to facilitate sizing. Nonetheless, parts of the rather stiff membranes of L2 and L3 passed the extrusion filter pores without being sheared, possibly by adopting an orientation along the flow direction.

The ζ potential measurements characterize liposome surfaces and the stability of suspensions, both of which are essential for the efficacy of drug delivery [47]. It has been reported that the presence of PEGylated lipids affects ζ-potential, which depends on PEG size and anchor [27,48]. Our results show ζ-potential values close to zero, regardless of PEGylation (Table 2). This behavior can be explained by Pad-PC-Pad resulting in a neutral, zwitter-ionic amphiphile (Fig. 2, (1)). The addition of negatively charged DSPE-PEG2000 causes the expected marginal decrease in the ζ-potential, as the comparison between L1 and L3 indicates. Encapsulated nitroglycerin has a detectable impact, because the liposomes prepared in saline (L2) show a ζ-potential which is more than twice as high as the value of the formulations with nitroglycerin, *i.e.* L1 and L3.

Due to its simplicity, the passive loading of a drug into a liposome *via* thin lipid film hydration and freeze-thaw steps is widely used. The presence of a PEG network inside and outside of the liposome membrane in the formulations L1 and L2 was solely chosen to prevent the formation of aggregates, which increase the immune system response [42]. Furthermore, the addition of PEGylated lipids seemed to be beneficial to nitroglycerin retention and suggests a noncovalent interaction between the two molecules.

A semi-quantitative ESI-MS assay, carried out for the liposomal formulation L1 and L3, showed a high loading of 27% to 49% nitroglycerin into Pad-PC-Pad liposomes, respectively. The passive loading of nitroglycerin is higher than expected from literature data of passive loading of other drug molecules [49], possibly because of the low nitroglycerin molecular weight being 227.1 Da.

The present study identified the pathway, through which Pad-PC-Pad-based liposomes can trigger the complement system. Although the *in vitro* results of the immunoassay in human sera clearly indicate no activation of the lectin pathway, the result has to be treated with care, because for the lectin pathway test the sample containing Abelcet was unavailable. The classical pathway, however, can definitely be ruled out, as zymosan exhibited the expected rise. The predominant role of the alternative pathway with respect to its classical and lectin counterparts in the presence of PEGylated lipids (L1 and L2 *vs.* L3) agrees with information available in the literature [27,48].

Samples containing Abelcet activated the complement system *via* the alternative pathway stronger than Doxil and Pad-PC-Pad-based liposomes at both high and low phospholipid contents. This enhanced complement activation is possibly associated with the micrometer size of the lipid complexes loaded with the amphotericin B drug. A previous communication [23] reported that larger liposomes increase the risk of severe immune reactions.

It is not surprising that Pad-PC-Pad-based liposome suspensions L1a, L2a, and L3a show a SC5b-9 level similar to the Doxil sample. This behavior is supported by the fact that these liposomes exhibit a size of about hundred nanometers. These formulations caused mild complement activation. In particular, the L1 formulation, comprising Pad-PC-Pad, PEGylated lipid, and the nitroglycerin payload, could trigger the immune system. This fact is interpreted as being the result of amplification caused by combining PEGylated lipids with nitroglycerin, which is in agreement with our results. The same behavior is known for Doxil, as doxorubicin and PEGylated lipids cause a higher response than each component alone [24]. In addition, it has been reported [23] that the presence of drugs in the liposome's surface and in the medium surrounding the liposomes could increase complement activation.

A previous *in vitro* study on Pad-PC-Pad liposomes, where the inner cavity was loaded with phosphate-buffered saline, showed negligible complement activation [42]. The nitroglycerin-loaded Pad-PC-Pad liposomes (L1a, L2a, and L3a) yielded a SC5b-9 level, well comparable to the FDA-approved Doxil, for all tested formulations. Furthermore, C3 protein consumption measured in the sample containing Doxil was comparable to the formulations L1, L2, and L3, a fact explained by the higher sensitivity of the immune system in the porcine model with respect to humans.

In the animal experiments, the administration of drug-free (L2′) and nitroglycerin-loaded (L1′ and L3′) liposomes with dosage up to 3 × HTD highlighted no significant changes in the monitored parameters, a result which agrees with previous data from liposomes of the same composition containing phosphate-buffered saline [42].

In addition to the complement activation by L1 formulation, which can be interpreted as being the result of an amplification caused by combining PEGylated lipids with nitroglycerin, the non-faceted shape of the liposomes has to be considered [13,20]. The cryo-TEM micrographs show that the liposomes prepared with or without the addition of PEGylated lipid and nitroglycerin payload do not only exhibit a size distribution but significantly differ in shape. As the curvature is size- and shape-dependent, it is suitable to characterize the liposome's anisotropy by the eccentricity – an approach, which accounts for the recent interpretation on adverse injection reactions to disk-like and spherical nanoparticles through shape modification [20].

According to the cryo-TEM images, the L3 formulation, where the highest eccentricity was found (*cf.* Table 2), caused the lowest complement activation. On the contrary, the L1 formulation comprising Pad-PC-Pad, PEGylated lipids, and the nitroglycerin payload with zero-eccentricity triggered a mild complement activation. The formulation L2 comprising Pad-PC-Pad, PEGylated lipids and loaded with saline showed eccentricity and complement activation values between the formulations L1 and L3. Therefore, the shape could be a key parameter regulating the acute adverse reactions.

Although the identity of the proteins and receptors, that cause the adverse reactions, remains unknown [20], one may speculate that the angles offered to the protein adsorption by the non-spherical liposomes gain access to the underlying phenomena, as found for nanopyramids influencing inflammatory reactions more than a decade ago [50,51]. Hence, the presence of hydroxyapatite crystallites in bone and the advantage of nanometer-scale roughness on lead-bearing implants is understood. In this context, studies on the three-dimensional structure of Pad-PC-Pad liposomes will follow as a prerequisite for a detailed understanding of acute adverse reactions.

One limitation of the Pad-PC-Pad liposomes for applications inside the human body lies in the main phase transition, which is very close to body temperature. Above 37 °C, the Pad-PC-Pad liposomes release 5(6)-carboxyfluorescein completely [11]. Consequently, for clinical use, one should search for a slightly more stable mechano-responsive container than the proposed Pad-PC-Pad liposomes.

5. Conclusion

Nanometer-sized Pad-PC-Pad liposomes with a concentration of 20 mg/mL initiate the complement cascade *via* the alternative pathway, concluded from an increase in the level of Bb protein. This finding is confirmed by significant differences with respect to saline in the final stage of complement activation, represented by the SC5b-9 concentration, which has been detected as significantly higher than for saline in the final stage of complement activation. Reducing the lipid content of Pad-PC-Pad to 2 mg/mL, the complement activation was negligible, a result derived from the *in vitro* experiments with human and porcine sera as well as an animal study. Therefore, the liposomes developed in this context are promising mechano-responsive container candidates for targeted drug delivery.

Despite the progress in understanding complex processes involving the immune system defenders, the shape of the particles may play a basic role in triggering an immune reaction. To this end, the structure of the liposomes should be better characterized and optimized towards slightly higher transition temperatures.

Future efforts will focus on the release kinetics of these mechano-responsive liposomes of 100 nm diameter for a detailed comparison with currently used non-encapsulated administration methods of nitroglycerin in emergency situations.

Acknowledgments

The authors thank the Swiss National Science Foundation (SNSF) *via* the National Research Program (NRP) 62 ‘Smart Materials’ (Grant No. 126090), which partially funded this work, as well as the European Union Seventh Framework Programme (FP7/2007-2013) grant No. NMP-2012-LARGE-6-309820 (NanoAthero) and (TransInt), FP-7-HEALTH-2013-Innovation-1 (2013) (602923-2) (TheraGlio), and the support by the ‘Applied Materials and Nanotechnology Center of Excellence’, Miskolc University.

Appendix A. Supplementary data

Supplementary data to this article can be found online at http://dx.doi.org/10.1016/j.jconrel.2017.08.010.

References

[1] H.-I. Chang, M.-K. Yeh, Clinical development of liposome-based drugs: formulation, characterization, and therapeutic efficacy, Int. J. Nanomedicine 7 (2012) 49–60.

[2] Y. Fan, Q. Zhang, Development of liposomal formulations: from concept to clinical investigations, Asian J. Pharm. Sci. 8 (2013) 81–87.

[3] D. Peer, J.M. Karp, S. Hong, O.C. Farokhzad, R. Margalit, R. Langer, Nanocarriers as an emerging platform for cancer therapy, Nat. Nanotechnol. 2 (2007) 751–760.

[4] C.M. Dawidczyk, C. Kim, J.H. Park, L.M. Russell, K.H. Lee, M.G. Pomper, P.C. Searson, State-of-the-art in design rules for drug delivery platforms: lessons learned from FDA-approved nanomedicines, J. Control. Release 187 (2014) 133–144.

[5] T. Saxer, A. Zumbuehl, B. Müller, The use of shear stress for targeted drug delivery, Cardiovasc. Res. 99 (2013) 328–333.

[6] S.R. Paliwal, R. Paliwal, G.P. Agrawal, S.P. Vyas, Hyaluronic acid modified pH-sensitive liposomes for targeted intracellular delivery of doxorubicin, J. Liposome Res. 26 (2016) 276–287.

[7] L. Robichaud, D. Ross, M.-H. Proulx, S. Légaré, C. Vacon, X. Xue, E. Segal, Prehospital nitroglycerin safety in inferior ST elevation myocardial infarction, Prehosp. Emerg. Care 20 (2016) 76–81.

[8] F.K. Swirski, M. Nahrendorf, Leukocyte behavior in atherosclerosis, myocardial infarction, and heart failure, Science 339 (2013) 161–166.

[9] M.N. Holme, G. Schulz, H. Deyhle, T. Weitkamp, F. Beckmann, J.A. Lobrinus, F. Rikhtegar, V. Kurtcuoglu, I. Zanette, T. Saxer, B. Müller, Complementary X-ray tomography techniques for histology-validated 3D imaging of soft and hard tissues using plaque-containing blood vessels as examples, Nat. Protoc. 9 (2014) 1401–1415.

[10] W. Yin, S.K. Shanmugavelayudam, D.A. Rubenstein, 3D numerical simulation of coronary blood flow and its effect on endothelial cell activation, Annual International Conference of the IEEE Engineering in Medicine and Biology Society, 2009, pp. 4003–4006.

[11] M.N. Holme, I.A. Fedotenko, D. Abegg, J. Althaus, L. Babel, F. Favarger, R. Reiter, R. Tanasescu, P.-L. Zaffalon, A. Ziegler, B. Muller, T. Saxer, A. Zumbuehl, Shear-stress sensitive lenticular vesicles for targeted drug delivery, Nat. Nanotechnol. 7 (2012) 536–543.

[12] D. Ricklin, J.D. Lambris, Complement-targeted therapeutics, Nat. Biotechnol. 25 (2007) 1265–1275.

[13] S.M. Moghimi, A.J. Andersen, D. Ahmadvand, P.P. Wibroe, T.L. Andresen, A.C. Hunter, Material properties in complement activation, Adv. Drug Deliv. Rev. 63 (2011) 1000–1007.

[14] C.J. Janeway, P. Travers, M. Walport, Immunobiology: The Immune System in Health and Disease, 5th ed., Garland Science, New York, 2001.

[15] S.M. Moghimi, P.P. Wibroe, S.Y. Helvig, Z.S. Farhangrazi, A.C. Hunter, Genomic perspectives in inter-individual adverse responses following nanomedicine administration: the way forward, Adv. Drug Deliv. Rev. 64 (2012) 1385–1393.

[16] S.P. Kastl, W.S. Speidl, C. Kaun, K.M. Katsaros, G. Rega, T. Afonyushkin, V.N. Bochkov, P. Valent, A. Assadian, G.W. Hagmueller, M. Hoeth, R. de Martin, Y. Ma, G. Maurer, K. Huber, J. Wojta, In human macrophages the complement component C5a induces the expression of oncostatin M via AP-1 activation, Arterioscler. Thromb. Vasc. Biol. 28 (2008) 498.

[17] S.M. Moghimi, Complement propriety and conspiracy in nanomedicine: perspective

and a hypothesis, Nucleic Acid Ther. 26 (2016) 67–72.
[18] J.A. Champion, S. Mitragotri, Role of target geometry in phagocytosis, Proc. Natl. Acad. Sci. U. S. A. 103 (2006) 4930–4934.
[19] Y. Geng, P. Dalhaimer, S. Cai, R. Tsai, M. Tewari, T. Minko, D.E. Discher, Shape effects of filaments versus spherical particles in flow and drug delivery, Nat. Nanotechnol. 2 (2007) 249–255.
[20] P.P. Wibroe, A.C. Anselmo, P.H. Nilsson, A. Sarode, V. Gupta, R. Urbanics, J. Szebeni, A.C. Hunter, S. Mitragotri, T.E. Mollnes, S.M. Moghimi, Bypassing adverse injection reactions to nanoparticles through shape modification and attachment to erythrocytes, Nat. Nanotechnol. 12 (2017) 589–594.
[21] J. Szebeni, Complement activation-related pseudoallergy: a stress reaction in blood triggered by nanomedicines and biologicals, Mol. Immunol. 61 (2014) 163–173.
[22] S.M. Moghimi, Z.S. Farhangrazi, Nanomedicine and the complement paradigm, Nanomedicine: NBM 9 (2013) 458–460.
[23] J. Szebeni, F. Muggia, A. Gabizon, Y. Barenholz, Activation of complement by therapeutic liposomes and other lipid excipient-based therapeutic products: prediction and prevention, Adv. Drug Deliv. Rev. 63 (2011) 1020–1030.
[24] J. Szebeni, P. Bedőcs, Z. Rozsnyay, Z. Weiszhár, R. Urbanics, L. Rosivall, R. Cohen, O. Garbuzenko, G. Báthori, M. Tóth, R. Bünger, Y. Barenholz, Liposome-induced complement activation and related cardiopulmonary distress in pigs: factors promoting reactogenicity of Doxil and AmBisome, Nanomedicine: NBM 8 (2012) 176–184.
[25] J. Szebeni, P. Bedőcs, R. Urbanics, R. Bünger, L. Rosivall, M. Tóth, Y. Barenholz, Prevention of infusion reactions to PEGylated liposomal doxorubicin via tachyphylaxis induction by placebo vesicles: a porcine model, J. Control. Release 160 (2012) 382–387.
[26] J. Szebeni, J.L. Fontana, N.M. Wassef, P.D. Mongan, D.S. Morse, D.E. Dobbins, G.L. Stahl, R. Bünger, C.R. Alving, Hemodynamic changes induced by liposomes and liposome-encapsulated hemoglobin in pigs, Circulation 99 (1999) 2302.
[27] L. Dézsi, T. Fülöp, T. Mészáros, G. Szénási, R. Urbanics, C. Vázsonyi, E. Őrfi, L. Rosivall, R. Nemes, R.J. Kok, J.M. Metselaar, G. Storm, J. Szebeni, Features of complement activation-related pseudoallergy to liposomes with different surface charge and PEGylation: comparison of the porcine and rat responses, J. Control. Release 195 (2014) 2–10.
[28] J. Szebeni, L. Baranyi, S. Sávay, M. Bodó, J. Milosevits, C.R. Alving, R. Bünger, Complement activation-related cardiac anaphylaxis in pigs: role of C5a anaphylatoxin and adenosine in liposome-induced abnormalities in ECG and heart function, Am. J. Physiol. Heart Circ. Physiol. 290 (2006) H1050–H1058.
[29] J. Szebeni, L. Baranyi, S. Savay, M. Bodo, D.S. Morse, M. Basta, G.L. Stahl, R. Bünger, C.R. Alving, Liposome-induced pulmonary hypertension: properties and mechanism of a complement-mediated pseudoallergic reaction, Am. J. Phys. 279 (2000) H1319–H1328.
[30] J. Szebeni, P. Bedőcs, D. Csukás, L. Rosivall, R. Bünger, R. Urbanics, A porcine model of complement-mediated infusion reactions to drug carrier nanosystems and other medicines, Adv. Drug Deliv. Rev. 64 (2012) 1706–1716.
[31] European Medicine Agency, EMA/CHMP/806058/2009/Rev. 02, (2013).
[32] J. Szebeni, Hemocompatibility testing for nanomedicines and biologicals: predictive assays for complement mediated infusion reactions, Eur. J. Nanomed. 5 (2012) 33–53.
[33] Y. Barenholz, Doxil® — the first FDA-approved nano-drug: lessons learned, J. Control. Release 160 (2012) 117–134.
[34] J.P. Adler-Moore, R.T. Proffitt, Amphotericin B lipid preparations: what are the differences? Clin. Microbiol. Infect. 14 (2008) 25–36.
[35] F.J. Di Carlo, V.J. Fiore, On the composition of zymosan, Science 127 (1958) 756–757.
[36] I.A. Fedotenko, P.-L. Zaffalon, F. Favarger, A. Zumbuehl, The synthesis of 1,3-diamidophospholipids, Tetrahedron Lett. 51 (2010) 5382–5384.
[37] P. Walde, Preparation of vesicles (liposomes), Encycl. Nanosci. Nanotechnol. 9 (2004) 43–79.
[38] F. Olson, C.A. Hunt, F.C. Szoka, W.J. Vail, D. Papahadjopoulos, Preparation of liposomes of defined size distribution by extrusion through polycarbonate membranes, Biochim. Biophys. Acta 557 (1979) 9–23.
[39] E. Stalder, A. Zumbuehl, Phosphate test 2.0, CHIMIA Int. J. Chem. 67 (2013) 819–821.
[40] S. Ardekani, H.A. Scott, S. Gupta, S. Eum, X. Yang, A.R. Brunelle, S.M. Wilson, U. Mohideen, K. Ghosh, Nanoliposomal nitroglycerin exerts potent anti-inflammatory effects, Sci Rep 5 (2015) 16258.
[41] O.B. Spiller, B.P. Morgan, Antibody-independent activation of the classical complement pathway by cytomegalovirus-infected fibroblasts, J Infect Dis 178 (1998) 1597–1603.
[42] S. Bugna, M. Buscema, S. Matviykiv, R. Urbanics, A. Weinberger, T. Meszaros, J. Szebeni, A. Zumbuehl, T. Saxer, B. Müller, Surprising lack of liposome-induced complement activation by artificial 1,3-diamidophospholipids in vitro, Nanomedicine: NBM 12 (2016) 845–849.
[43] E. Sackmann, Membrane bending energy concept of vesicle- and cell-shapes and shape-transitions, FEBS Lett. 346 (1994) 3–16.
[44] Bioren https://compendium.ch/mpro/mnr/24894/html/fr.
[45] Perlinganit https://compendium.ch/mpro/mnr/19338/html/de.
[46] S.G.M. Ong, M. Chitneni, K.S. Lee, L.C. Ming, K.H. Yuen, Evaluation of extrusion technique for nanosizing liposomes, Pharmaceutics 8 (2016) 36.
[47] F.J. Carrión, A. De La Maza, J.L. Parra, The influence of ionic strength and lipid bilayer charge on the stability of liposomes, J. Colloid Interface Sci. 164 (1994) 78–87.
[48] J.M. van den Hoven, R. Nemes, J.M. Metselaar, B. Nuijen, J.H. Beijnen, G. Storm, J. Szebeni, Complement activation by PEGylated liposomes containing prednisolone, Eur. J. Pharm. Sci. 49 (2013) 265–271.
[49] J. Gubernator, Active methods of drug loading into liposomes: recent strategies for stable drug entrapment and increased in vivo activity, Expert. Opin. Drug Deliv. 8 (2011) 565–580.
[50] M. Riedel, B. Müller, E. Wintermantel, Protein adsorption and monocyte activation on germanium nanopyramids, Biomaterials 22 (2001) 2307–2316.
[51] B. Müller, Natural formation of nanostructures: from fundamentals in metal heteroepitaxy to applications in optics and biomaterials science, Surf. Rev. Lett. 08 (2001) 169–228.

SUPPLEMENTARY INFORMATION

Immunological response to nitroglycerin-loaded shear-responsive liposomes *in vitro* and *in vivo*

Marzia Buscema[a], Sofiya Matviykiv[a], Tamás Mészáros[b,c], Gabriela Gerganova[a],
Andreas Weinberger[d], Ute Mettal[d], Dennis Mueller[d], Frederik Neuhaus[d], Etienne Stalder[d],
Takashi Ishikawa[e], Rudolf Urbanics[c], Till Saxer[f], Thomas Pfohl[a], János Szebeni[b,c],
Andreas Zumbuehl[d] and Bert Müller[a]

[a]*Biomaterials Science Center, Department of Biomedical Engineering, University of Basel, Allschwil, Switzerland*
[b]*Nanomedicine Research and Education Center, Semmelweis University Budapest, Hungary*
[c]*SeroScience Ltd, Budapest, Hungary*
[d]*Department of Chemistry, University of Fribourg, Fribourg, Switzerland*
[e]*Paul Scherrer Institute (PSI), Villigen, Switzerland*
[f]*Cardiology Division, University Hospital of Geneva, Geneva, Switzerland*

* Corresponding author at: Biomaterials Science Center, Department of Biomedical Engineering, University of Basel, 4123 Allschwil, Gewerbestrasse 14, Switzerland, Tel: +41 61 207 54 30

E-mail address: bert.mueller@unibas.ch (B. Müller).

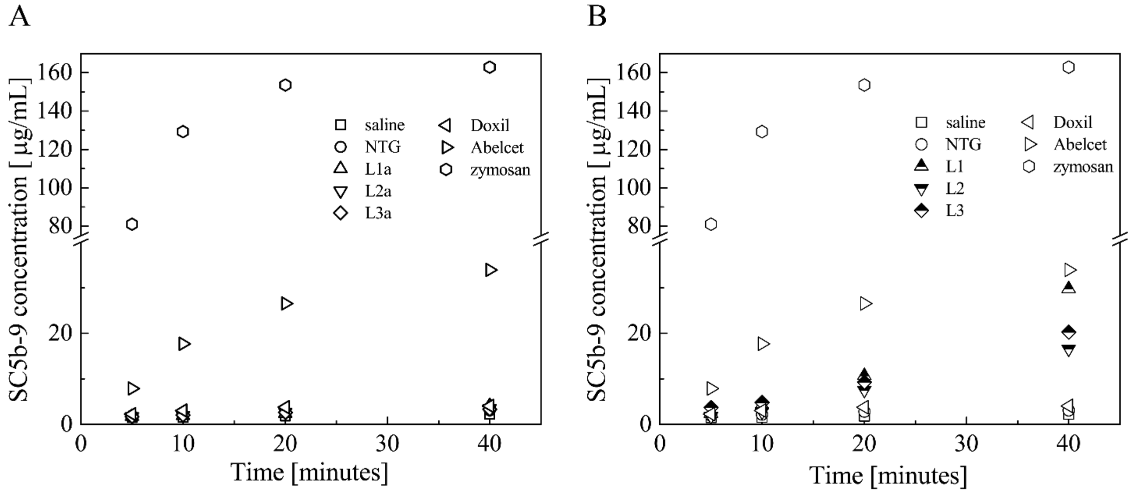

Fig. S1. Time point *in vitro* experiment. SC5b-9 concentration of six human sera incubated at a temperature of 37 °C with the positive, negative controls and liposomes at high lipid content (A) and at low lipid content (B). The data are shown as the mean value among the six donors. The reaction was terminated after 5, 10, 20, and 40 minutes. The data were sorted as A and B, in order to visualize clearly the SC5b-9 level of the Pad-PC-Pad-based liposomes at high and low lipid content.

Table S2
Temporal sequences of liposomal injections in the six pigs, from left to right. L1’ was administrated in three liposomal concentrations, while L2’ and L3’ in a single concentration. For each injection, the pulmonary arterial pressure, PAP, and systemic arterial pressure, SAP, and heart rate, HR, were recorded and displayed in Figures S3 to S8.

Pig ID	Injection							
	#1	#2	#3	#4	#5	#6	#7	#8
1	1/3 × L1’	L1’	3 × L1’	L2’	L3’	Perlinganit	zymosan	
2	saline	3 × L1’	L2’	L3’	Perlinganit	1/3 × L1’	zymosan	
3	saline	3 × L1’	L1’	L2’	L3’	Perlinganit	zymosan	
4	saline	L1’	3 × L1’	L2’	L3’	Perlinganit	zymosan	
5	saline	L1’	3 × L1’	L3’	Perlinganit	zymosan		
6	saline	3 × L1’	L1’	1/3 × L1’	L2’	L3’	Perlinganit	zymosan

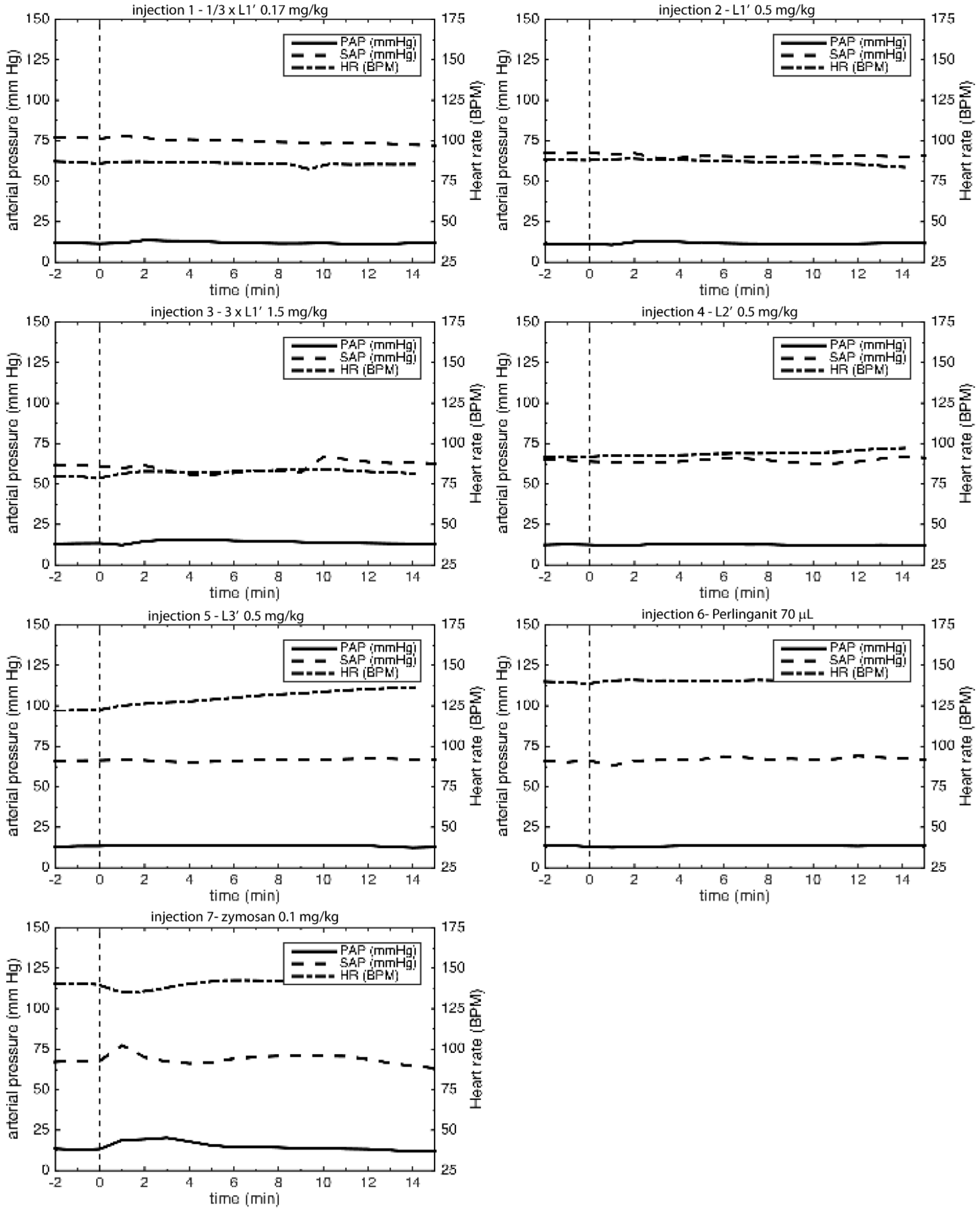

Fig. S3. Pig 1 (21 kg male)—Summary: Monitoring of PAP, SAP, and HR changes after injection; dashed line denotes injection time.

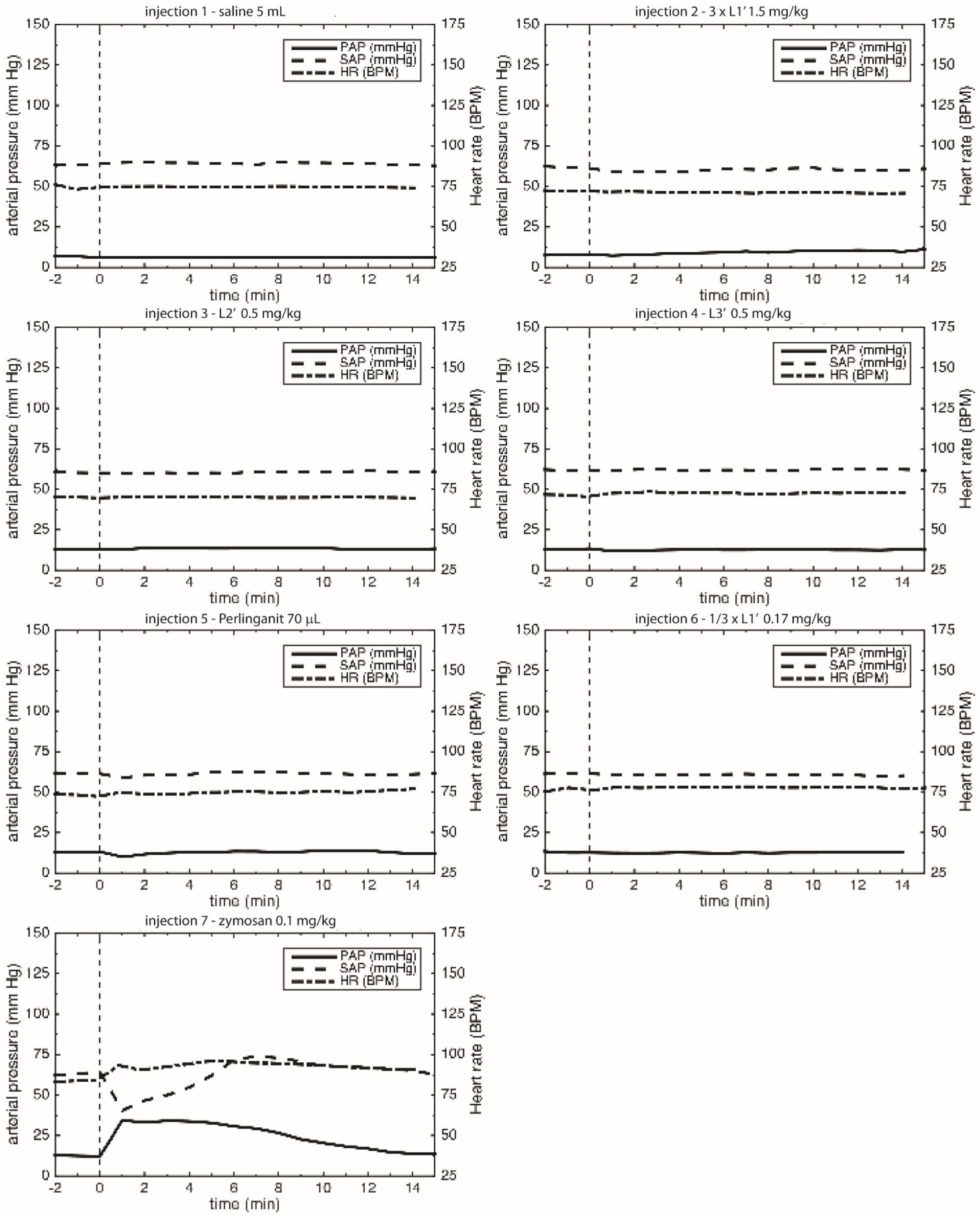

Fig. S4. Pig 2 (20 kg male)—Summary: Monitoring of PAP, SAP, and HR changes after injection; dashed line denotes injection time.

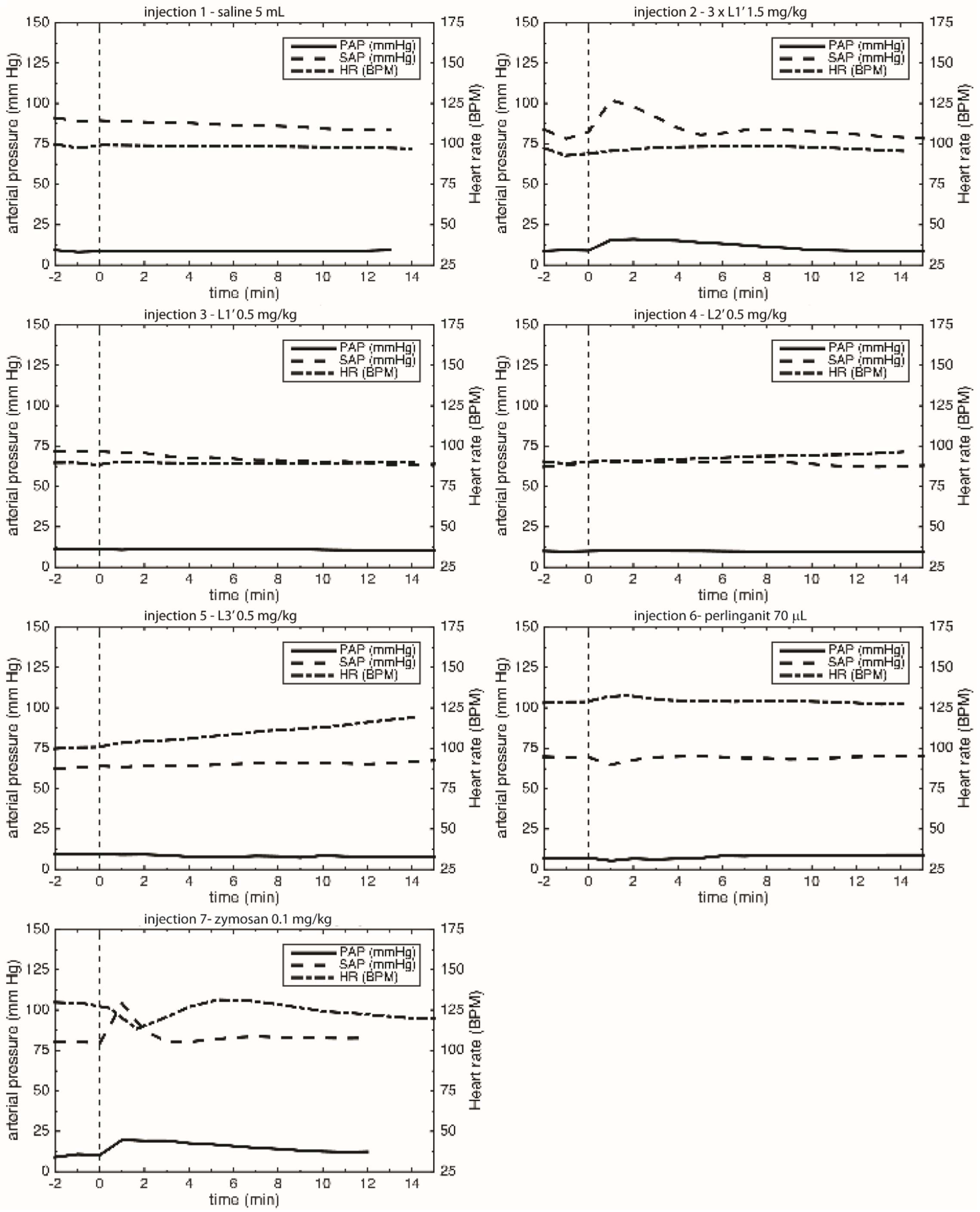

Fig. S5. Pig 3 (22 kg male)—Summary: Monitoring of PAP, SAP, and HR changes after injection; dashed line denotes injection time.

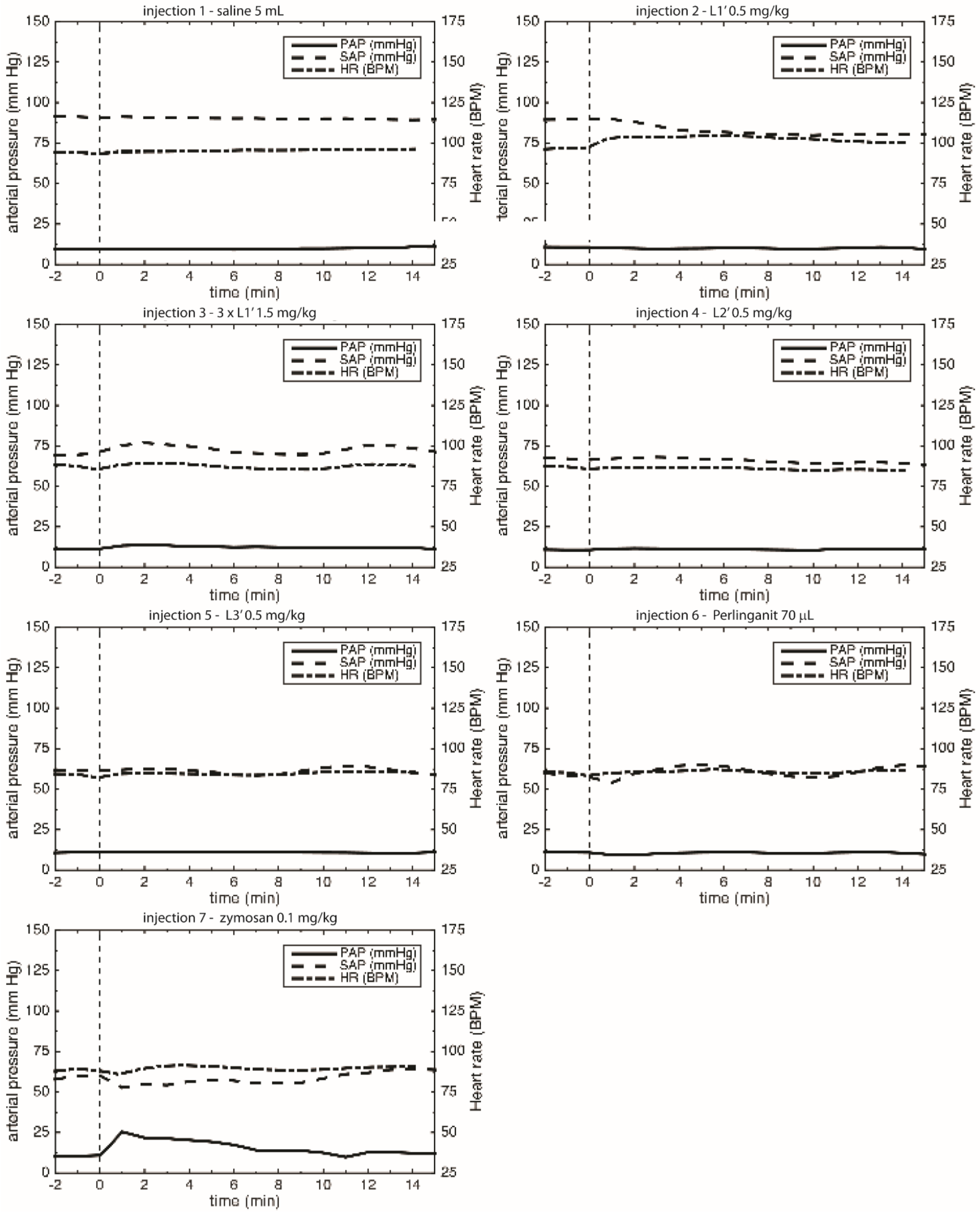

Fig. S6. Pig 4 (19 kg male)—Summary: Monitoring of PAP, SAP, and HR changes after injection; dashed line denotes injection time.

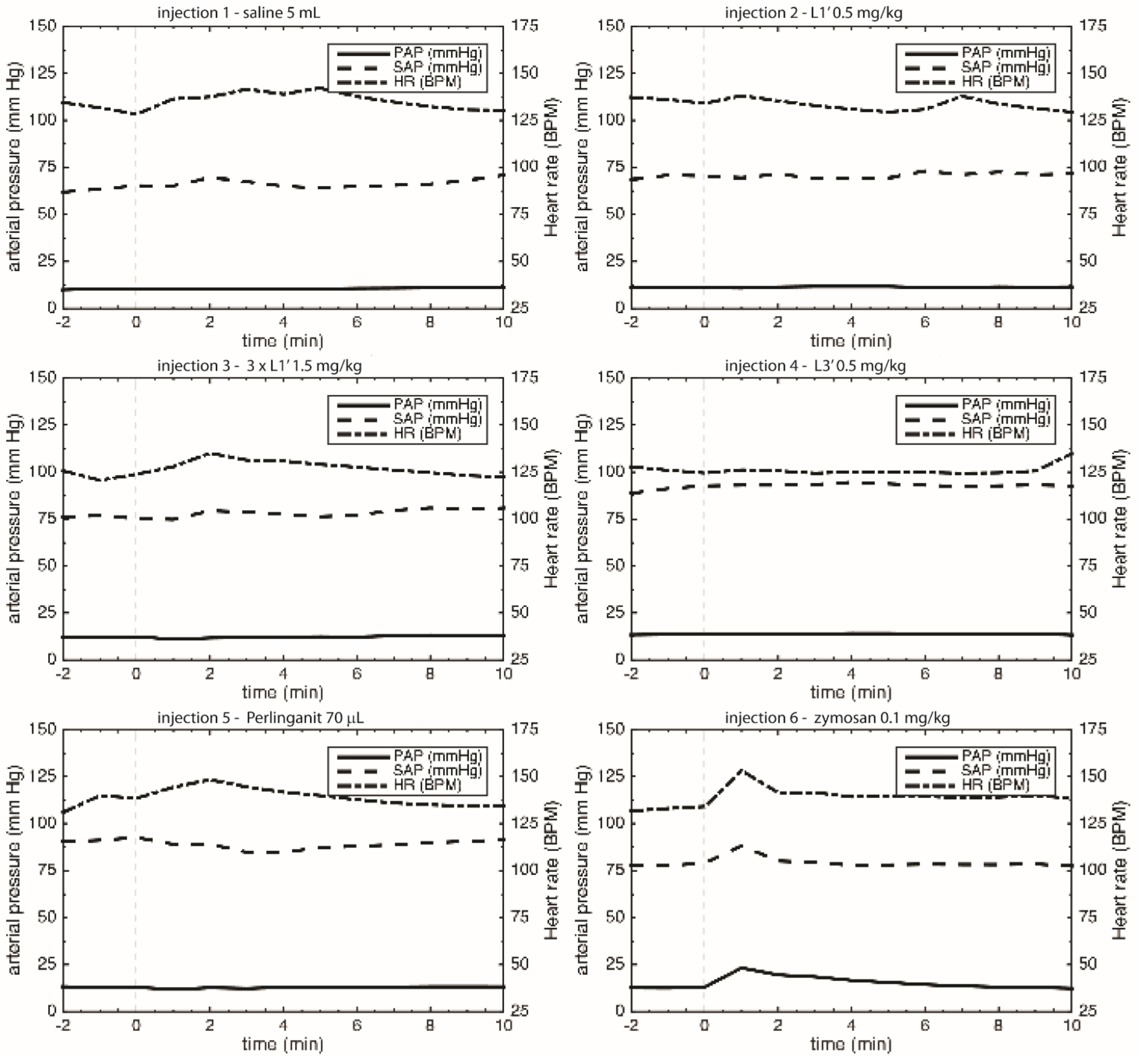

Fig. S7. Pig 5 (19 kg male)—Summary: Monitoring of PAP, SAP, and HR changes after injection; dashed line denotes injection time.

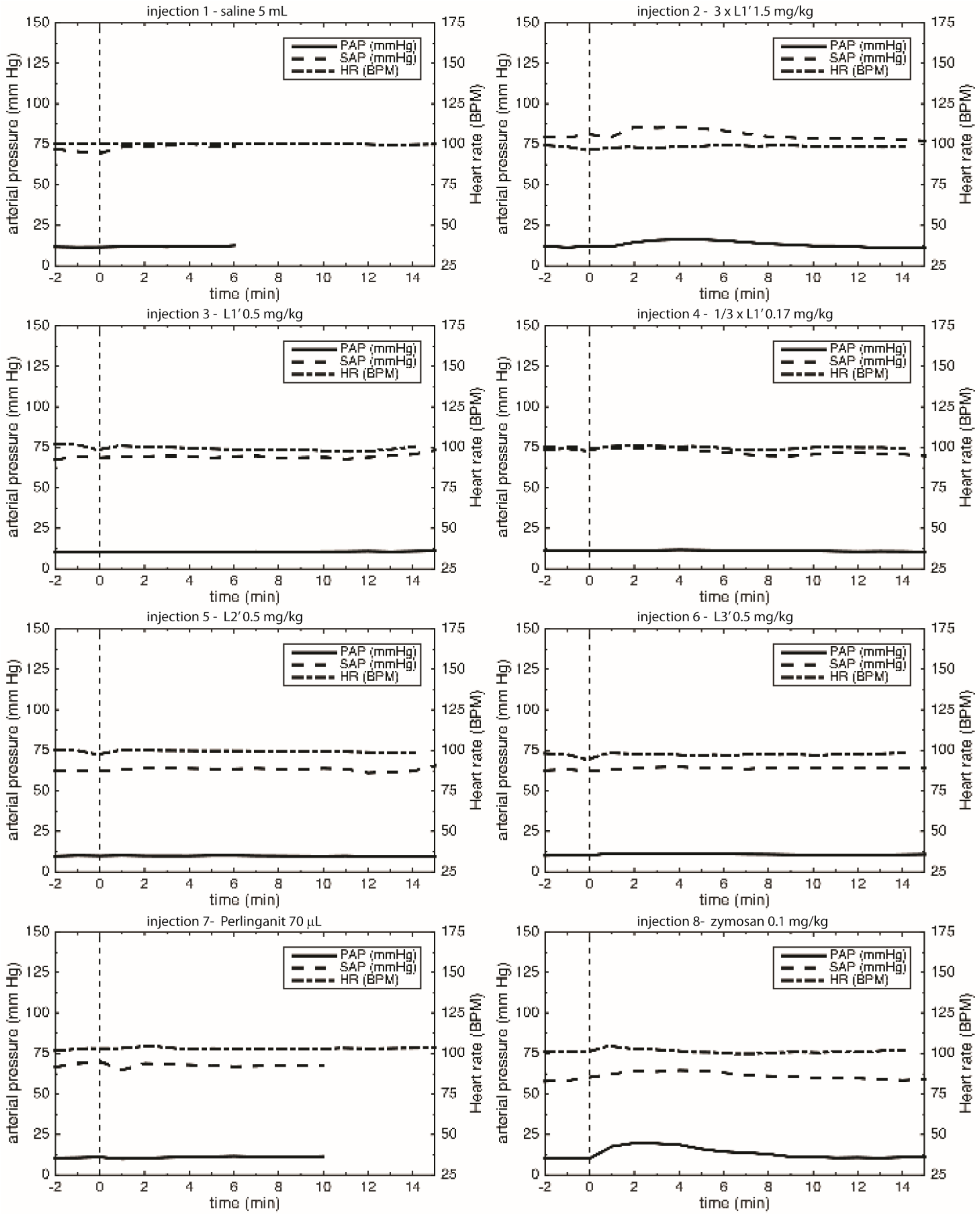

Fig. S8. Pig 6 (24 kg male)—Summary: Monitoring of PAP, SAP, and HR changes after injection; dashed line denotes injection time.

Contributors

The content of the *Results* chapter was achieved thanks to the collaboration among chemists, physicists, computational scientists, medical doctors, biologists and immunologists. The work of the author of this thesis (M.B.) was supported by the precious contributions of Prof. Dr. Bert Müller (B.M.), Dr. Simone E. Hieber (S.E.H.), Dr. Hans Deyhle (H.D.), Dr. Georg Schulz (G.S.), Dr. Thomas Pfohl (T.P.), Prof. Dr. Andreas Zumbuehl (A.Z.), Etienne Stalder (E.S.), Dennis Mueller (D.M.), Dr. Andreas Weinberger (A.W.), Dr. Ute Mettal (U.M.), Frederik Neuhaus (F.N.), Dr. Till Saxer (T.S.), Dr. Johannes A. Lobrinus (J.A.L.), Sofiya Matviykiv (S.M.), Gabriela Gerganova (G.G.), Dr. Christos Bikis (C.B.), Dr. Felix Beckmann (F.B.), Alexander Hipp (A.H.), Dr. János Szebeni, Tamás Mészáros, Dr. Rudolf Urbanics (R.U.), Dr. Takashi Ishikawa (T.I.).

M.B. contributed significantly in the following phases of the three subprojects: study design, conducting the experiments, data evaluation, and preparation of the manuscripts.

The contributions of the co-authors are listed for each chapter of section *Results*. All co-workers participated actively in discussing the results, and provided critical feedback on the related manuscripts. The co-authors' order corresponds to the order shown in author's list of the manuscripts.

Section 2.1:

S.E.H.: Assistance with the implementation of the iterative procedure reported in the "Results" section. Assistance with writing the "Materials and Methods section".

G.S.: Assistance during the data acquisition. Assistance with the data registration. Suggestions for the data interpretation and figure preparation. Assistance with writing the "Material and Methods section".

H.D.: Suggestion for the data interpretation.

A.H.: Assistance with the data reconstruction.

F.B.: Assistance during the data acquisition.

J.A.L.: The specimen preparation. Provided the specimen decalcified and the histological sections. Assistance with writing the "Materials and Methods section".

T.S.: Provided the specimen. Assistance with the specimen preparation.

B.M.: Initiation of the study. Assistance with the study design. Assistance with the writing of the "Introduction" and "Results and Discussion" sections. Critical reviewing of the manuscript for content. Suggestions for the graphical representation of figures.

Section 2.2:

H.D.: Assistance with figure preparation.
T.P.: Suggestion for microfluidic device preparation. Assistance with writing the "Materials and Methods section".
S.E.H.: Assistance with figure preparation.
A.Z.: Initiation of the study. Provided the lipids.
B.M.: Initiation of the study. Assistance with the study design. Assistance with the writing of the "Introduction" and "Results and Discussion" sections. Critical reviewing of the manuscript for content. Suggestions for the graphical representation of figures.

Section 2.3:

H.D.: Assistance during the data acquisition. Suggestion for the data interpretation. Assistance with data analysis and figure preparation.
T.P.: Assistance during the data acquisition. Suggestion for the data interpretation. Assistance with writing the "Materials and Methods section".
T.I.: The specimen characterization. Provided the cryo-TEM image.
A.Z.: Initiation of the study. Provided the lipids.
B.M.: Initiation of the study. Assistance with the study design. Assistance with the writing of the "Introduction" and "Results and Discussion" sections. Critical reviewing of the manuscript for content. Suggestions for the graphical representation of figures.

Section 2.4:

S.M.: Assistance during the sample preparation, assistance during the *in vitro* experiment and figure preparation.
T.M.: Assistance during the *in vitro* experiment and data interpretation.
G.G.: Assistance during the sample preparation, and the *in vitro* experiment.
A.W.: Performed the *in vivo* experiment.
U.M.: Worked on the lipid synthesis. Assistance with writing the "Materials and Methods" section.
D.M.: The specimen preparation. Worked on the lipid synthesis.
F.N.: The specimen preparation. Worked on the lipid synthesis.
E.S.: The specimen characterization. Assistance during the sample characterization.
T.I.: The specimen characterization. Provided the cryo-TEM images.
R.U.: Assistance during the *in vivo* experiment and with the data interpretation.
T.S.: Assistance with writing the "Materials and Methods" section.
T.P.: Assistance with writing the "Materials and Methods" section.
J.S.: Assistance with the study design and data interpretation.
A.Z.: Assistance with the study design. Provided the lipids.
B.M.: Initiation of the study. Assistance with the study design. Assistance with the writing of the "Introduction" and "Results and Discussion" sections. Critical reviewing of the manuscript for content. Suggestions for the graphical representation of figures.

3 Conclusions and Outlook

The properties of Pad-PC-Pad liposomes have to be tuned to ensure a release of the drug only at constricted area of diseased blood vessels. For this reason the morphology of obstructed blood vessels was investigated with particular attention to the artery lumen, which is inevitably reduced when plaque starts to form.

Synchrotron radiation-based phase µCT provided non-destructive, 3D rendering of the specimen with suitable contrast for both high (plaque) and low (vessel walls, fat, muscle) X-ray absorbing tissues present in the diseased artery. Tomography datasets of the sample fixed in formalin and embedded in paraffin were recorded. After the decalcification procedure and the re-embedding in paraffin, tomography data were acquired in absorption contrast using both table-top laboratory and synchrotron radiation sources. Tomography slices were compared to the histological counterparts. Although the main features of the specimen were present both in tomography and histology, some additional deformations due to histological sectioning could not be avoided.

The results indicated that formalin fixation is the most appropriate procedure, among the others here investigated, for imaging the specimen using µCT, as it enabled localizing the plaque with reasonable precision. However, gas bubble formation arising during the scan remains a crucial issue, that needs to be circumvented in order to improve the quality of the lumen segmentation.

Microfluidics enabled mimicking a constricted blood vessel and SAXS provided access to possible structural changes of Pad-PC-Pad liposomes when subjected to an external perturbation. We report the successful detection of the liposomes within the microfluidic device, despite the low lipid concentration achievable during the preparation. The results indicated that Pad-PC-Pad liposomes subjected to shear gradient modify their structure. This behavior was not observed in liposomes prepared using DPPC phospholipid.

In this study, several shear rates have been tested, however only three of them have been reported. Higher shear rates caused the formation of big air bubbles within the microfluidic channel, which made the recorded data unusable. Further studies should focus on improving the fabrication of the microfluidic device, e.g. strength to higher flow rates.

The complex behavior of Pad-PC-Pad liposomes under flow conditions suggests further efforts to fully understand their structural properties.

In the future, it would be advised to study dye-release by the liposomes exploiting fluorescence microscopy and microchannels based on polydimethylsiloxane. Furthermore, it would be beneficial to investigate the membrane rigidity of the liposomes by means of atomic force microscopy in liquid environment, an approach complementary to SAXS and microfluidics.

For the immediate treatment of arteries occlusion, Pad-PC-Pad liposomes are envisioned for intravenous injection. The direct contact with human blood can result in adverse immune reactions. CARPA is one of the most common safety issues and reasons for nanomedicines failure. Therefore, the *in vitro* and *in vivo* tests with Pad-PC-Pad liposomes were performed. Pad-PC-Pad liposomes loaded with a vasodilatory drug and incubated in human sera and pig plasma might initiate the complement cascade via the alternative pathway. The *in vitro* studies were confirmed by the animal study where no significant changes, in the continuously monitored hemodynamic parameters, were observed. Activation of the complement system anaphylatoxins can also trigger cytokine-mediated inflammation. Consequently, it would be advised to detect the impact of Pad-PC-Pad liposomes upon activation of pro-inflammatory cytokines.

One limitation of the Pad-PC-Pad liposomes for applications within the human body lies in the main phase transition temperature, which is very close to body temperature. In fact, above 37°C, Pad-PC-Pad liposomes release their cargo completely. Consequently, for clinical use, it would be beneficial to develop more thermally stable mechano-responsive nano-carriers than those discussed here.

Bibliography

[1] WHO, "World health organisation." `http://www.who.int/cardiovascular_diseases/en/`.

[2] Wellnhofer, E., Osman, J., Kertzscher, U., Affeld, K., Fleck, E., and Goubergrits, L., "Non-dimensional modeling in flow simulation studies of coronary arteries including side-branches: a novel diagnostic tool in coronary artery disease," *Atherosclerosis* **216**(2), 277–282 (2011).

[3] Torchilin, V., "Recent advances with liposomes as pharmaceutical carriers," *Nature Reviews Drug Discovery* **4**(2), 145–160 (2005).

[4] Holme, M. N., Fedotenko, I. A., Abegg, D., Althaus, J., Babel, L., Favarger, F., Reiter, R., Tanasescu, R., Zaffalon, P.-L., Ziegler, A., Müller, B., Saxer, T., and Zumbuehl, A., "Shear-stress sensitive lenticular vesicles for targeted drug delivery," *Nature Nanotechnology* **7**(8), 536–543 (2012).

[5] Habbel, C., Hetterich, H., Willner, M., Herzen, J., Steigerwald, K., Auweter, S., Schüller, U., Hausleiter, J., Massberg, S., Reiser, M., Pfeiffer, F., Saam, T., and Bamberg, F., "Ex vivo assessment of coronary atherosclerotic plaque by grating-based phase-contrast computed tomography: Correlation with optical coherence tomography," *Investigative Radiology* **52**(4), 223–231 (2017).

[6] Kume, T. and Uemura, S., "Current clinical applications of coronary optical coherence tomography," *Cardiovascular intervention and therapeutics* **33** (2017).

[7] Yin, W., Shanmugavelayudam, S. K., and Rubenstein, D. A., "3d numerical simulation of coronary blood flow and its effect on endothelial cell activation," *Conference proceedings IEEE in Engineering in Medicine and Biology Society, 2009* , 4003–4006 (2009).

[8] Molloy, C. P., Yao, Y., Kammoun, H., Bonnard, T., Hoefer, T., Alt, K., Trovar-Lopez, F., Rosengarten, G., Ramsland, P. A., Meer, A. D., Berg, A., Murphy, A. J., Hagemeyer, C. E., Peter, K., and Westein, E., "Shear-sensitive nanocapsule drug release for site- specific inhibition of occlusive thrombus formation," *Journal of Thrombosis and Haemostasis* **15**(5), 972–982 (2016).

[9] Korin, N., Kanapathipillai, M., Matthews, B. D., Crescente, M., Brill, A., Mammoto, T., Ghosh, K., Jurek, S., Bencherif, S. A., Bhatta, D., Coskun, A. U., Feldman, C. L., Wagner, D. D., and Ingber, D. E., "Shear-activated nanotherapeutics for drug targeting to obstructed blood vessels," *Science* **337**(6095), 738–742 (2012).

[10] Hibi, K., Kimura, K., and Umemura, S., "Clinical utility and significance of intravascular ultrasound and optical coherence tomography in guiding percutaneous coronary interventions," *Circulation Journal* **79**(1), 24–33 (2014).

[11] Nissl, F., "Über die sogenannten granula der nervenzellen," *Neurol. Centralblatt* **13**, 781–789 (1894).

[12] Schulz, G., Weitkamp, T., Zanette, I., Pfeiffer, F., Beckmann, F., David, C., Rutishauser, S., Reznikova, E., and Müller, B., "High-resolution tomographic imaging of a human cerebellum: comparison of absorption and grating-based phase contrast," *Journal of The Royal Society Interface* **7**(53), 1665–1676 (2010).

[13] Khimchenko, A., Deyhle, H., Schulz, G., Schweighauser, G., Hench, J., Chicherova, N., Bikis, C., Hieber, S. E., and Müller, B., "Extending two-dimensional histology into the third dimension through conventional micro computed tomography," *NeuroImage* **139**, 26–36 (2016).

[14] Thalmann, P., Bikis, C., Hipp, A., Müller, B., Hieber, S., and Schulz, G., "Single and double grating-based x-ray microtomography using synchrotron radiation," *Applied Physics Letters* **110**(6), 061103 (2017).

[15] Schulz, G., Götz, C., Müller-Gerbl, M., Zanette, I., Zdora, M.-C., Khimchenko, A., Deyhle, H., Thalmann, P., and Müller, B., "Multimodal imaging of the human knee down to the cellular level," *Journal of Physics: Conference Series* **849**(1), 012026 (2017).

[16] Buscema, M., Schulz, G., Deyhle, H., Khimchenko, A., Matviykiv, S., Holme, M. N., Hipp, A., Beckmann, F., Saxer, T., Michaud, K., and Müller, B., "Histology-validated x-ray tomography for imaging human coronary arteries," *Proceedings of SPIE* **9967**, 99670O (2016).

[17] Matviykiv, S., Buscema, M., Deyhle, H., Pfohl, T., Zumbuehl, A., Saxer, T., and Müller, B., "X-ray micro computed tomography for the visualization of an atherosclerotic human coronary artery," *Journal of Physics: Conference Series* **849**(1), 012002 (2017).

[18] Holme, M. N., Schulz, G., Deyhle, H., Weitkamp, T., Beckmann, F., Lobrinus, J. A., Rikhtegar, F., Kurtcuoglu, V., Zanette, I., Saxer, T., et al., "Complementary x-ray tomography techniques for histology-validated 3d imaging of soft and hard tissues using plaque-containing blood vessels as examples," *Nature protocols* **9**(6), 1401–1415 (2014).

[19] Bangham, A., Standish, M., and Watkins, J., "Diffusion of univalent ions across the lamellae of swollen phospholipids," *Journal of Molecular Biology* **13**(1), 238–252 (1965).

[20] Gregoriadis, G., "The carrier potential of liposomes in biology and medicine," *New England Journal of Medicine* **295**(13), 704–710 (1976).

[21] Fedotenko, I. A., Zaffalon, P.-L., Favarger, F., and Zumbuehl, A., "The synthesis of 1,3-diamidophospholipids," *Tetrahedron Letters* **51**(41), 5382–5384 (2010).

[22] Buscema, M., Matviykiv, S., Meszaros, T., Gerganova, G., Weinberger, A., Mettal, U., Mueller, D., Neuhaus, F., Stalder, E., Ishikawa, T., Urbanics, R., Saxer, T., Pfohl, T., Szebeni, J., Zumbuehl, A., and Müller, B., "Immunological response to nitroglycerin-loaded shear-responsive liposomes in vitro and in vivo," *Journal of Controlled Release* **264**, 14–23 (2017).

[23] Bugna, S., Buscema, M., Matviykiv, S., Urbanics, R., Weinberger, A., Meszaros, T., Szebeni, J., Zumbuehl, A., Saxer, T., and Müller, B., "Surprising lack of liposome-induced complement activation by artificial 1,3-diamidophospholipids in vitro," *Nanomedicine: Nanotechnology, Biology and Medicine* **12**(3), 845–849 (2016).

[24] Weinberger, A., Tanasescu, R., Stefaniu, C., Fedotenko, l. A., Favarger, F., Ishikawa, T., Brezesinski, G., Marques, C. M., and Zumbuehl, A., "Bilayer properties of 1,3-diamidophospholipids," *Langmuir* **31**(6), 1879–1884 (2015).

[25] Olson, F., Hunt, C., Szoka, F., Vail, W., and Papahadjopoulos, D., "Preparation of liposomes of defined size distribution by extrusion through polycarbonate membranes," *Biochimica et Biophysica Acta (BBA) - Biomembranes* **557**(1), 9–23 (1979).

[26] Noguchi, H., "Polyhedral vesicles: A brownian dynamics simulation," *Physical Review E* **67**(4), 041901 (2003).

[27] Kobayashi, T., Tsukagoshi, S., and Sakurai, Y., "Enhancement of the cancer chemotherapeutic effect of cytosine arabinoside entrapped in liposomes on mouse leukemia l-1210," *Gann Japanese Journal of Cancer Research* **66**(6), 719–720 (1975).

[28] Lopez-Berestein, G., Fainstein, V., Hopfer, R., Mehta, K., Sullivan, M. P., Keating, M., Rosenblum, M. G., Mehta, R., Luna, M., Hersh, E. M., Reuben, J., Juliano, R. L., and Bodey, G. P., "Liposomal amphotericin b for the treatment of systemic fungal infections in patients with cancer: A preliminary study," *The Journal of Infectious Diseases* **151**(4), 704–710 (1985).

[29] Colzi, I., Troyan, A. N., Perito, B., Casalone, E., Romoli, R., Pieraccini, G., Kalko-Basnet, N., Adessi, A., Rossi, F., Gonnelli, C., and Ristori, S., "Antibiotic delivery by liposomes from prokaryotic microorganisms: Similia cum similis works better," *European Journal of Pharmaceutics and Biopharmaceutics* **94**, 411–418 (2015).

[30] Szebeni, J., Muggia, F., Gabizon, A., and Barenholz, Y., "Activation of complement by therapeutic liposomes and other lipid excipient-based therapeutic products: Prediction and prevention," *Advanced Drug Delivery Reviews* **63**(12), 1020–1030 (2011).

[31] Nesargikar, P. N., Spiller, B., and Chavez, R., "The complement system: history, pathways, cascade and inhibitors," *European Journal of Microbiology & Immunology* **2**(2), 103–111 (2012).

[32] Szebeni, J., "Complement activation-related pseudoallergy: A stress reaction in blood triggered by nanomedicines and biologicals," *Molecular Immunology* **61**(2), 163–173 (2014).

[33] Chanan-Khan, A., Szebeni, J., Savay, S., Liebes, L., Rafique, N. M., Alving, C. R., and Muggia, F. M., "Complement activation following first exposure to pegylated liposomal doxorubicin (doxil): possible role in hypersensitivity reactions," *Annals of Oncology* **14**(9), 1430–1437 (2003).

[34] Szebeni, J., Bedócs, P., Csukás, D., Rosivall, L., Bünger, R., and Urbanics, R., "A porcine model of complement-mediated infusion reactions to drug carrier nanosystems and other medicines," *Advanced Drug Delivery Reviews* **64**(15), 1706–1716 (2012).

[35] Szebeni, J., Bedocs, P., Rozsnyay, Z., Weiszhar, Z., Urbanics, R., Rosivall, L., Cohen, R., Garbuzenko, O., Bathori, G., Toth, M., Bunger, R., and Barenholz, Y., "Liposome-induced complement activation and related cardiopulmonary distress in pigs: factors promoting reactogenicity of doxil and ambisome," *Nanomedicine: Nanotechnology, Biology and Medicine* **8**(2), 176–184 (2012).

Acknowledgments

First and foremost, I would like to thank my thesis advisor Prof. Dr. Bert Müller for giving me the opportunity to join the Biomaterials Science Center group and work in a multidisciplinary project. Prof. Dr. Bert Müller has guided me during these years providing always precious scientific input. I have learned a lot from his advice and for that, I am very grateful.

I wish to thank Prof. Dr. Alex Dommann for kindly being the co-referee of my thesis.

A special thank goes to Dr. Hans Deyhle, for numerous meaningful scientific discussions, for being always available to all my questions and for his great and unique support with the arduous SAXS data analysis. With some “magic” Matlab scripts, he gave me the hope to see my liposomes within the microfluidic device! Thanks Hans!!!

I am grateful to Dr. Georg Schulz for providing always valuable feedback and support on my work and assisting me during the beamtimes in Hamburg. I really enjoyed working and learning with him.

My thank goes to Dr. Simone E. Hieber for sharing her valuable knowledge as computational scientist and for guiding me through the hidden world of the iterative procedures. I really enjoyed the time with her, and I am really happy to have had the chance to work with her.

I wish to thank Dr. Thomas Pfohl for the fruitful scientific discussions. I enjoyed his perfect mood very much, even during the endless beamtime night shifts. I have really appreciate his support during these years.

I like to thank Dr. Andreas Zumbuehl for providing the precious "ingredient" which made my research possible.

I like to thank Dr. Till Saxer for his kind availability and support as medical doctor.

My thanks go to Dr. Felix Beckmann and to Alexander Hipp. Felix for the useful scientific discussions and support during the beamtime preparation and Alexander for his kind support day and night during the beamtime at DESY.

I am thankful to Prof. Jörg Huwyler, who allowed me using some instruments in his laboratories.

I like to thank Sofiya Matviykiv who shared with me the NO-Stress project. Actually, we have been often Stress(ed) but we also have had a lot of pleasant moments

together. I really enjoyed working with her around Europe, pushing together our challenging project towards the success.

My thanks go to Dr. Anna Khimchenko, for being always available for fruitful discussions. I really enjoyed the working hours including coffee breaks with her and the nice bbq together with her husband Sasha and the lovely Emiel Regis Rohellec Terzieff-Godefroy.

I like to thank Gabriela Gerganova for being part of the NanoStressGirls group together with Sofiya Matviykiv. I really enjoyed the time she was with us and the great assistance during the days in Budapest. I will always remember the nice moments shared eating Magnum ice cream at the end of the long working day.

I am thankful to thank Dr. Christos Bikis, for helping with the paraffin embedding of the specimen.

I would like to thank Dr. Viviane Lutz-Bueno for the useful discussions on microfluidcs.

My thanks go to Dr. Marco D. Dominietto for the interesting discussions about science, life, and italian politics.

I also like to thank all members of Biomaterials Science Center. With the hope to not forget anybody, I like to say thank to Verena Grötzinger, Griffin Rodgers, Willy Kuo, Dr. Simon Bugna, Dr. Florian Weiss, Dr. Tino Töpper, Dr. Bekim Osmani, Dr. Peter Thalmann, Matej Siketanc, Dr. Margaret N. Holme, and Dr. Natalia Chicherova. These years would not have been the same without their nice company!

Parts of this thesis have been proof-read by Griffin Rodgers, Sofiya Matviykiv, Anna Cavalieri, Bartolomeo Buscema, and Giuseppe Fisicaro. I like to thank them very much for the valuable advice.

I would like to thank my Family – Bartolomeo, Anna, Daria, Ettore – and my grand mothers Pina and Ada for giving me all their love and support during these years.
I wish to thank my 97-year old grandfather Tino, who supported me with his unique verve every Sunday afternoon during our usual phone call. Grazie Nonno!!!
I also like to remember and mention my grandfather Angelo, although I have never met him.

My thanks go to Principessa and Musetta, always present during the home-Skype calls with their sweet purr. The best cats one could ever desire!

And last but not least, I am thankful to my boyfriend Giuseppe Fisicaro, for taking care of me every day of the week. As scientist, he was always interested on discussing about my project allowing me to share my goals and failures. Thanks a lot!

Curriculum Vitae

Personal Information

Family Name: Buscema
First Name: Marzia Maria Gaia
Citizenship: Italian
Date of Birth: 10.12.1987
Place of Birth: Catania, Italy

Education

2013 - 2018	Ph.D. Researcher at the Biomaterials Science Center, Department of Biomedical Engineering, University of Basel Primary Advisor: Prof. Dr. Bert Müller Secondary Advisor: Prof. Dr. Alex Dommann
2010 - 2013	Master of Science in Condensed Matter Physics at University of Catania and CNR-IMM Catania Primary Advisor: Prof. Francesca Simone Secondary Advisor: Dr. Silvia Scalese
2005 - 2010	Bachelor Degree in Physics at University of Catania Advisor: Prof. Dr. Salvatore Lo Nigro